Characterization of the magma source and melt generation mechanisms of the Cenozoic intra-plate magmatism at the Harrat al-Shamah, Syria

Master Thesis

Sander Molendijk
Department of Earth Sciences, Utrecht University

July 8, 2018

Abstract

Extensive Cenozoic intra-plate volcanism in West-Arabia reflects a geodynamic setting relating convergent, transform, and plume related divergent plate boundaries. I present a detailed analysis of mineral- and recrystallized melt inclusions from an extensive set of >1000 early crystallized olivine hosts derived from alkali basalts of the Harrat al-Shamah in Syria. Major and trace element geochemistry of olivine crystals and inclusions was determined by SEM, EMPA, and LA-ICPMS. Volume corrections for recrystallized melt inclusions were used in order to determine bulk major element compositions without re-homogenization. On the basis of a compositionally variable dataset, I discerned three distinct melt groups documenting a compositional progression. Covariance of major and trace elements in these primary melts indicates compositional control by polybaric melting and binary mixing of spinel- and garnet peridotite derived end-member melts. High Dy/Yb, Zr/Y, and low Zr/Nb ratios in incompatible element enriched magmas indicate a magma source of Red-Sea MORB-type mantle which was locally re-fertilized by OIB-type material. Olivine-melt thermometry indicates the majority of melt-generation to be located at the lithosphere-asthenosphere boundary, consistent with thermal erosion by hot mantle. I argue for West-Arabian intra-plate volcanism to be driven by migrating plume material which locally exploited tectonically generated zones of lithospheric weakness. My data shows no evidence for melting of metasomatic veins and/or a separate mantle plume underneath West-Arabia.

Supervisors:

Prof. P.R.D. Mason

Dr. I.K. Nikogosian

Contents

1 Introduction

Determining mantle source compositions from volcanic rocks is an effective way of assessing the upper mantle structure and geodynamics at the root of any magmatically active environment. The various processes affecting magmas before eruption make this a difficult task on the basis of whole-rock data. This is especially true for regimes involving intra-continental volcanism, where both crustal and lithospheric involvement are common [*Fitton*, 1987; *Bergantz & Dawes*, 1994]. For these types of environments, melt inclusions have become increasingly relevant as containers of momentary magma compositions, allowing for retracing of the primary melt composition and its evolution though time [*Sobolev*, 1996]. The Arabian plate is an example of such a complex geodynamical setting accompanying extensive intra-plate volcanic activity, where plume activity and lithospheric extension appear to operate concurrently [*Schilling et al.*, 1992]. Plentiful geochemical and geodynamical studies have been carried out for this region based on whole-rock analysis and xenolith studies [e.g. *McGuire*, 1987; *Camp & Roobol*, 1989; *Camp & Roobol*, 1992; *Baker et al.*, 2000], but only limited attention has been given to northwestern lying volcanism trailing the Dead Sea Fault Zone (DSFZ). Despite this, the presence of the Harrat al-Shamah (HAS), the largest intra-plate volcanic field on the plate [*Shaw et al.*, 2003; *Krienitz et al.*, 2007], as well as multi-source indications of an anomalous mantle structure and composition [*Stein et al.*, 1993; *Krienitz et al.*, 2009; *Chang & Van Der Lee*, 2011; *Faccena et al.*, 2013], make this an area of increasing scientific interest [*Lustrino & Sharkov*, 2006]. Multiple geodynamic models have been proposed to account for the volcanic activity at the HAS, including (1) northward channelling of the Afar plume [*Sobolev et al.*, 2005; *Krienitz et al.*, 2007, 2009; *Chang & Van der Lee*, 2011; *Faccena et al.*, 2013], (2) the presence of an additional plume source [*Camp & Roobol*, 1992; *Chang & Van der Lee*, 2011], (3) Extension and lithospheric thinning related passive upwelling of (metasomatized) mantle [*Shaw et al.*, 2003; *Lustrino & Sharkov*, 2006; *Ismail et al.*, 2008], and (4) melting of fossilized plume material [*Stein & Hofmann*, 1992]. Explanations for the chemical signature of the volcanics in this area also include the preferential melting of amphibole-rich hornblendite from a heterogeneous mantle source [*Ma et al.*, 2011, 2013]. Study of this locality and specifically its potential relationship with the activity of the Afar plume may thus have far-reaching implications regarding plume dynamics and global intra-plate magma-genesis. This study aims to use melt inclusion data to document the compositions and formation conditions of the most primitive magmas underlying Harrat al-Shamah, in order to better understand the genetic link between magmatism and geodynamics in western Arabia.

2 Geological setting

The Arabian plate separated from the African-Arabian plate in the Late Oligocene. This separation was related to propagation of the Central Indian Ridge spreading system which started in the med- to late- Eocene [*Hempton*, 1987; *Daradich et al.*, 2003]. Collision between the Eurasian and Afro-Arabian plates at the northern lying Bitlis suture (Figure 1) started in the Medial to Late Eocene [*Hempton*, 1987]. Despite this collisional regime, extension in the south of the proto-Arabian plate caused block faulting in
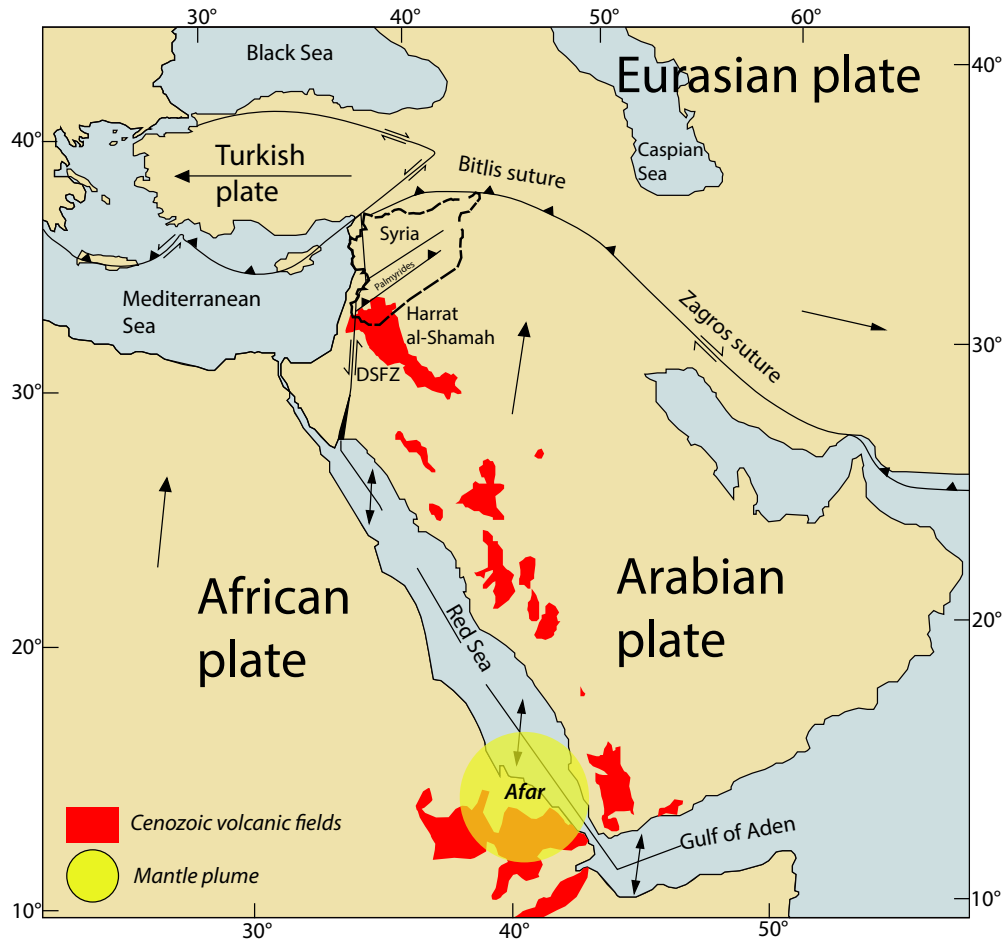
Figure 1: Geological map of the Arabian peninsula including present day geological features and volcanic fields, adapted from *Hemption* (1987). An approximate location of the Afar plume is noted, based on *Chang & Van der Lee* (2011). Locations of volcanic fields are adapted from *Al Kwatli et al* (2012) and *Chang & Van der Lee* (2011)

the current Gulf of Aden and Red Sea basins shortly afterwards [*Hempton*, 1987]. At approximately 30 Ma, continental rifting and associated magmatism were initiated in these areas, completely separating the Arabian plate from the African-Arabian plate [*Hempton*, 1987]. This is concurrent with the inferred moment of arrival of the Afar mantle plume, and the production of extensive magmatism in the Ethiopia- Yemen

continental flood basalt province (Figure 1) [*Furman et al.*, 2006 *and references therein*]. As an extension of the Red Sea Basin, the N-S oriented left lateral DSFZ developed at 18-22 Ma, in order to accommodate more rapid northward motion of Arabia compared to Africa (Figure 1) [*Hempton*, 1987; *Brew et al.*, 2001; *McClusky et al.*, 2003]. This sinistral strike slip fault of about 1000 km in length and 105 km in displacement

represents the most northerly boundary between the African and Arabian plates, crossing through the entire lithosphere [*Garfunkel*, 1981; *Sobolev et al.*, 2005]. Cross-cutting relationships have indicated this fault zone to have developed contemporaneously with the Red Sea, with the total displacement occurring over two periods [*Garfunkel*, 1981; *Brew et al.*, 2001]: an early phase of activity during Early- to Mid-Miocene, a break in activity between 14.5 and 4.5 Ma, and a secondary phase from the Early Pliocene onwards. Topographical asymmetry around the DSFZ is one of its most distinct features, assumed to result from variable degrees of Late Cenozoic uplift in the area [*Sobolev et al.*, 2005]. The eastern shoulder of the fault zone is up to 1500 m in altitude, whereas the western shoulder reaches a maximum elevation of 500 m [*Sobolev et al.*, 2005]. It has been proposed that thermal lithospheric erosion due to an elevated asthenospheric temperature is at the root of this uplift, while the division between oceanic and continent bound lithosphere created by the DSFZ generated the asymmetry [*Sobolev et al.*, 2005]. An additional form of Cenozoic uplift can be observed north of the Red Sea Basin, in the form of the West-Arabian swell [*Camp & Roobol*, 1992]. This zone has been related to the magmatism trailing the axis of uplift, which have both been active for the past 14 million years [*Camp & Roobol*, 1992]. Whereas magmatic activity in Arabia has been dated back to as early as the Jurassic [*Laws & Wilson*, 1997], the development of the various intra-plate volcanic fields known as Harrats (Figure 1) only started in the Early Oligocene with the opening of the Red Sea and separation of the plate from Africa [*Hempton*, 1987; *Camp & Roobol*, 1992; *Daradich et al.*, 2003; *Krienitz et al.*, 2007]. Slightly variable per locality, the volcanism is frequently divided into an older and younger phase of activity, dated at roughly 30-20 Ma, and <12 Ma [*Camp & Roobol*, 1992], whereas *Sharkov et al.* (1994) and *Lustrino & Sharkov* (2006) instead propose semi-continuous activity in some areas. The generated volcanic fields follow the Red Sea and DSFZ systems from Yemen in the South-East to Syria in the North-West, covering a total of approximately 200,000 km^2 (Figure 1) [*Camp & Roobol*, 1989; *Weinstein & Garfunkel*, 2014]. Erupted materials largely consist of transitional to strongly alkali basaltic suites, with the exception of some older, more tholeiitic rocks from Saudi Arabia [e.g. *Camp & Roobol*, 1992; *Krienitz et al.*, 2007]. The Harrat al-Shamah is the largest of the Harrats, covering 50.000 km^2, stretching from the south of Syria to the north of Saudi Arabia (Figure 1). Abundant geochronological data from this field indicates that its activity can roughly be divided into an initial phase between 26 and 16 Ma, and a second one starting at approximately 13 Ma [*Trifonov et al.*, 2011; *Al Kwatli et al.*, 2012]. The northernmost margin of the Harrat al-Shamah, the Djebel al-Arab, is found in southern Syria, near the Syrian rift (part of the DSFZ; Figure 1, 9). The magmatic rocks here are primarily Ti-rich alkali basalts and basanites, commonly forming massive lava flows erupted from fissures [*Sharkov et al.*, 1994; *Shaw et al.*, 2003; *Lustrino & Sharkov*, 2006; *Krienitz et al.*, 2007]. Volcanic cones on the top of the platform represent the youngest phase of activity, and frequently contain both mantle and crustal xenoliths which have been intensely studied [e.g. *Nasir & Safarjalani*, 2000; *Bilal & Touret*, 2001; *Ismail et al.*, 2008]. This study exclusively considers Quaternary age samples originating from the Djebel al-Arab volcanic field.

3 Geochemistry of Harrat al-Shamah volcanics

3.1 Major elements

Igneous rocks from the Harrat al-Shamah cover a range of compositions, with SiO_2 in the range of 41.0 to 60.2 wt%. The rock types are dominated by alkali basalts and basanites, but also include tephrites, hawaiites, mugearites, and rare trachytes and phonolites [*Krienitz et al.*, 2007]. In line with observations from the majority of western Arabian harrats, the magmatic suites are dominantly alkalic to transitional [*Camp & Roobol.*, 1992; *Shaw et al.*, 2003; *Krienitz et al.*, 2007]. Samples from the Jordanian parts of the HAS are generally less evolved than those from Syria, with the majority of samples containing between 7.8 and 10.5 wt% MgO [*Shaw et al.*, 2003], compared to 3.8 to 9.8 wt% MgO observed in their Syrian counterparts (Figure 2) [*Krienitz et al.*, 2007]. This primitive nature was also observed in comparison with Saudi Arabian volcanism, and has been attributed to a higher ascension rate in the Jordanian HAS region [*Shaw et al.*, 2003]. The Syrian specific magmatism has previously been divided into three series: 1 (<1 Ma), 2 (1-3.5 Ma), and 3 (>3.5-7 Ma) [*Krienitz et al.*, 2007]. Major element variations between series one and three are minor, while series two is frequently observed to diverge, including primarily basanites and tephrites rather than the alkali basalts common to the other series (Figure 2) [*Krienitz et al.,* 2007]. This difference is most pronounced for samples with MgO>6 wt%, and is best observed in comparatively elevated concentrations of TiO_2, Na_2O, K_2O, and P_2O_5, as well as lower concentrations of SiO_2 for any given MgO value [*Krienitz et al.*, 2007]. Positive correlations can be observed in both Jordanian and Syrian samples between MgO and FeO, while MgO is negatively correlated with SiO_2, Al_2O_3, Na_2O, and K_2O. However, due to a relatively constant MgO content, trends are less pronounced in Jordanian rocks [*Shaw et al.*, 2003].

3.2 Trace elements

Primitive mantle relative trace element compositions of HAS-derived rocks include only few pattern variations on incompatible trace element diagrams, primarily controlled by rock type (Figure 3) [*Krienitz et al.*, 2007]. An overall enrichment in incompatible elements is present in all rocks from this area, with similar patterns, distinctly peaking at Ta, observable in all but the most evolved lavas (Trachytes). Alkali basalts in particular present a consistent enrichment pattern similar to Afar plume derived Ethiopian flood basalts, but contain lower absolute concentrations (Figure 3). This relative depletion was not observed in basanites from the same locality, which are most similar in elemental abundances to Afar [*Pik et al.*, 1999]. Jordanian lavas include a wide range of compositions in terms of overall enrichment, and include some of the most depleted samples. Nevertheless, these rocks also lack indication of time-dependent variation in trace element abundances (Figure 3). Roughly all HAS rocks are enriched in Ba and Sr, and are commonly slightly enriched in Ti, the former of which is typical for rocks from Syria and the Mashrek area [*Lustrino & Sharkov*, 2006]. The Sr enrichment of these rocks is their most distinct difference with Afar plume derived rocks. Negative anomalies are common in Th, U, Y, and K, the latter of which is only present in the more primitive Jordanian samples, often accompanied by a negative Pb anomaly [*Shaw et al.*, 2003]. Compatible trace elements Cr and
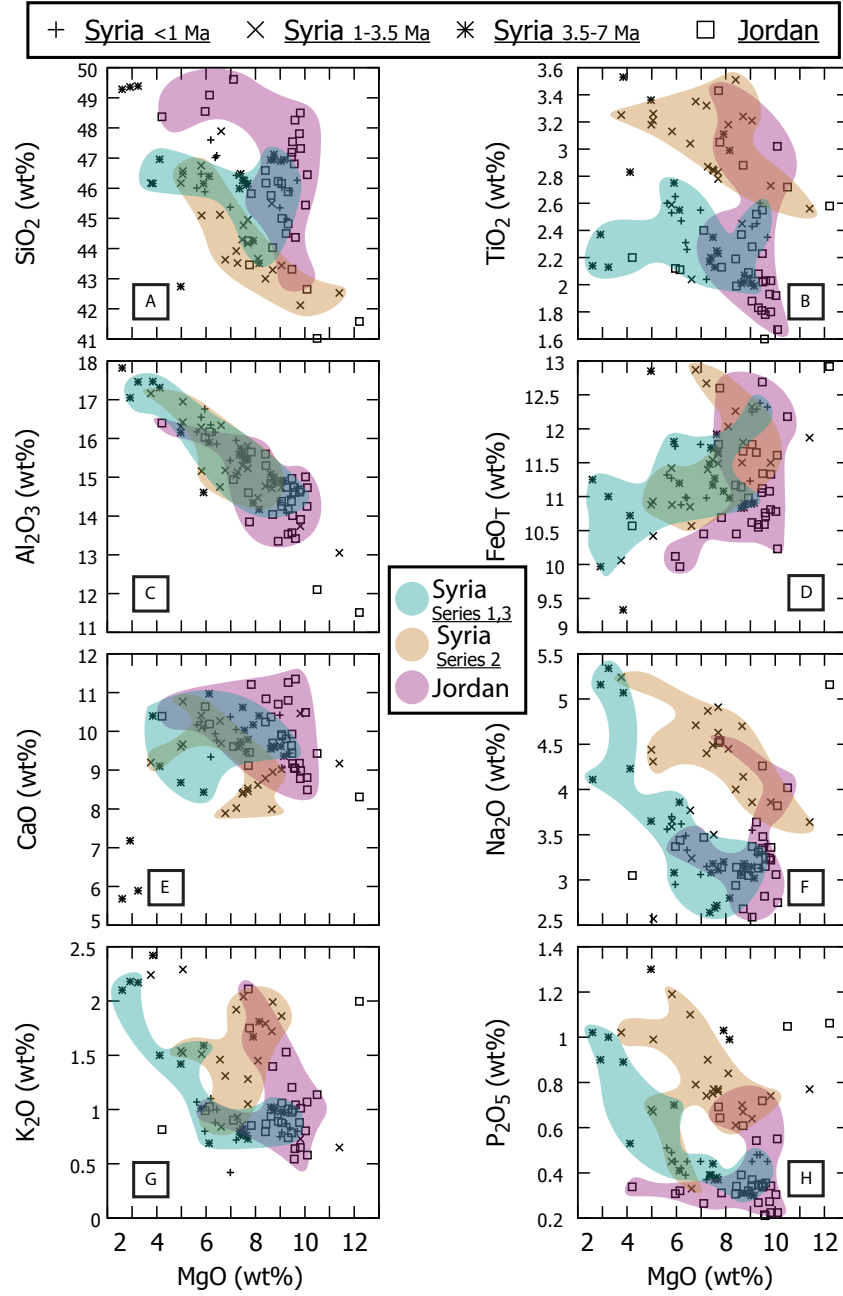
Figure 2: Representative major element data for HAS volcanics from Syria and Jordan, data from *Krienitz et al.* (2007) and *Shaw et al.* (2003), respectively. Colours are indicative of chemically similar groups.
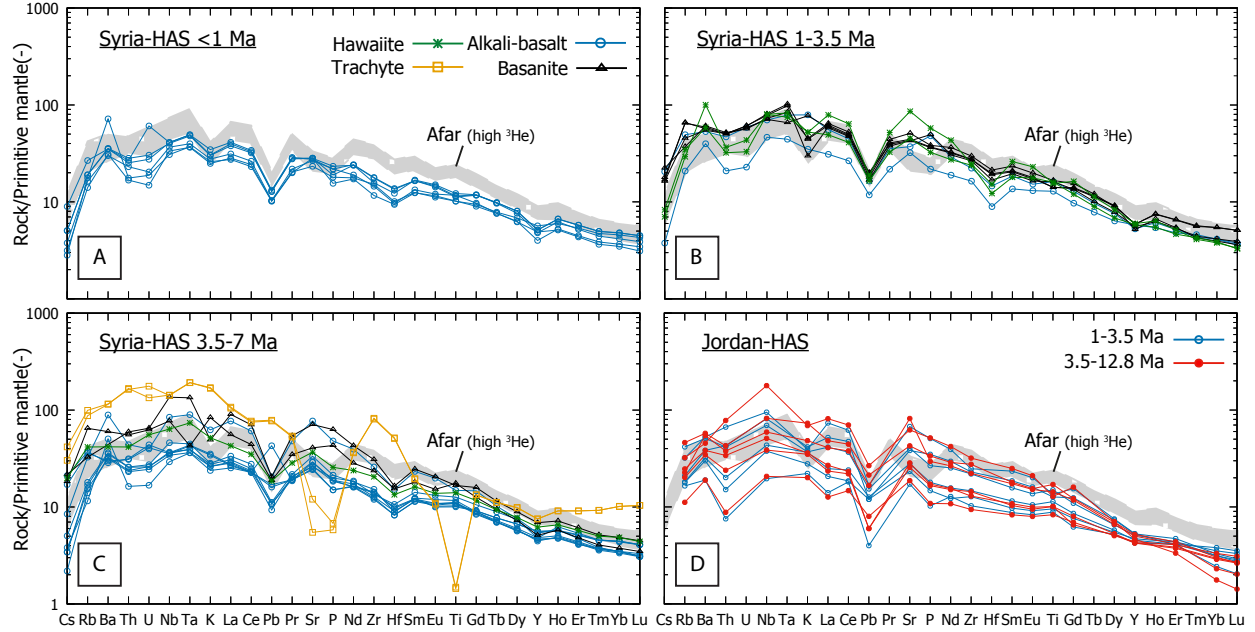
Figure 3: Representative trace element diagrams for HAS volcanics from Syria series 1 (A), 2 (B), and 3 (C), as well as Jordan, data from *Krienitz et al.* (2007) and *Shaw et al.* (2003), respectively. Primitive mantle composition used for normalization as in *Mcdonough & Sun* (1995). Afar plume representative high ^3He data from *Pik et al.* (1999).

Ni increase with MgO in samples from all localities [*Lustrino & Sharkov*, 2006; *Shaw et al.*, 2003; *Krienitz et al.*, 2007]. Based on ratios of incompatible elements K/Nb, La/Nb, Th/La, and Ba/Nb, *Shaw et al.* (2003) argued for a similarity in composition between the Jordanian HAS rocks and HIMU-type OIB. These ratios were measured to be 122, 91.7, 122, and 103.6% of HIMU values. Ce/Pb ratios have been shown to positively correlate with Nb/U in all wholerocks from the HAS (Figure 4) [*Krienitz et al.*, 2007], indicative of contamination by High Pb, U crustal material. Nevertheless, only some of the Syrian basalts older than 3.5 Ma have Ce/Pb ratios that are offset strongly enough to indicate significant contamination [*Krienitz et al.*, 2007]. For these rocks, Ce/Pb correlation with K/La

(Figure 4) has been used to argue for contamination by the Precambrian basement in some areas of the Syrian Harrat al-Shamah [*Krienitz et al.*, 2007]. The low K/La ratio, as well as a frequently observed low Ba/Nb ratio in rocks from this region has been a point of discussion in previous studies [*Weinstein et al.*, 2006; *Krienitz et al.*, 2007, 2009; *Ma et al.*, 2011]. Some authors attribute this to the mantle source composition, arguing for a similar reservoir extending northwards from the Red Sea [*Krienitz et al.*, 2007]. Alternatively, preferential melting of metasomatic lithologies such as amphibole peridotite and/or pyroxenite veins has been suggested to result in similarly depleted ratios [*Weinstein et al.*, 2006; *Ma et al.*, 2011, 2013]. Melting of a hydrous mantle as opposed to anhydrous
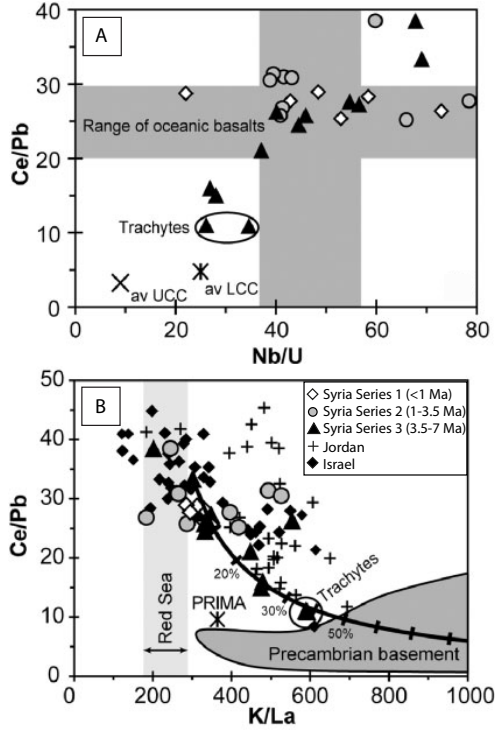
Figure 4: Trace element ratio diagrams by *Krienitz et al.* (2007). Jordan and Israel data from *Shaw et al.* (2003) and *Weinstein et al.* (2006), respectively. (a) Ocean island array based on *Hofmann et al.* (1986). Average compositions of upper (UCC) and lower (LCC) continental crust are based on *Rudnick & Fountain* (1995).(b) Precambrian basement, Red Sea, and PRIMA data from *Jarrar et al.* (2003), *Rogers* (1993), and *Sun & Mcdonough* (1989), respectively.

peridotite also helps explain the extensive volcanism in this region without the influence of an active mantle plume. Various authors, e.g. *Lustrino & Sharkov* (2006), *Weinstein et al.* (2006), and *Ma et al.* (2011), argued that the highly elevated and diverse set of MREE/HREE and LREE/HREE ratios in combination with approximately constant Yb concentrations found in rocks from this area cannot be explained by simple melting of spinel peridotite (Figure 5). However, whereas *Shaw et al.* (2003) argue for polybaric melting between spinel and garnet peri-

dotite, *Krienitz et al.* (2007) instead argued for complete melting in the garnet peridotite field. The former hypothesis argues for binary mixing on the basis of straight mixing lines observed in normalised Dy/Yb-La/Yb diagrams [*Shaw et al.*, 2003]. *Shaw et al.* (2003) observe a progressive migration of melting towards deeper levels, contrary to the consistent shallow melting signature from Yemen, and therefore argue for extension driven melt generation. Conversely, *Krienitz et al.* (2007) require no influence of spinel peridotite to explain their dataset (Figure 5), and additionally argue for the requirement of an elevated mantle temperature based on whole-rock thermometry. Their genetic model requires variable degrees of melting, hypothesised to result from a pulsing influx of hot mantle plume material from the Afar plume region. However, despite the large variation in models, there is an agreement amongst the literature that the geochemical signature of the Harrat al-Shamah, and indeed, that of most of West-Arabian magmatism, requires either an enriched mantle composition or metasomatic influences [e.g. *Shaw et al.*, 2003; *Weinstein et al.*, 2006; *Krienitz et al.*, 2007, 2009; *Ismail et al.*, 2009; *Ma et al.*, 2011, 2013].

3.3 Isotopic composition

The $^{87}Sr/^{86}Sr$ isotope ratios of HAS rocks from Jordan, Syria, and Israel are observed to stretch roughly between 0.70305 and 0.70415, while $^{143}Nd/^{144}Nd$ varies between 0.512804 and 0.512989 [*Bertrand et al.*, 2003; *Shaw et al.*, 2003; *Weinstein et al.*, 2006; *Krienitz et al.*, 2007]. Independent of age, the two ratios show negative correlations in the Jordanian rocks, with only few exceptions to the main array [*Shaw et al.*, 2003]. This negative trend is also ob-
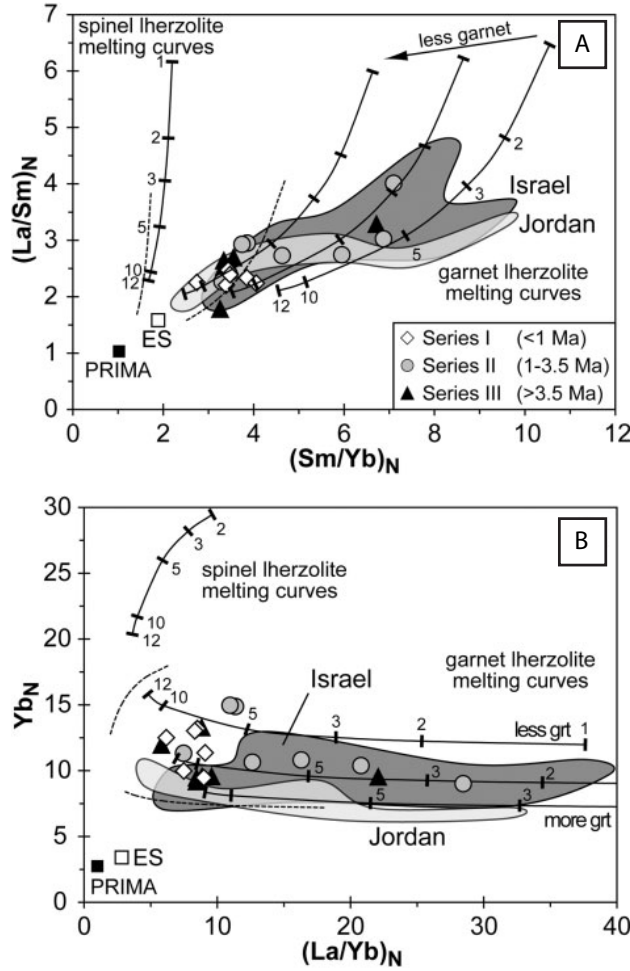
Figure 5: Chondrite normalised (a) Sm/Yb vs La/Sm and (b) La/Yb vs Yb diagrams for uncontaminated Syrian HAS lavas by *Krienitz et al.* (2007). Jordan and Israel fields from *Shaw et al.* (2003) and *Weinstein et al.* (2006), respectively. Melting curves for non-modal batch melting are shown for garnet and spinel lherzolites of PRIMA compositions (dashed lines), as well as enriched source compositions (continuous lines). PRIMA and chondrite compositions are from *McDonough & Sun* (1995). Key as in Figure 6. For additional information, see *Krienitz et al.* (2007).

served in series 2 and 3 of the Syrian rocks, but fails to account for the youngest series, which contains samples more closely resembling those from the western Israeli parts of the volcanic

field [*Krienitz et al.*, 2007]. These rocks generally posses significantly lower $^{143}Nd/^{144}Nd$ ratios for a given $^{87}Sr/^{86}Sr$ ratio, and show a weaker correlation between the two. The relationship between these two ratios plots the Israeli and young Syrian parts of the HAS within the field of Saudi Arabian magmatism, but outside of any other distinct volcanic fields (Figure 7) [*Weinstein et al.*, 2006; *Krienitz et al.*, 2007]. Jordanian rocks, and by extension those of the older Syrian series, instead plot overlapping multiple arrays: Samples with lower $^{87}Sr/^{86}Sr$ ratios plot within the compositional range of Saudi Arabian rocks (Figure 7), while rocks with higher $^{87}Sr/^{86}Sr$ ratios are compositionally similar to those from Yemeni intra-plate volcanism [*Shaw et al.*, 2003]. Compared to high ^3He Afar plume basalts, all HAS data presents lower ratios of both elements, but the largest offset is observed
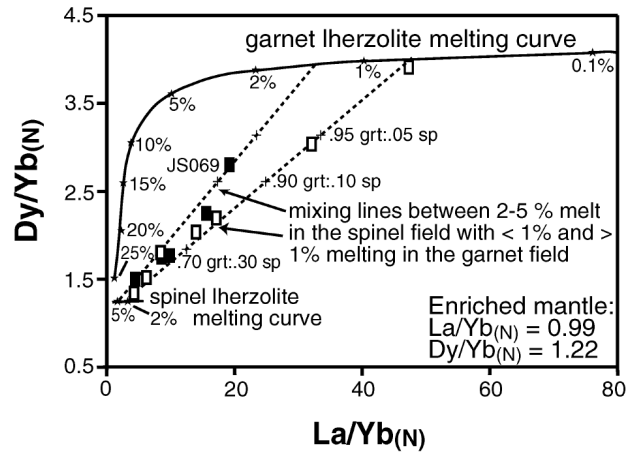
Figure 6: Primitive mantle normalised Dy/Yb vs La/Yb diagram for Jordanian HAS lavas by *Shaw et al.* (2003). Primitive mantle composition is from *Taylor & Mclennan* (1985). Melting curves for non-modal fractional melting are shown for garnet and spinel lherzolites sources. Stars on melting curves indicate degrees of melting. Dashed lines represent mixing lines between melts from spinel- and garnet-facies mantle. For additional information, see *Shaw et al.* (2003).

10
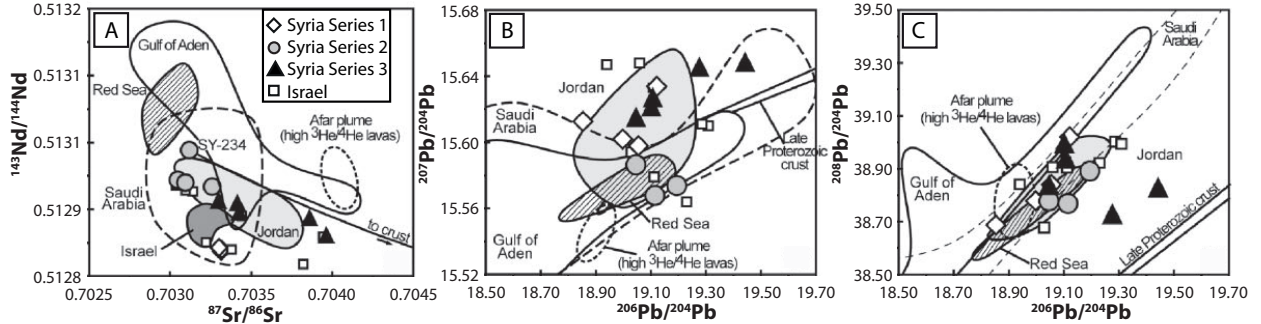
Figure 7: (a) Sr vs Nd, (b) ^{207}Pb/^{206}Pb, and (c) ^{208}Pb/^{206}Pb ratio diagrams by Krienitz et al. (2007). Fields and data are representative for intra-plate volcanism from Jordan [*Bertrand et al.*, 2003; *Shaw et al.*, 2003], Israel [*Weinstein et al.*, 2006], the Red Sea [*Eissen et al.*, 1989; *Haase et al.*, 2000], high ^{3}He/^{4}He lavas from the Afar plume [*Pik et al.*, 1999], Gulf of Aden [*Schilling et al.*, 1992], and Saudi Arabia [*Hegner & Pallister*, 1989; *Altherr et al.*, 1990; *Bertrand et al.*, 2003], and the Late Proterozoic crust [*Baker et al.*, 2000]. For additional background, see *Krienitz et al.* (2007).

in Sr isotopes [*Krienitz et al.*, 2007]. Lead isotopes are in better agreement between the Jordanian and young Syrian parts of the HAS, indicating the largest distinction between the two suites to be that of their ^{143}Nd/^{144}Nd ratios [*Krienitz et al.*, 2007]. *Shaw et al.* (2003) observed significant co-variance between major elements, trace elements, and isotopes, which could not be explained through simple AFC processes. In particular, negative correlations between ^{143}Nd/^{144}Nd and Sm/Nd ratios (Figure 8) formed additional evidence for polybaric melting of heterogeneous mantle, as this is inconsistent with progressive depletion of a single chemically homogeneous source [*Shaw et al.*, 2003]. Published ratios of ^{208}Pb,^{207}Pb, and ^{206}Pb over ^{204}Pb from the Israeli, Jordanian, and Syrian parts of the HAS cover ranges of 38.652-39.020 [*Bertrand et al.*, 2003], 15.563-15.654 [*Shaw et al.*, 2003], and 18.833-19.443 [*Krienitz et al.*, 2007], respectively. A clear positive correlation can be observed between the former and latter ratios, whereas ^{207}Pb/^{206}Pb ratios appear largely uncorrelated. All Pb ratios other than ^{208}Pb/^{204}Pb present higher values than those from the high ^{3}He Afar derived basalts [*Pik et al.*, 1999; *Krienitz et al.*, 2007]. Instead, basalt samples from Syria with ages between 1 and 3.5 Ma show an overlap in lead isotopes with Red Sea MORB (Figure 7) [*Krienitz et al.*, 2007], reaffirming the presence of a chemically distinct ambient mantle underneath Arabia. Overlap with the large range of Saudi Arabian data is also observed in Pb isotope data for most of this volcanic field (Fig-

Figure 8: ^{143}Nd/^{144}Nd vs Sm/Nd diagram for Jordanian rocks by *Shaw et al.* (2003), suggesting mixing of isotopically distinct sources.

ure 7) [*Bertrand et al.*, 2003; *Shaw et al.*, 2003; *Krienitz et al.*, 2007]. It has been argued that the isotopic similarities between the Red Sea and noticeably enriched zones of melt generation indicate relatively recent enrichment events affecting the mantle under Syria [*Krien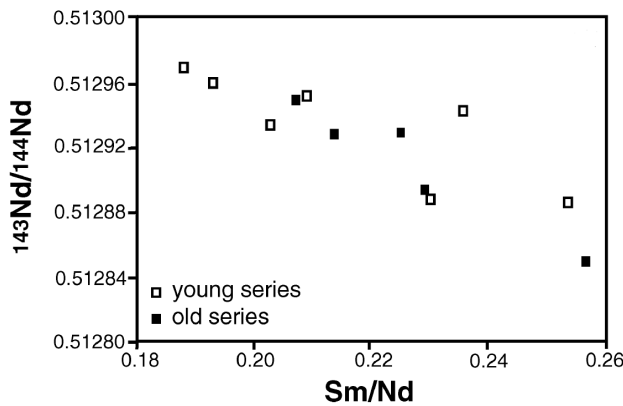itz et al.*, 2007]. Additionally, samples with especially high lead and strontium isotope ratios, though scarce, are thought to potentially result from contamination by Proterozoic continental crust [*Krienitz et al.*, 2007; *Shaw et al.*, 2003].

of 1.5 mm, while the smallest crystals in all samples are approximately 50 μm across. Feldspar phenocrysts are subhedral to euhedral in sample 97Syr1, while samples 00Syr1 and 00Syr2 also contain large anhedral feldspar masses. Olivine can frequently be found within these masses. This occurrence type of the mineral is not considered for the study, as a a non-magmatic nature is assumed. Samples 00Syr1 and 00Syr2 additionally include secondary calcite, although very localised.

4   Studied samples

This study considers a total of four Quarternary age basalt samples collected from the Djebel al-Arab volcanic field (Figure 9), namely samples 97Syr1, 00Syr1, 00Syr2, and 00Syr4. Sample names preceded with '00' were retrieved in 2000, for the study of *Ismail et al.* (2008). Sample 00Syr4 concerns a xenolith encased in basalt, for which only the surrounding rock was used in this study. Samples 97Syr1, 00Syr1, and 00Syr2 instead concern alkali basalts. Double polished thin sections were already available for these three samples samples. The thin sections of all samples show porphyritic textures in all samples (Figure 10). The groundmass is cryptocrystalline, composed primarily of pyroxene and feldspar. Phenocrysts of olivine and plagioclase compose approximately 10-15% of the total volume. Tabular feldspar crystals range up to 5 mm in length, and equant olivine phenocrysts have a maximum diameter of approximately 2 mm. Both mineral types are larger in samples 00Syr1 and 00Syr2, but the size disparity is most pronounced for feldspar, of which the maximum length is 1 mm in sample 97Syr1. Olivine in this sample has a maximum diameter

Figure 9: Geological map of Western Syria including volcanic fields, showing the sample locality for the 00- collection. Adapted from *Ismail et al.* (2009).
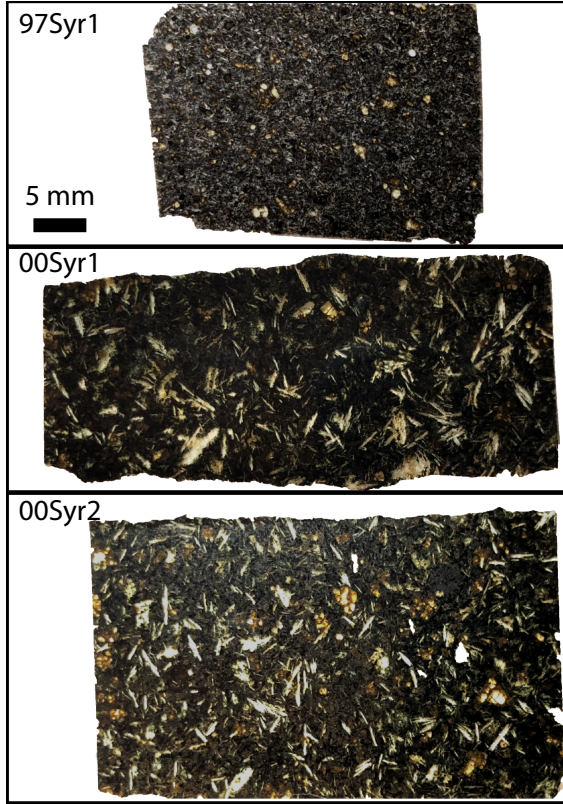
Figure 10: Images of thin section slides used in the study. Yellow colours are olivine phenocrysts, white colours are feldspar.

5 Methods and analytics

5.1 Sample preparation

For melt inclusion analysis, olivine phenocrysts had to be separated from whole-rock samples. To accomplish this, the samples were crushed and sieved to <0.2, 0.2-0.5, and >0.5 mm fractions, after which olivine suitable for analysis was selected by hand from the latter two fractions. Olivine was selected based on size and colour, with a preference for large, brightly green grains, as this colour is assumed to be representative of Fo content. A total of 1096 olivine grains were

mounted into 1 inch thick epoxy holders and polished on one side for following analytical methods. This work was done at the Vrije Universiteit, Amsterdam. Fusion beads were produced from all whole-rock samples at Utrecht University using *ICPH Fluomix 6515 Lil* at a sample:FLUX ratio of 1:10, to be used in later analytical work as representative whole-rock compositions. Additionally, a fusion bead was made from reference material JJR-2022, to be used in assessment of measurement accuracy. An additional epoxy holder was then constructed to include two fragments of the reference material glass, as well as single fragments from each whole-rock fusion bead.

5.2 Scanning electron microscope analysis

Scanning Electron Microscope (SEM) analysis was performed on all five 1 inch epoxy holders at the Vrije Universiteit, Amsterdam using a JEOL JCM 6000 Benchtop SEM. Operating conditions during EDx analysis were 15 kV accelerating voltage, and a probe current of $\sim$ 1nA. Pulse Height Analyser (PHA) mode T3 was used, with a live time for analysis of 30 seconds for all measurements. All SEM EDx analyses consider rectangular areas rather than singular points. Respective area boundary dimensions vary between 1 and 10 μm depending on mineral size based on BSE imagery, details of which are listed in Electronic Appendix per analysis. In order to assess the measurement accuracy, the two reference material fusion bead fragments were analysed a total of 9 times under identical conditions and area dimensions of approximately 20-30 μm in both length and width, the results of which are listed in Table 2. A comparison to known concentrations indicates a significant (1.92-3.38

13

wt%) underestimation of FeO concentrations, as well as minor ones for Al_2O_3 (0.53 wt%), MgO (0.31 wt%), CaO (1.01 wt%), and Na_2O (1.27 wt%). Compensating for accurate totals, overestimations are commonly observed for SiO_2 (2.91 wt%), TiO_2 (0.1 wt%), MnO (0.3 wt%), K_2O (2.91 wt%), and P_2O_5 (0.64 wt%).

5.3 Microprobe analysis

Microprobe analysis was performed at Utrecht University using a JEOL JXA-8530F Hyperprobe Field Emission Electron probe microanalyser. Operating conditions for all WDS analyses were an accelerating voltage of 15 kV, and a nominal beam current of $\sim$ 10 nA. Counting times for all elements were 20 seconds on peak, and 10 seconds on background. I used a beam size of 1 μm for spinel, 3 μm for olivine, and 15 μm for whole-rock and reference glasses. All glasses were measured 5 times at different parts of the fragments. Internal data processing of raw data was done using Probe for EMPA software [probesoftware.com]. Due to the large amount of FLUX in the glasses, WDS analysis was destructive for these samples. The WR data was therefore adjusted per element on the basis of the deviations from known values of the 10 reference material measurements, listed in Table 2. Comparison with known concentrations indicates a general overestimation of SiO_2 of 2-2.5 wt%, and underestimation of Al_2O_3 and FeO in the order of 1 wt%. Additional deviations are sub-wt%, which can partially be attributed to low concentrations. Data from olivine and spinel grains analysed exclusively by SEM was adjusted on the basis of median EMPA/SEM measurement ratios per element acquired from grains analysed by both techniques. These adjustment factors are listed in Table 1 and visualised in Fig-

Table 1: Median ratios of EMPA/SEM measurements for single grains per oxide used as adjustment factors for SEM data. Number of analyses used for median listed after 'N', standard deviation in dataset listed under '1σ'. *For Cr_2O_3 & NiO holds N=101 & N=162,respectively. **For SiO_2 & MnO holds N=69 & N=4, respectively.

N	Olivine 188*		Spinel 71**	
	Factor	1σ	Factor	1σ
SiO_2	1.028	0.01	-	-
TiO_2	-	-	0.953	0.27
Al_2O_3	-	-	0.961	0.18
V_2O_3	-	-	-	-
Cr_2O_3	0.380	0.93	0.964	0.21
FeO	1.122	0.08	1.071	0.19
MnO	0.807	0.54	-	-
MgO	0.925	0.03	0.872	0.17
CaO	1.014	0.23	-	-
NiO	1.065	2.87	-	-

ures 11 & 12. Major elements show acceptable agreement with the adjustment factor (R^2=0.38-0.80 for olivine, R^2=0.37-0.97 for spinel), especially FeO & MgO required for determining forsterite content in olivine (R^2=0.80). However, trace oxides such as NiO in olivine and SiO_2 in spinel show bad correlation between the estimated corrected line and measured values due to a large amount of scatter or far outlying values (R^2=0.05 & R^2=0.09). Insufficient measurement of MnO in spinel (N=4) means adjustment of this oxide is either not possible or highly speculative and is thus not taken into account for samples not measured by WDS. Spot EDx analyses performed on surface features on the microprobe were performed at 15 kV and 10.00 seconds live time. Due to the small area of analysis and lower total counts due to measurement time, microprobe EDx data was only used for phases not previously analysed by SEM.
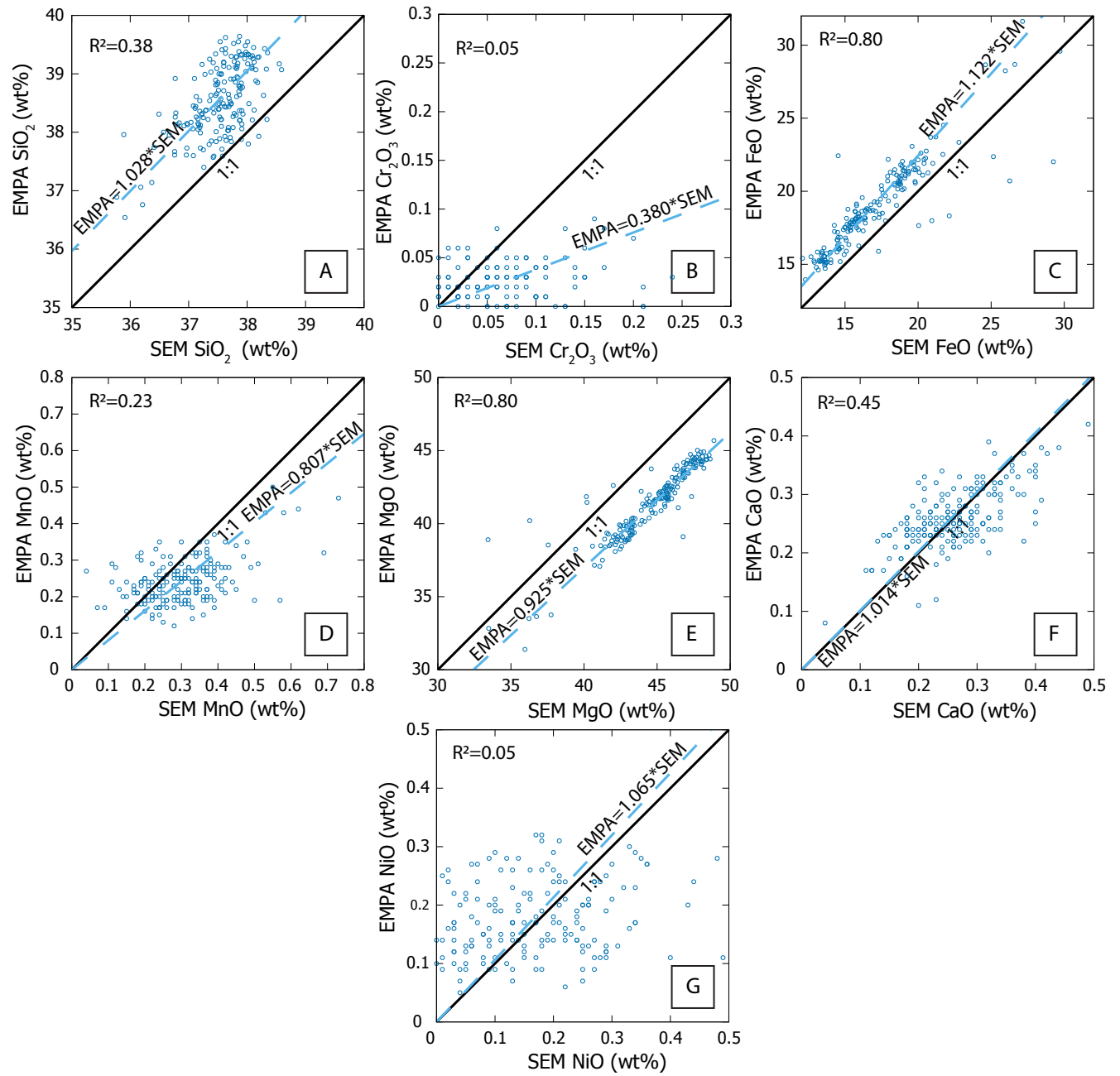
Figure 11: EMPA vs SEM data for all measured elements for single olivine grain measurements. The correction trend-line based on Table 1 and fitting R^2 is given (dashed line), as well as a 1:1 line for reference (continuous line).
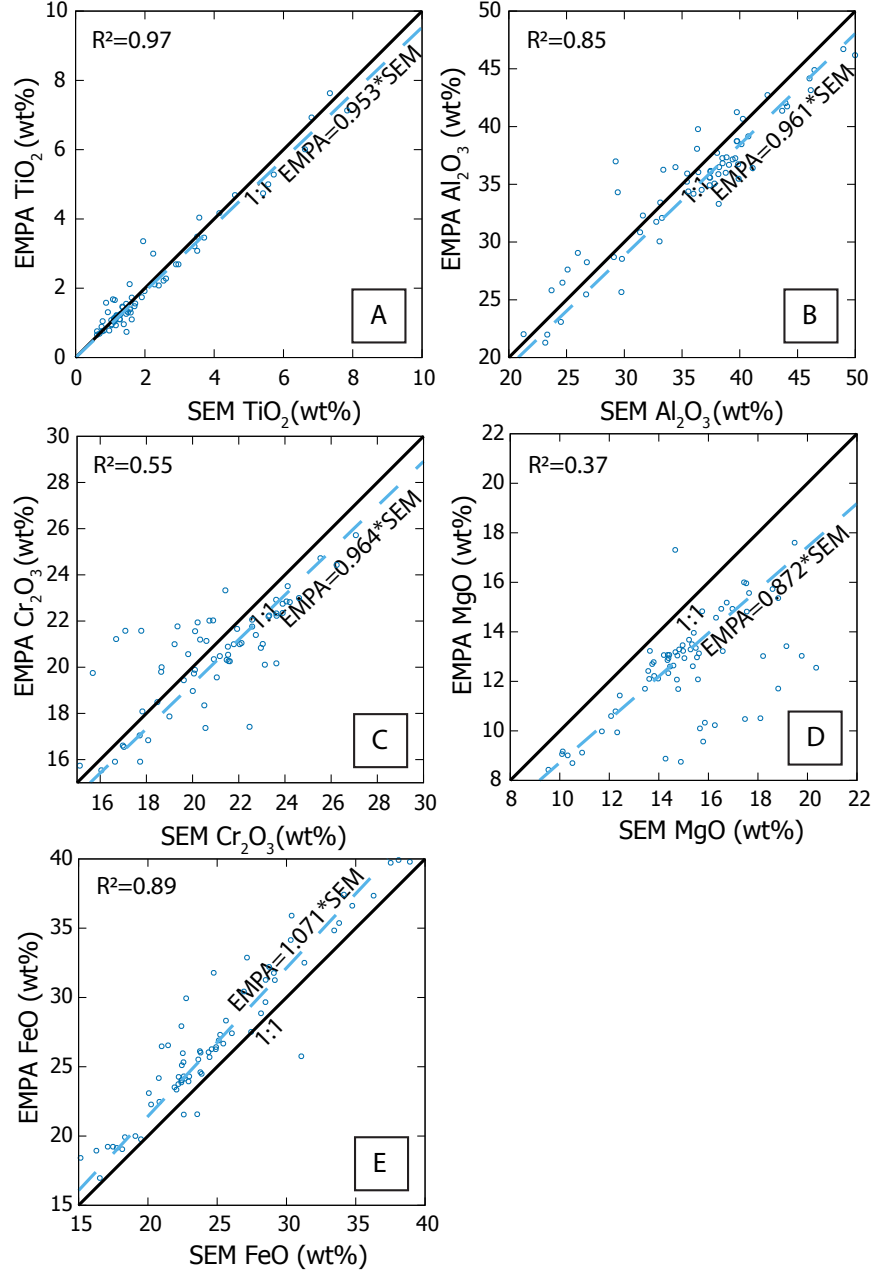
Figure 12: EMPA vs SEM data for all measured elements for single spinel inclusion measurements. The correction trend-line based on Table 1 and fitting R^2 is given (dashed line), as well as a 1:1 line for reference (continuous line).

Table 2: SEM EDx and EMPA WDS analysis results for reference material JJR-2022 normalised to 100% totals compared to known concentrations. A multiplication coefficient based on the real/average ratio of WDS analyses is listed. This is used for adjustment of WR data in Table 4. N.d. = not detected.

	SiO_2	TiO_2	Al_2O_3	FeO_T	MnO	MgO	CaO	Na_2O	K_2O	P_2O_5
					SEM (EDx)					
JJR-2022	51.09	1.58	14.55	6.43	0.48	7.36	10.90	2.12	3.38	2.11
	51.18	0.70	15.02	6.47	0.70	8.06	10.34	2.21	4.12	1.20
	52.16	2.01	15.28	6.74	0.26	8.07	10.56	2.09	2.81	n.d.
	50.75	2.10	15.17	7.54	0.66	7.35	10.45	2.01	3.76	0.20
	52.51	2.50	14.88	6.08	0.28	8.23	9.80	2.00	3.21	0.50
	51.79	1.94	15.64	7.13	n.d.	7.51	9.75	1.93	2.78	1.54
	50.49	2.38	14.74	7.49	0.37	7.58	9.76	2.20	3.18	1.82
	52.33	1.08	15.28	6.37	0.46	8.54	10.12	2.18	3.64	n.d.
	50.58	1.12	15.76	7.30	0.58	8.57	10.12	1.72	2.63	1.61
Average	**51.07**	**1.70**	**15.04**	**6.79**	**0.47**	**7.86**	**10.13**	**2.04**	**3.26**	**1.28**
Real	*48.16*	*1.6*	*15.57*	*9.46*	*0.17*	*8.17*	*11.14*	*3.31*	*1.78*	*0.64*
					Microprobe (WDS)					
JJR-2022	50.23	1.27	14.70	8.41	0.31	7.71	11.24	3.50	1.78	0.78
	50.97	1.32	14.45	8.41	0.11	7.62	11.33	3.19	1.85	0.75
	50.78	1.55	14.67	8.30	0.29	7.53	11.10	3.09	1.95	0.83
	50.23	1.45	14.77	8.33	0.36	7.40	11.00	3.14	1.90	1.12
	50.71	1.76	15.07	8.38	0.00	7.48	11.48	3.07	1.93	0.56
	50.33	1.53	14.31	8.32	n.d.	7.86	11.51	3.09	1.88	1.06
	49.31	1.39	15.25	8.45	0.37	7.82	11.37	3.22	1.90	0.77
	50.06	1.46	14.71	8.32	0.22	7.70	11.33	3.34	1.97	0.90
	50.30	1.65	14.63	8.63	0.09	7.77	10.96	3.25	1.80	0.99
	50.87	1.56	14.31	8.45	0.01	7.83	11.32	2.98	1.89	0.87
Average	**50.38**	**1.49**	**14.69**	**8.40**	**0.15**	**7.67**	**11.26**	**3.19**	**1.88**	**0.86**
Real	*48.16*	*1.6*	*15.57*	*9.46*	*0.17*	*8.17*	*11.14*	*3.31*	*1.78*	*0.64*
Coefficient	**0.96**	**1.07**	**1.06**	**1.13**	**1.14**	**1.07**	**0.99**	**1.04**	**0.94**	**0.74**

5.4 Laser ablation ICP-MS

Laser Ablation Inductively Coupled Plasma Mass Spectrometry (LA-ICPMS) was performed at Utrecht University using a ThermoFischer Scientific Element 2 magnetic sector ICP-MS and a Geolas [Microlas, Goettingen, Germany] 193 nm excimer laser ablation system. Analyses used a beam diameter of 40- to 80 μm, depending on the melt inclusion size. Surface melt inclusion measurements were preceded by 60 seconds of background, followed by 60 seconds of ablation (stopped prematurely in the case that the inclusion was fully ablated). The procedure was finished by 15 additional seconds of background. Melt inclusions located at depth were instead given 40 to 50 seconds of initial background, in order to make sure the entire inclusion could be ablated. A representative deep melt inclusion signal is presented in Figure 13, showing selected element signals over time. One USGS reference material BCR-2G measurement and two glass material NIST SRM 610 measurements were taken after every 10 analyses to serve as external standard, and in order to assess equipment stability and accuracy, respectively (Table 3). Element concentrations of these reference materials were taken from the GeoReM database [http://georem.mpch-mainz.gwdg.de]. For elements Mg, Ca, Ti, Sm, and Eu we report isotopes with the weights of 24, 43, 47, 149, and 153 u. On the basis of strong deviations from mean and reference values, elements Ta and Lu were excluded from interpretation for all samples. Data was processed using GLITTER data reduction software. Detection limits are reported at the level of 10σ as calculated from the gas blank, following the procedure from *Mason et al.* (2008). For whole-rock samples, calcium concentrations as in Table 4 were used as internal stan-

Table 3: LA-ICPMS results for USGS reference glass BCR-2G given for relevant measured elemental concentrations. Mean values were derived from a total of 5 BCR measurements. Standard deviations (SD) are included for reference values.

Element	Mean±1σ (ppm)	GeoReM±SD (ppm)
BCR-2G		
Na	29694±4457	28131±609
Mg	22390±2934	21466±542
Al	75523±6501	70920±2117
Si	290225±17837	254271±1869
Ca	50457±-	50458±786
Ti	12139±552	14100±1000
V	474.57±13.19	425±18
Cr	18.37±1.49	17±2
Ni	8.62±4.34	13±2
Rb	53.58±2.45	47±0.5
Sr	349.68±14.64	342± 4
Y	31.61±2.37	35±3
Zr	171.74±11.55	184±15
Nb	12.10±0.87	12.5±1
Cs	1.23±0.07	1.16±0.07
Ba	714.38±41.86	683±7
La	24.39±2.01	24.7±0.3
Ce	53.16±3.36	53.3±0.5
Pr	6.64±0.62	6.7±0.4
Nd	27.76±3.29	28.9±0.3
Sm	6.24±0.9	6.59±0.07
Eu	1.87±0.24	1.97±0.02
Gd	6.30±1.0	6.71±0.07
Dy	5.96±1.11	6.44±0.06
Er	3.35±0.53	3.7±0.04
Yb	3.07±0.59	3.39±0.03
Lu	0.46±0.08	0.503±0.005
Hf	4.77±0.66	4.84±0.28
Ta	0.72±0.06	0.78±0.06
Pb	12.19±1.93	11±1
Th	5.69±0.75	5.9±0.3
U	1.82±0.22	1.69±0.12
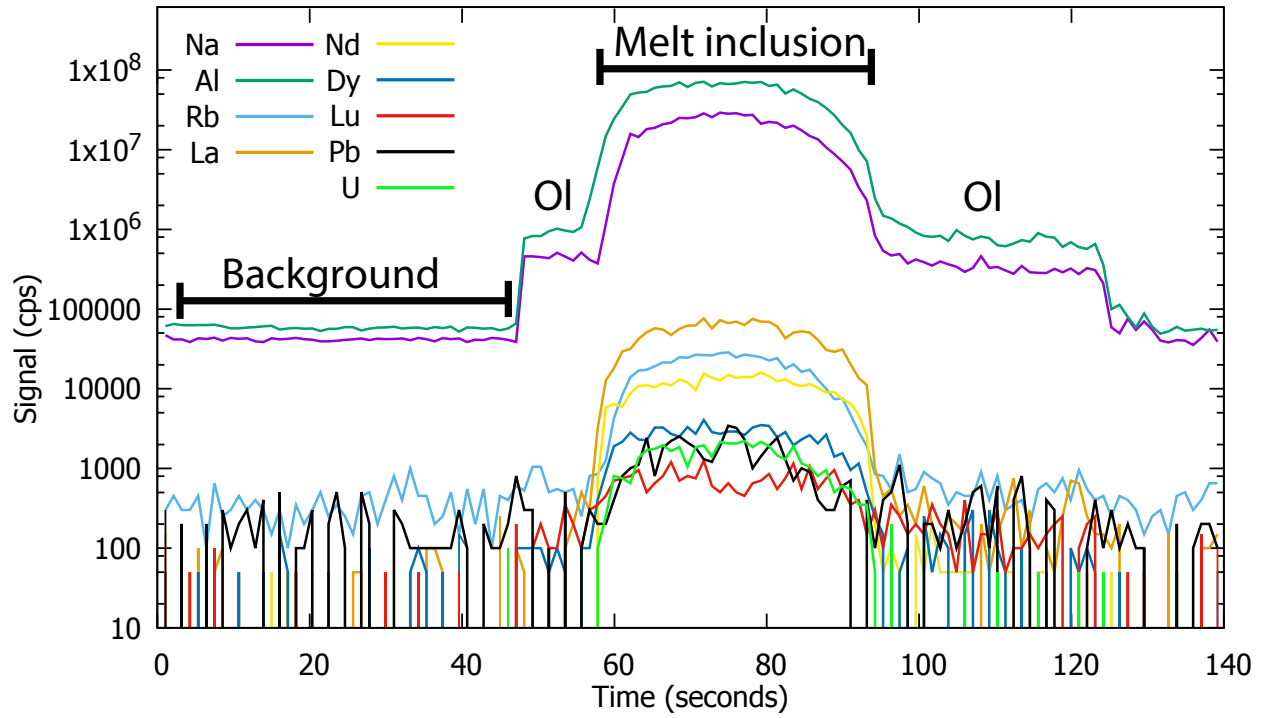
Figure 13: Representative LA-ICPMS signal of melt inclusion 167 of sample 97Syr1, located under the surface of the crystal. Selected elements show transition from olivine to melt inclusion and back. 'Background', 'Ol' (olivine), and 'Melt inclusion' intervals are included to indicate the ablated phase.

dard for trace element concentrations, measured as [43]Ca. Melt inclusions were instead normalised to CaO concentrations of 10 wt%, as based on the Syrian whole-rock array by *Krienitz et al.* (2007). Due to the semi-quantitative nature of the resulting values, trace elements are only discussed in terms of ratios.

6 Results

6.1 Whole-rock chemistry

Whole-rock data obtained by microprobe indicates samples 00Syr1 and 00Syr2 to match the geochemical signature of alkali basalts (Figure 14), with an overall similar composition to previous data from the Syrian Harrat al-Shamah (Figure 14, 15). HAS data from geographically close Israel most notably varies from the Syrian samples in terms of FeO, which is observed to be up to 2 wt% more abundant in my samples than similarly evolved, otherwise chemically similar Israeli samples (Figure 15). This high iron content also distinguishes my data from the intraplate volcanics from Yemen [*Baker et al.*, 1997], which are otherwise chemically similar (Figure 15). Sample 00Syr4, plotting near basanite compositions (Figure 14), is chemically dissimilar to all other samples. The adjusted data plots at significantly higher MgO compared to the other samples, and includes multiple wt% less SiO_2 and Al_2O_3. In comparison to other datasets,

Figure 14: Total alkali-silica classification diagram after *Bas et al.* (1986). Alkali-Sub alkali boundary based on *Miyashiro* (1978). Plotted data as in Table 4. Overlays from Syrian north-eastern (NE) and Harrat al-Shamah (HAS) regions from *Krienitz et al.* (2009) and *Krienitz et al.* (2007), respectively. Israel data from *Weinstein et al.* (2006), Yemen field based on *Baker et al.* (1997). ^{3}He rich Afar plume data is represented by Ethiopian lavas from *Pik et al.* (1998) and *Pik et al.* (1999).

Table 4: Whole-rock data defined by average of five glass measurements individually normalized by adjustment coefficient found in Table 2. All iron is documented as being ferrous, noted FeO_T.

Sample	00Syr1	00Syr2	00Syr4
SiO_2	46.96	47.53	45.19
TiO_2	2.62	2.49	2.89
Al_2O_3	16.66	16.80	14.87
FeO_T	12.80	12.20	13.27
MnO	0.14	0.19	0.31
MgO	6.94	6.81	10.53
CaO	9.89	9.89	9.20
Na_2O	3.18	3.05	2.43
K_2O	1.00	1.01	1.27
P_2O_5	0.50	0.58	0.77
Total	100.69	100.54	100.73

this sample is most similar to either the NE Syrian compositions or those of the Ethiopian Afar plume derived lavas (Figure 15). Given the oxides in question and the contact of this sample to a xenolith (see section 4, Studied samples), this deviation may represent olivine contamination during fusion bead preparation. The other samples deviate from the dataset of *Krienitz et al.* (2007) primarily in terms of SiO_2 and Al_2O_3, which are both measured at or above the highest documented values in their dataset. While the samples do present overlap with the less magnesian parts of the Afar dataset for some oxides, the significant TiO_2 content and low Al_2O_3 and
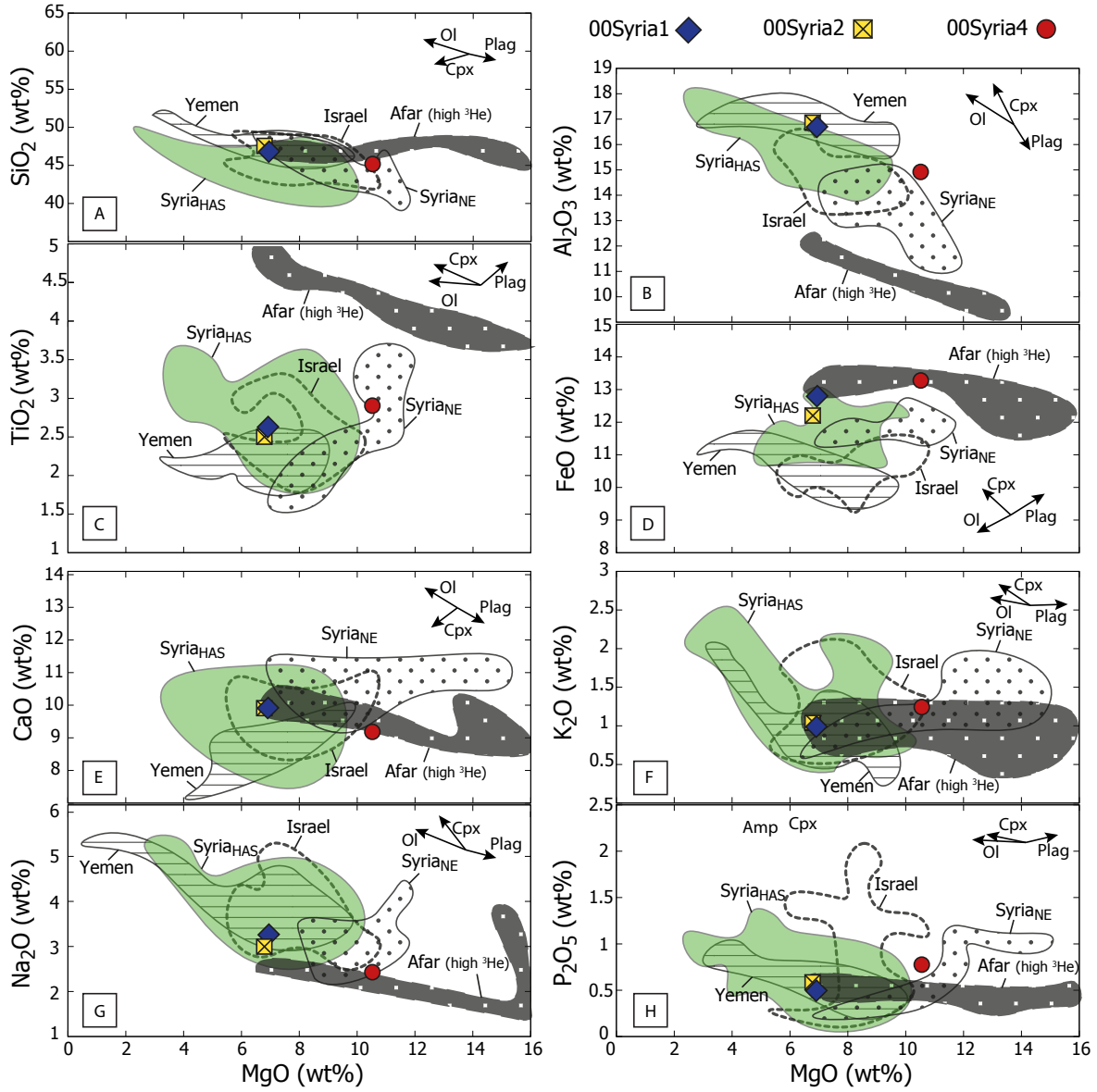
Figure 15: Harker diagrams for the three whole-rock samples analysed in this study. Overlays from Syrian north-eastern (NE) and Harrat al-Shamah (HAS) regions from *Krienitz et al.* (2009) and *Krienitz et al.* (2007), respectively. Israel data from *Weinstein et al.* (2006), Yemen field based on *Baker et al.* (1997). ^3He rich Afar plume data is represented by Ethiopian lavas from *Pik et al.* (1998) and *Pik et al.* (1999).

21

alkali content of these rocks clearly offsets them from ours (Figure 14, 15). Little to no overlap is observed between my rocks and those from the north-eastern parts of Syria, indicating a clear distinction between the two volcanic provinces.

6.1.1 Trace elements

Table 5: Trace element concentrations in ppm of whole-rock glasses, representing the mean of two analyses per sample.*: Due to an anomalous uranium peak in the first 00Syr1 measurement (see Figure 16), the second measured concentration is documented instead of the mean.

Element	00Syr1	00Syr2	00Syr4
V	262.90	231.15	194.36
Cr	91.11	93.65	315.28
Ni	91.12	84.95	300.74
Rb	12.35	13.88	18.29
Sr	793.59	992.47	1848.78
Y	20.70	23.01	22.35
Zr	186.26	201.36	309.43
Nb	25.56	27.97	64.89
Cs	0.06	0.07	0.42
Ba	184.12	200.52	750.64
La	24.24	26.64	48.37
Ce	50.61	54.95	92.02
Pr	6.68	7.00	10.78
Nd	30.44	31.59	44.94
Sm	6.92	7.14	9.66
Eu	2.53	3.14	3.16
Gd	7.28	7.68	8.53
Dy	6.20	6.55	6.50
Er	2.98	3.22	2.75
Yb	2.39	2.67	2.32
Lu	0.29	0.32	0.26
Hf	5.50	5.66	8.01
Ta	2.67	2.87	5.63
Pb	4.55	4.32	6.09
Th	2.01	2.22	5.90
U	0.53*	0.45	1.61

Trace element concentrations of the Syrian whole-rock samples agree well with alkali-basalt samples described by (Figure 16) *Krienitz et al.*, 2007]. Samples 00Syr1 and 00Syr2 are virtually identical in overall trace element enrichment, while sample 00Syr4 is noticeably enriched in comparison (Figure 16). This observation is in conflict with the assumption of olivine contamination affecting this sample, as was interpreted from major element data. I am therefore led to believe that this is a primary feature of the sample. The variable degrees of overall enrichment plot the latter sample close to previously described Syrian basanites, similar to OIB compositions [*McDonough & Sun*, 1989]. The two more depleted samples closely resemble alkali basalts from this area (Figure 16), and present degrees of enrichment slightly higher than Iranian P-MORB basalts [*Saccani et al.*, 2013b], particularly in terms of LREE and HREE. Notable element concentrations from the two more depleted samples in disagreement with previous literature include Pb, Sr, and Eu, all of which are significantly enriched compared to literature-based alkali basalt data. More disagreement exists between sample 00Syr4 and the basanite array, presenting an overall increased divergence from the high [3]He Afar lavas [*Pik et al.*, 1999]. Notable anomalies in this sample include increased concentrations of Ba, Th, Nb, Pb, and Sr, as well as significantly lower concentrations of Rb and Ti. This titanium depletion is particularly contrasting with the Ti-rich Ethiopian plume lavas (Figure 16). Crustal contamination sensitive ratios Ce/Pb and Nb/U, which have distinctly different values in mantle rocks and continental crust [*Hofmann et al.*, 1986], are displayed for my samples in Figure 17. All of the whole-rock glasses display slightly depleted Ce/Pb ratios compared to uncontaminated oceanic basalts. This is pri-
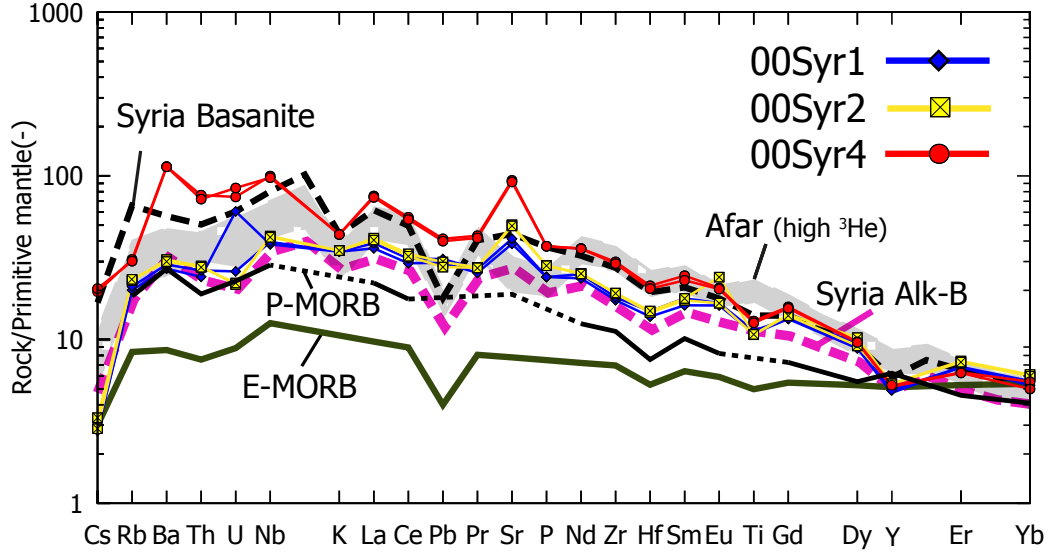
Figure 16: Primitive mantle normalised trace element diagram for whole-rock glasses as measured by LA-ICPMS in order of low to high incompatibility. Syrian alkali basalt and basanite lines (dashed; pink and black, respectively) are based on an average compositions from *Krienitz et al.* (2007). Afar (high ^{3}He) array represents high ^{3}He lavas from *Pik et al.* (1999). E-MORB and P-MORB lines (dark green, black; continuous) are based on *Sun &Mcdonough* (1989) and [*Saccani et al.*, 2013a]. Primitive mantle composition used for normalization as in *Mcdonough & Sun* (1995).
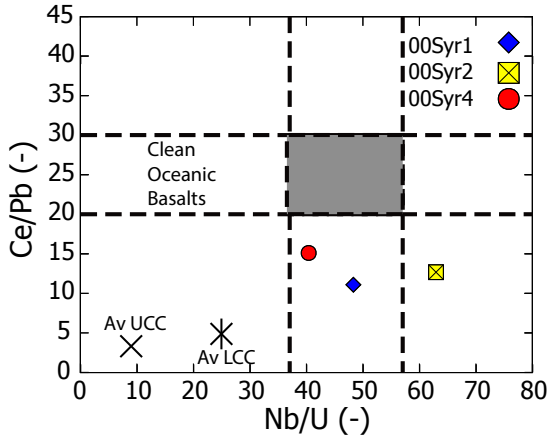
Figure 17: Crustal contamination sensitive Ce/Pb versus Nb/U ratios of mean whole rock glass measurements (Table 5). Average upper (UCC) and lower (LCC) continental crust ratios are included for reference, based on *Rudnick & Fountain* (1995). Oceanic basalt range representing mantle rocks is based on *Hofmann et al.* (1986).

marily a reflection of the elevated Pb concentrations observed in all of my samples, and could be indicative of crustal input. However, based on the uncontaminated (00Syr1,00Syr4) and elevated (00Syr2) Nb/U ratios of my samples, I infer that it is unlikely for these to have been subject to significant assimilation of crustal material.

6.2 Mineralogy

6.2.1 Olivine

Olivine is a common phenocryst phase in all samples, composing up to 5% of the total volume of the rock. Grains are commonly fractured, with localised serpentinization at the contact with groundmass and along fracture planes. The mineral is found in clusters, as well as isolated. Single
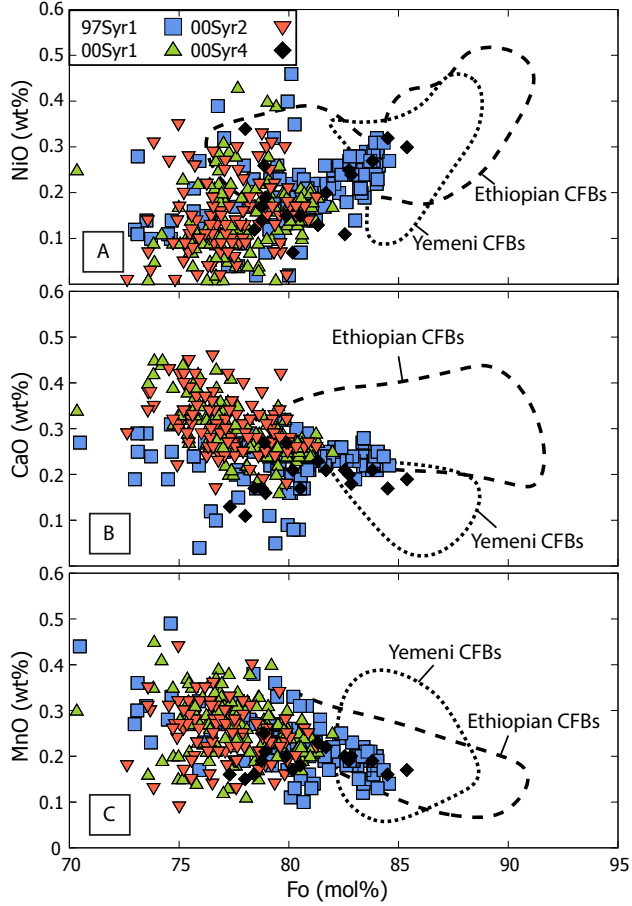
Figure 18: Olivine NiO (A),CaO (B), and MnO (C) concentrations versus forsterite content. Representative fields are added for olivine from Afar plume related Ethiopian and Yemeni CFB picrites from *Natali et al.* (2006).

minerals vary in size significantly, with a maximum diameter of 2 mm found in thin section, whereas specimens of up to 5 mm have been found in the crushed rock samples. The largest volume of analysed olivines is from the diameter size range of 0.2 to 0.5 mm. Inclusions in olivine are common and include fluid, feldspar, spinel, and melt. Analysed olivines contain a large range of forsterite contents $[Fo = \frac{Mg}{[Mg+Fe]}]$ ranging from approximately 64 to 85, with a

mode and mean of 76.47 and 78.28 (N=412, 1σ=3.08), respectively. A representative list of olivine analyses is found in the Tables 6 and 7, and a complete list is included in the Electronic Appendix. The most diverse population of crystals is found in sample 97Syr1. The main cluster of this specimen contains Fo values of 73.1 to 84.6 mol%, and NiO contents of 0 to 0.46 wt%, respectively. Few crystals with down to 63.9 mol% forsterite have also been documented. Nickel is positively correlated in the main cluster of this sample set (0.32 wt% NiO at Fo=84,0.09 wt% NiO at Fo=73.8), following a similar trend to that observed in Yemeni and Ethiopian lavas (Figure 18A). This range approximately matches with the two nearly identical sets from samples 00Syr1 and 00Syr2, which range in NiO from 0 to 0.43 wt%, lacking correlation with the stricter Fo range of approximately 73.6 to 82 mol% (Figure 18). The small (N=19) olivine set of 00Syr4 contains comparatively magnesium-rich olivine (Fo=77.3-85.4), and shows a weakly positive correlation with NiO (0-0.34 wt%) on a trend-line comparable to that of Yemeni and Ethiopian samples. The highest calcium concentrations were measured in olivine from samples 00Syr1 and 00Syr2 (0.16-0.46 wt% CaO), both of which contain near identical data sets (Figure 18A). A negative correlation between calcium and forsterite content have be observed in these samples. Conversely, the more calcium depleted samples 97Syr1 and 00Syr4 (0.04-0.31 and 0.11-0.23 wt% CaO, respectively) appear to largely lack this trend (Figure 18A). Manganese concentrations are more homogeneously distributed among the four populations, stretching from roughly 0.1 to 0.45 in all data sets (Figure 18B). While significant scatter is observed in the 2000 samples, a negative correlation with Fo can be observed primarily

in 97Syr1, at a similar slope to that observed in olivine from Oligocene Ethiopian continental flood basalts (CFB) (Figure 18) [*Natali et al., 2006*] . Olivine crystals in the dataset are generally less magnesian than those found in both Ethiopian and Yemeni CFB picrites and basalts (Figure 18) [*Natali et al., 2006*]. Nevertheless, some overlap is found between the least forsteritic olivine of the Ethiopian type and few magnesium rich olivine from all four of my data sets in both CaO and MnO. Yemeni derived olivine provides less overlap, limited to samples 97Syr1 and 00Syr4 (Figure 18).

6.2.2 Spinel

Spinel inclusions occur in roughly a third of all analysed olivine and are most common in the grains from 97Syr1. Inclusion diameters rarely exceed 100 μm. The olivine from sample 00Syr4 contains no valid spinel inclusions. A list of rep-

Figure 20: Plot of spinel TiO_2 vs Al_2O_3 for all spinel inclusions pairs. Fields representative of Arc, OIB, and MORB magmatic spinels are included, based on *Kamenetsky et al.* (2001).

resentative spinel inclusions is given in Tables 6 and 7, and a full list can be found in the Electronic Appendix. Inclusions have Cr# $[\frac{Cr}{Al+Cr}]$ values between 0.03 and 0.38, with a median and mean of 0.28 and 0.27, respectively (N=100, 1σ=0.06). No clear correlation is found between host olivine forsterite content and the spinel Cr# in my samples (Figure 19). The least chromium rich spinel are all found in sample 97Syr1, while those from the 2000 samples are clustered at the higher end of the dataset, partially overlapping the highest 97Syr1 values. No inclusions show overlap with the mantle array, but given the subhorizontal trend, they are most closely related to mantle data from the Red Sea and Syria, disregarding the higher host Fo content (Figure 19). To estimate more primitive mantle compositions, a trend-line is listed, giving an estimate of mantle olivine forsterite content for this area, being approximately 88-89 Fo. Compared to xenolith data from the Ethiopian plume related flood basalts, my spinel data shows significantly higher Cr#, even more so when assuming gradual increase with Fo (Figure 19). Negative correlations can be observed between Fo and TiO_2, FeO, and MnO, whereas SiO_2, Al_2O_3,

Figure 19: Plot of spinel Cr# $[\frac{Cr}{Al+Cr}]$ vs host olivine Fo $[\frac{Mg}{[Mg+Fe]}]$ for all spinel-olivine pairs. OSMA (Olivine-Spinel Mantle Array) for spinel peridotites is included as from *Arai* (1994). For comparison, domains are shown for xenoliths from the Syrian HAS, Ethiopian continental flood basalt (CFB) province, and the Ethiopian rift, as well as for peridotites from the Red Sea. Data for respective fields is from *Sharkov et al.* (1996), *Nasir & Safarjalani* (2000), and *Ismail et al.* (2008), *Beccaluva et al.* (2011) (Ethiopia), and *Bonatti et al.* (1986) (Red Sea).

Table 6: List of representative spinel inclusions and their olivine host grains measured by EMPA. All iron measured as FeO. FeO* and $Fe_2O_3^*$ represent iron recalculated based on stoichiometry.

Sample	97Syr1										00Syr1		
Grain #	12	29	54	80	98	140	185	190	209	223	16	28	65
Host olivine													
SiO_2	39.13	39.18	39.38	39.33	38.85	39.26	38.48	38.71	38.77	39.11	38.72	38.89	37.91
Cr_2O_3	0.05	0.05	0.05	0.08	0.02	0.06	0.01	0.02	0.03	0.06	0.04	0.02	n.d.
FeO	15.66	14.93	15.30	15.84	17.67	15.19	19.08	18.67	17.88	16.20	18.58	18.71	19.25
MnO	0.22	0.17	0.21	0.18	0.21	0.13	0.23	0.26	0.20	0.23	0.25	0.25	0.29
MgO	44.18	44.30	44.15	43.79	41.85	44.89	41.70	41.53	42.57	43.61	41.71	41.79	40.92
CaO	0.24	0.24	0.25	0.24	0.22	0.25	0.23	0.24	0.24	0.25	0.26	0.24	0.26
NiO	0.24	0.26	0.26	0.28	0.20	0.29	0.23	0.14	0.17	0.27	0.17	0.17	0.20
Fo (mol%)	83.41	84.10	83.72	83.13	80.85	84.05	79.57	79.86	80.93	82.75	80.01	79.93	79.12
Spinel inclusions													
SiO_2	0.13	0.11	0.18	0.17	0.11	0.15	0.10	0.14	0.12	0.13	0.14	0.10	0.09
TiO_2	1.20	1.11	0.66	0.76	1.03	0.93	1.47	1.56	1.66	1.31	1.74	2.08	1.10
Al_2O_3	36.16	34.18	41.75	43.15	41.25	44.17	36.09	41.37	40.67	35.48	31.75	36.05	30.85
V_2O_3	0.26	0.17	0.19	0.15	0.24	0.19	0.20	0.24	0.26	0.24	0.27	0.24	0.28
Cr_2O_3	22.75	23.00	18.97	18.49	17.42	16.61	21.05	13.71	20.57	21.00	25.72	22.20	24.43
FeO_T	23.94	24.49	19.05	19.23	22.47	19.92	26.05	27.31	21.57	26.55	25.69	24.61	28.86
MnO	0.25	0.21	0.17	0.19	0.21	0.17	0.21	0.20	0.20	0.22	0.26	0.20	0.30
MgO	12.86	13.06	14.93	15.57	14.83	16.00	12.33	13.23	13.46	12.08	12.42	12.78	11.43
NiO	0.14	0.17	0.23	0.27	0.21	0.23	0.14	0.22	0.10	0.13	0.16	0.15	0.12
ZnO	0.19	0.10	0.19	0.09	0.07	0.10	0.07	0.24	0.20	0.21	0.29	0.15	0.18
Total	97.88	96.61	96.30	98.07	97.83	98.47	97.70	98.21	98.81	97.32	98.43	98.57	97.65
FeO*	18.08	17.14	14.85	14.81	15.84	14.65	19.29	18.73	18.59	19.14	18.59	19.26	19.28
$Fe_2O_3^*$	6.51	8.17	4.67	4.92	7.37	5.87	7.51	9.53	3.32	8.23	7.89	5.95	10.64
$Mg/(Mg+Fe^{2+})$	0.56	0.58	0.64	0.65	0.63	0.66	0.53	0.56	0.56	0.53	0.54	0.54	0.51
Cr/(Cr+Al)	0.30	0.31	0.23	0.22	0.22	0.20	0.28	0.18	0.25	0.28	0.35	0.29	0.35
Spinel Fe^{2+}/Fe^{3+}	3.09	2.33	3.53	3.35	2.39	2.77	2.85	2.18	6.22	2.59	2.62	3.60	2.01
Melt Fe^{2+}/Fe^{3+}	12.29	8.52	14.65	13.67	8.80	10.69	11.09	7.81	30.77	9.75	9.91	15.03	7.03

Table 7: Table 6 continued

Sample	00Syr1					00Syr2						
Grain #	101	132	142	143	157	50	128	164	173	181	254	269
Host olivine												
SiO_2	38.61	38.20	38.21	38.49	38.22	38.26	39.19	38.91	38.81	38.41	38.44	38.64
Cr_2O_3	0.03	0.01	0.02	0.02	0.01	0.03	0.04	0.02	n.d.	0.01	0.03	0.04
FeO	17.32	17.99	18.64	18.10	17.78	19.03	17.98	17.51	18.44	19.34	18.20	18.15
MnO	0.21	0.22	0.25	0.25	0.24	0.26	0.26	0.22	0.24	0.23	0.21	0.25
MgO	42.32	41.45	41.60	41.80	41.71	40.14	42.21	42.56	41.51	41.20	41.69	43.11
CaO	0.27	0.27	0.25	0.24	0.25	0.26	0.26	0.26	0.28	0.27	0.26	0.27
NiO	0.19	0.17	0.19	0.17	0.20	0.15	0.17	0.19	0.17	0.18	0.15	0.14
Fo (mol%)	81.33	80.42	79.91	80.46	80.70	79.00	80.71	81.25	80.05	79.15	80.33	80.89
Spinel inclusions												
SiO_2	0.11	0.11	0.09	0.09	0.20	0.12	0.10	0.70	0.14	0.07	0.12	0.14
TiO_2	2.12	1.92	0.89	0.93	2.28	1.29	1.45	1.13	2.11	1.35	2.22	1.26
Al_2O_3	32.30	33.42	36.49	35.23	34.38	32.16	34.31	36.26	37.34	32.09	34.92	37.16
V_2O_3	0.28	0.28	0.21	0.21	0.30	0.28	0.21	0.24	0.33	0.25	0.41	0.26
Cr_2O_3	21.58	20.89	21.01	21.00	21.76	22.47	23.33	21.77	20.54	22.24	20.48	20.35
FeO_T	27.93	27.42	25.98	27.52	26.27	28.58	26.02	23.10	24.04	29.66	26.42	25.11
MnO	0.25	0.26	0.23	0.24	0.21	0.30	0.26	0.27	0.22	0.24	0.24	0.25
MgO	12.55	12.61	13.50	12.70	13.07	11.72	13.02	13.42	13.04	11.70	12.11	13.35
NiO	0.11	0.12	0.18	0.15	0.12	0.12	0.13	0.14	0.17	0.12	0.11	0.13
ZnO	0.17	0.21	0.15	0.12	0.17	0.16	0.15	0.15	0.26	0.10	0.23	0.13
Total	97.40	97.23	98.73	98.21	98.77	97.21	98.97	97.19	98.18	97.82	97.28	98.15
FeO^*	18.73	18.50	17.22	18.18	18.94	19.14	18.20	17.73	18.81	19.51	19.72	17.76
$Fe_2O_3^*$	10.23	9.91	9.74	10.39	8.15	10.49	8.69	5.96	5.81	11.28	7.45	8.17
$Mg/(Mg+Fe^{2+})$	0.54	0.55	0.58	0.55	0.55	0.52	0.56	0.57	0.55	0.52	0.52	0.57
$Cr/(Cr+Al)$	0.31	0.30	0.28	0.29	0.30	0.32	0.31	0.29	0.27	0.32	0.28	0.27
Spinel Fe^{2+}/Fe^{3+}	2.04	2.07	1.97	1.94	2.58	2.03	2.33	3.31	3.60	1.92	2.94	2.42
Melt Fe^{2+}/Fe^{3+}	7.13	7.31	6.81	6.72	9.74	7.09	8.50	13.44	15.03	6.61	11.55	8.93

MgO, and NiO, as well as the Mg# correlate positively. Roughly all correlations with forsterite are more clearly expressed in the 2000 samples compared to 97Syr1. All spinel TiO_2 content is relatively high, with a minimum of 0.44 wt% but the majority of measurements exceeding 1 wt% TiO_2 (Figure 20). In TiO_2 vs Al_2O_3 space, the spinel measurements plot at the upper edge of the MORB-like magmatic spinel field, forming a sub-horizontal trend (Figure 20). A clear progression can be observed in this diagram, with spinel becoming more Al_2O_3 rich from sample 00Syr2 to 00Syr1 to 97Syr1, perhaps indicating a stronger expression of an OIB-like source component in the former samples (Figure 20).

6.2.3 Feldspar

Feldspar is observed inside olivine both as a melt inclusion phase, as well as in the form of isolated mineral inclusions, presumably trapped during crystallization. Figure 21 displays the chemical variation on the basis of SEM analysis within both populations of feldspar crystals as a function of host olivine forsterite content. A bimodal distribution is present, forming clusters of albitic alkali feldspar (Anorthoclase) and anorthitic plagioclase (Labradorite & Bytownite). The anorthitic plagioclase group contains a slight majority of solitary inclusions, which overall contain less orthoclase and albite fractions, but include the largest population of anorthite-rich feldspars. MI-contained feldspars have the largest population of albitic compositions, clustering at approximately 80 mol% regardless of host forsterite content. Anorthitic feldspar compositions are also observed in melt inclusions, the majority of which cluster at a composition of (An_{80}/Ab_{20}). Measurements were checked for correct stoichiometry in order to discard inaccu-
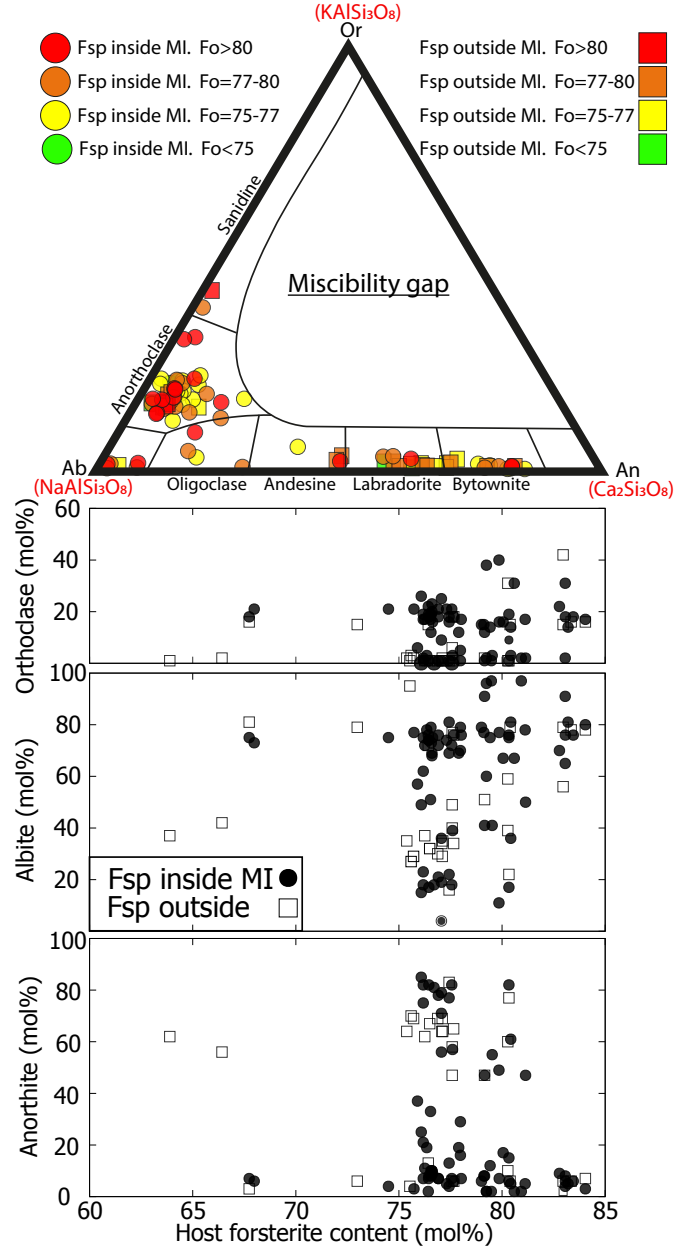
Figure 21: Data from isolated and melt inclusion contained feldspar crystals in terms of Orthoclase, Albite, and Anorthoclase molar percentages, compared to olivine-host forsterite content.

rate measurements. No clear correlation appears to be present between host forsterite content and feldspar composition within melt inclusions, as indicated by the relatively constant composition over the range of 75-85 Fo. However, isolated inclusions display a weak positive correlation between albite and forsterite content. A representative list of solitary feldspar inclusions is given in Table 8.

6.2.4 Pyroxene

Pyroxene mineral inclusions were also observed in olivine, but are significantly less abundant than feldspar and spinel. A total of three isolated pyroxenes were analysed, two from sample 97Syr1, included in olivine samples number 85 and 174, and one from sample 00Syr2, included in olivine number 134. These inclusions have Mg# values of 73.7, 74.2, and 45.9, respectively. Pyroxene crystals inside melt inclusions are more abundant, and cluster at Mg# values between 61.6 and 82.3 (median=73.68, $1\sigma=7.63_{N=23}$), with no apparent correlation with host forsterite content, which stretches between 73.59 and 80.33 (median=76.55, $1\sigma=3.14_{N=23}$). A representative list of pyroxene inclusions as found in MIs is given in Table 9.

6.3 Melt inclusions

6.3.1 Petrography

Olivine from all studied samples include melt inclusions, the smallest amount being found in sample 00Syr4, in which only 18 out of 308 olivine crystals are observed to contain inclusions. Out of the complete set of 1079 mounted olivine crystals, a total of 422 were seen to host melt inclusions, 62 of which are in contact with the polished surface, allowing for major element analysis. Inclusion sizes vary between 5 and 160 μm, though most vary between 15 and 50 μm. All observed melt inclusions are of recrystallized nature, with cryptocrystalline (Figure 22A) to microcrystalline (Figure 22B) crystals. Melt pockets frequently occur in clusters, sometimes at specific zones of the crystal, indicative of assimilation during specific growth stages. This is most common at the edges of the crystal. Nevertheless, solitary inclusions are not uncommon. Minerals formed in post-entrapment crystallization include both alkali and calcic feldspars, commonly representing the majority of the inclusion volume. Volumetrically smaller phases include (ulvo)spinel, (clino)pyroxene, and various unidentified phases which may represent leftover melt fractions.

6.3.2 Calculations and adjustments

Major element chemical analysis of melt inclusions is limited to EDx analysis by SEM on inclusions outcropping at the surface. The recrystallized nature of the melt pockets allows for a semi-quantitative image of the overall chemical composition of the inclusion. I recognize that the two-dimensional slice may not represent the three-dimensional mineral distribution, and therefore I evaluated each inclusion with regards to mineral over representation. To best estimate the overall composition, volume proportions for all phases were determined on the basis of BSE imagery, using image processing software tool Fiji by ImageJ [*Schindelin et al.*, 2015; *Schindelin et al.*, 2012]. On the basis of mineral proportions and compositions as measured by EDx on SEM, an overall composition was calculated. An example of this process is shown in Figure 22. Mineral proportions and calculated overall melt inclusion compositions are

Table 8: List of representative solitary feldspar inclusions and their olivine host grains measured by EMPA. All iron measured as FeO.

Sample	97Syr1					00Syr1				00Syr2	
Host olivine											
Grain #	26	34	84	115	202	6	114	137	201	248	254
SiO_2	39.26	38.92	36.54	38.41	36.76	37.60	37.86	38.39	38.03	38.01	38.44
Cr_2O_3	0.05	0.04	n.d.	0.02	n.d.	n.d.	0.05	0.02	0.03	n.d.	0.03
FeO	15.13	18.32	31.63	20.71	19.08	22.61	20.52	18.24	21.01	21.08	18.20
MnO	0.17	0.21	0.50	0.26	0.23	0.37	0.29	0.24	0.31	0.31	0.21
MgO	44.69	41.85	31.39	40.22	41.70	38.82	40.00	41.96	39.63	39.86	41.69
CaO	0.23	0.25	0.32	0.20	0.24	0.38	0.31	0.27	0.32	0.30	0.26
NiO	0.29	0.15	0.06	0.12	0.05	0.10	0.12	0.13	0.12	0.10	0.15
Fo (mol%)	84.04	80.28	63.89	77.58	67.56	75.38	77.65	80.39	77.08	77.12	80.33
Feldspar inclusions											
Feldspar type	Alk-Fsp	Alk-Fsp	Plag	Alk-Fsp	Alk-Fsp	Plag	Plag	Alk-Fsp	Plag	Plag	Plag
SiO_2	61.92	63.51	51.56	60.14	60.82	51.23	50.89	64.67	51.31	50.48	46.81
TiO_2	0.68	0.2	0.18	0.58	0.08	0.16	0.17	0.26	0.1	0.11	0.21
Al_2O_3	22.39	21.38	30.14	23.23	19.83	30.67	31.01	21.4	30.78	31.15	31.75
FeO	0.62	0.6	1.23	0.87	0.74	0.91	0.58	0.51	0.67	0.76	1.77
MnO	n.d.	n.d.	0.11	0.08	0.01	n.d.	0.01	0.01	0.09	0.10	n.d.
MgO	0.28	n.d.	n.d.	0.11	0.14	0.06	0.17	0.06	0.1	0.04	3.17
CaO	1.42	2.15	12.52	1.23	2.62	12.83	13.21	1.26	12.89	13.14	13.92
Na_2O	9.22	6.77	4.09	9.43	5.08	3.84	3.79	8.94	3.82	3.93	2.18
K_2O	2.80	5.36	0.13	3.30	8.64	0.29	0.18	2.62	0.23	0.21	0.15
P_2O_5	0.67	0.04	0.04	1.02	2.04	0.02	n.d.	0.27	n.d.	0.08	0.03
Orthoclase (mol%)	15.55	30.71	0.77	17.68	46.55	1.72	1.06	15.17	1.36	1.22	0.99
Albite (mol%)	77.83	58.95	36.87	76.79	41.60	34.53	33.81	78.70	34.43	34.69	21.86
Anorthite (mol%)	6.62	10.34	62.36	5.53	11.86	63.75	65.13	6.13	64.20	64.09	77.15

Table 9: List of representative pyroxene inclusions within melt inclusions, as well as their olivine host grains measured by EMPA. All iron measured as FeO.

| Sample	**97Syr1**			**00Syr1**				**00Syr2**				
Host olivine												
Grain #	15	84	108	46	126	158	226	21	41	72	181	208
SiO_2	37.96	36.54	38.92	38.11	37.70	37.84	38.10	37.61	37.73	38.33	38.41	38.52
Cr_2O_3	n.d.	n.d.	0.04	0.05	0.01	0.01	n.d.	0.01	n.d.	0.03	0.01	n.d.
FeO	22.02	31.63	17.65	23.07	22.00	21.30	21.41	23.72	21.46	20.68	19.34	19.07
MnO	0.32	0.50	0.14	0.35	0.29	0.34	0.27	0.35	0.28	0.33	0.23	0.25
MgO	38.90	31.39	42.61	38.26	38.09	39.20	39.20	37.08	38.92	39.54	41.20	41.27
CaO	0.22	0.32	0.25	0.39	0.32	0.35	0.32	0.38	0.34	0.30	0.27	0.29
NiO	0.13	0.06	0.21	0.09	0.14	0.13	0.13	0.07	0.10	0.11	0.18	0.17
Fo (mol%)	75.90	63.89	81.14	74.72	75.53	76.63	76.55	73.59	76.37	77.31	79.15	79.42
Pyroxene inclusions												
SiO_2	47.01	49.36	48.16	44.76	49.04	47.34	46.66	42.8	42.62	41.82	42.8	45.98
TiO_2	3.16	1.7	2.31	4.32	1.21	1.96	2.94	3.01	3.86	4.13	4.27	3.11
Al_2O_3	3.69	3.15	4.06	8.95	5.35	7.12	6.94	11.14	9.64	10.74	11.97	8.85
FeO	10.04	8.23	9.38	5.86	6.37	6.48	6.35	10.07	10.76	9.24	5.56	5.61
MnO	0.31	0.39	0.2	0.12	0.32	0.24	0.04	0.18	0.3	0.09	0.1	0.16
MgO	14.79	15.57	14.73	13.6	16.31	15.4	15.55	11.07	12.3	12.63	13.27	14.67
CaO	20.52	21.18	20.79	21.97	21.01	21.05	20.9	19.96	18.72	19.84	21.65	21.21
Na_2O	0.38	0.37	0.36	0.38	0.33	0.28	0.6	0.76	0.49	0.7	0.38	0.38
K_2O	0.09	n.d.	n.d.	n.d.	0.02	n.d.	n.d.	0.18	0.24	0.05	n.d.	0.02
P_2O_5	n.d.	0.05	n.d.	0.04	0.03	0.12	0.03	0.82	1.07	0.77	n.d.	0.01
Mg#	72.42	77.13	73.68	80.53	82.03	80.90	81.36	66.21	67.08	70.90	80.97	82.34
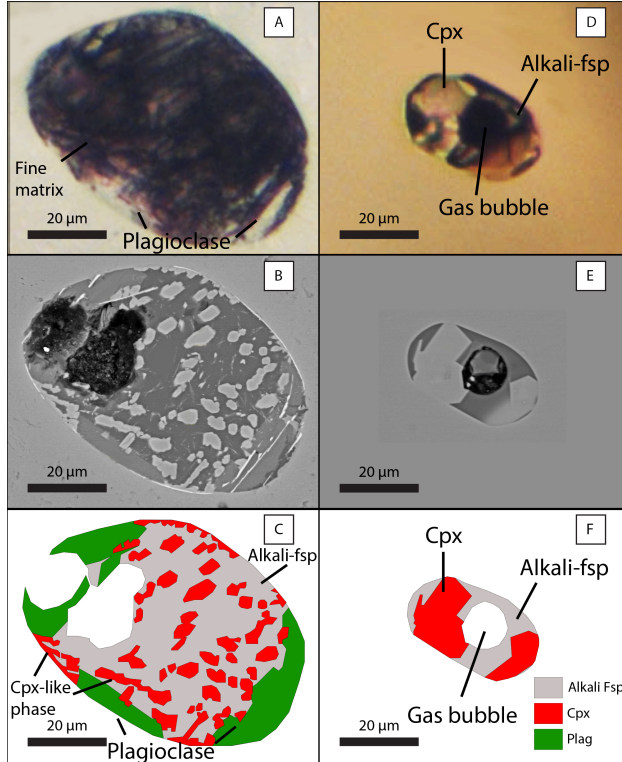
Figure 22: Representative examples of melt inclusions found on the mount surface, showing cryptocrystalline (A) (Olivine 00Syr1-21) and microcrystalline (D) (Olivine 00Syr2-208) examples, as observed in transmitted light. Volume calculation based on BSE imagery is visualised, as discussed in text.

listed in Tables 10-13. Melt inclus ions are frequently observed to contain less FeO and more MgO than their host rock. This is attributed to re-equilibration between host and inclusion during cooling of the magma, and occurs on month-, to year time scales [*Danyushevsky et al.*, 2000]. This process is termed 'FeO loss', and can be assumed to impact a majority of natural systems, especially when considering early crystallizing phases [*Danyushevsky et al.*, 2000]. To compensate for this, I applied the technique by *Danyushevsky et al.*, (2000). Compositions were re-equilibrated with their host olivine crystals using PETROLOG3 [*Danyushevsky & Plechov*, 2011]. In order to utilise an appropriate Fe^{2+}/Fe^{3+} ratio for the procedure, the measured spinel Fe^{2+}/Fe^{3+} ratios were used in combination with the melt-spinel equilibrium model by *Maurel & Maurel*, (1982). As such I used an FeO (total) content of 11.5 wt% as representative for all melt inclusions, and an Fe^{2+}/Fe^{3+} ratio of 7.0. Crystallization temperatures were determined using the melt-olivine equilibrium model of *Ford et al.* (1983). The correction most significantly affects iron and magnesium content in the melt inclusion, thereby conserving geochemical trends observed in other major oxides. Fully re-equilibrated compositions are listed in Tables 10-13.

6.3.3 Major elements

Tables 10-13 list the set of calculated melt inclusion compositions, excluding those which include >10 volume% of Cr-Spinel. Unequilibrated constituent oxide measurements are plotted relative to host olivine Fo and MgO in Figures 23 and 24, while Figures and 25 to 28 display re-equilibrated compositions relative to MgO, K_2O, and host forsterite, respectively. Non-equilibrated compositions are frequently offset from whole-rock HAS data collected by *Krienitz et al.* (2007) (Figure 24). This is most strongly expressed in oxides FeO, Al_2O_3, and SiO_2, and can in part be related to re-equilibration with the host olivine grain. Forsterite-relative plotting indicates scarce correlation between host olivine compositions and their included melts, presenting weak positive correlations observed with CaO and TiO_2, associated with an increased abundance of clinopyroxene. Melt contained MgO-relative diagrams present more convincing trends in SiO_2, Al_2O_3, and Na_2O (neg-

ative), as well as FeO and arguably CaO (positive). Exempting CaO, these patterns are consistent with olivine fractionation. While 97Syr1 covers a limited MgO range with regards to unequilibrated compositions (1.77-7.24 wt%), equilibration corrects this to the largest MgO range between the samples (2.94-8.10 wt%), consistent with olivine forsterite variation. Unlike spinel measurements, a clear distinction exists between melt samples 00Syr1 and 00Syr2 (MgO=0.84-8.16 wt% & 0.24-14.02 wt%), with 00Syr2 including significantly more magnesian inclusions. However, this disparity does not hold post-equilibration (MgO=4.88-6.5 wt% & 4.41-6.75 wt%) (Table 11-13), reaffirming the compositional similarity of these samples. The re-equilibrated compositions show increased, albeit selective agreement with the whole rock dataset. Despite the large compositional range in my measurements (e.g. SiO_2=40.85-54.37 wt%, Al_2O_3=15.46-22.67 wt%, CaO=0.99-18.7 wt%), clear clustering is observed with respect to the major oxides and few trend lines can be distinguished. Not unlike non-equilibrated compositions, my melt inclusion data consistently plots at higher SiO_2, Al_2O_3, and Na_2O, and lower TiO_2, MnO, and CaO values compared to whole-rock arrays from nearby volcanic provinces. Remaining oxides K_2O and P_2O_5 largely agree with the Syrian Harrat al-Shamah compositions (Figure 25). This pattern is interpreted as partly reflecting an over-representation of sodic feldspar in the estimated volume distribution. Inclusions with CaO content lower than that of the Syrian whole-rock array of *Krienitz et al.* (2007) are therefore listed as a separate 'low Ca' group (Figure 25-27). Additionally of note are four inclusions of especially high CaO, and low Na_2O concentrations. These inclusions include a significant proportion of cpx, or cpx-like unidentified

components (Table 10-13). Mild negative correlations are observed between MgO and SiO_2, Al_2O_3, P_2O_5, and both alkali metal oxides. As the alkali metal trends are most notable in low Ca samples, this is likely an artefact of the volume calculation. Less population diversity is observed in trends relative to K_2O (Figure 26). SiO_2, CaO, and Na_2O correlate positively with K_2O in the low Ca group, affirming the assumption that this group is significantly influenced by feldspar proportions. Forsterite relative diagrams show a similar pattern to those relative to MgO, which is consistent with the positive correlation between the two (Figure 27, 28).

6.3.4 Entrapment temperatures

Compositionally inferred crystallization temperatures show a negative correlation with CaO for all inclusions (Figure 29A). Conversely, temperature and host olivine forsterite content are positively correlated, especially when only considering the selected CaO interval (Figure 29B). It is evident that the melt inclusions have been trapped across a diverse range of temperatures (1064-1342 °C). However, excluding samples that fall outside of the whole-rock CaO range imposes an upper temperature limit of 1249 °C. The positive linkage between forsterite and entrapment temperature is consistent with fractionation control in the system, indicating that the melts trapped into the surface inclusions have been subject to variable degrees of crystal fractionation prior to entrapment. As my collection of calcium-fit surface inclusions is limited to a maximum host olivine forsterite content of 83.45 mol% (Table 8, grain 143), which is significantly lower than the mantle equilibrated array [*Arai*, 1994], all of the sampled melts represent fractionated magma compositions.

Table 10: List of surface melt inclusions and their host olivine, adjusted for FeO loss. T=Crystallization temperature, method explained in text. *Host olivine composition not measured by EMPA.

Sample	97Syr1												
Grain #	15	47	64	67	82	84	108	133	143	158	179	190	205
Host Olivine													
SiO_2	37.96	37.14	38.40	38.32	37.06	36.54	38.92	37.74	39.31	39.12	38.84	38.71	38.79
Cr_2O_3	n.d.	0.02	n.d.	n.d.	0.02	n.d.	0.04	n.d.	0.02	0.09	0.04	0.02	0.04
FeO	22.02	28.66	21.81	20.68	28.25	31.63	17.65	23.35	15.54	15.77	17.64	18.67	18.14
MnO	0.32	0.44	0.24	0.27	0.43	0.50	0.14	0.28	0.17	0.19	0.21	0.26	0.20
MgO	38.90	33.76	39.70	40.34	33.64	31.39	42.61	38.24	43.96	43.84	42.50	41.53	42.24
CaO	0.22	0.11	0.12	0.21	0.28	0.32	0.25	0.19	0.25	0.24	0.23	0.24	0.26
NiO	0.13	0.11	0.14	0.09	0.09	0.06	0.21	0.11	0.19	0.21	0.22	0.14	0.19
Fo	75.90	67.74	76.44	77.66	67.98	63.89	81.14	74.49	83.45	83.20	81.12	79.86	80.59
Mineral Volumes													
Plag (V%)	87						73						
Alk-Fsp (V%)		86	55	76	70			80	55	55	65	55	90
Cpx (V%)	13					20	27						
Misc. (V%)		14	45	24	30	80		20	45	45	35	45	10
Inclusion composition													
SiO_2	53.69	54.75	49.77	51.63	47.37	49.59	50.20	54.35	50.30	51.02	51.86	49.32	52.23
TiO_2	0.61	0.51	4.33	0.69	3.25	0.64	0.82	1.39	2.65	2.63	2.05	2.64	1.61
Al_2O_3	24.70	22.83	20.35	23.26	23.28	18.63	23.26	22.28	18.63	20.34	20.72	19.56	25.27
FeO	2.21	2.48	4.96	4.00	7.08	7.91	3.64	1.81	3.12	3.20	2.70	3.88	2.21
MnO	0.25	0.12	0.08	0.18	0.20	0.42	0.14	0.02	0.30	0.05	0.08	0.04	0.01
MgO	2.05	2.61	6.95	6.24	3.97	7.24	4.24	2.78	6.60	5.68	4.79	6.20	1.77
CaO	9.23	4.00	5.37	3.62	4.04	8.87	12.64	4.90	10.36	9.90	8.04	10.20	1.25
Na_2O	5.89	8.33	5.82	7.15	7.55	4.57	4.49	8.01	5.40	5.31	6.65	5.70	8.64
K_2O	0.81	2.79	1.76	2.27	2.89	2.24	0.28	2.99	1.68	1.15	1.91	1.61	5.46
P_2O_5	n.d.	0.70	0.60	0.66	0.63	0.02	0.02	0.57	0.48	0.32	0.57	0.50	0.77
Total	99.43	99.11	99.98	99.70	100.26	100.12	99.73	99.09	99.52	99.60	99.37	99.66	99.20
Re-Equillibrated													
SiO_2	49.77	51.52	47.86	49.24	46	49.04	47.19	50.71	47.44	47.89	48.64	46.98	48.64
TiO_2	0.49	0.44	4	0.62	3.06	0.66	0.66	1.15	2.2	2.14	1.68	2.3	1.28
Al_2O_3	19.72	19.56	18.81	20.79	21.89	19.14	18.84	18.42	15.46	16.58	17.02	17	20.09
Fe_2O_3	1.6	1.6	1.6	1.6	1.6	1.59	1.6	1.6	1.6	1.6	1.6	1.61	1.6
FeO	10.08	10.07	10.11	10.08	10.11	9.98	10.11	10.08	10.08	10.06	10.08	10.11	10.08
MnO	0.2	0.1	0.07	0.16	0.19	0.43	0.11	0.02	0.25	0.04	0.07	0.03	0.01
MgO	5.43	3.15	5.02	5.26	2.94	3.03	7.37	4.41	8.1	8.09	6.81	6.31	5.48
CaO	7.37	3.43	4.96	3.24	3.8	9.11	10.24	4.05	8.6	8.07	6.6	8.87	0.99
Na_2O	4.7	7.14	5.38	6.39	7.1	4.7	3.64	6.62	4.48	4.33	5.46	4.96	6.87
K_2O	0.65	2.39	1.63	2.03	2.72	2.3	0.23	2.47	1.39	0.94	1.57	1.4	4.34
P_2O_5	n.d.	0.6	0.55	0.59	0.59	n.d.	n.d.	0.47	0.4	0.26	0.47	0.43	0.61
T(°C)	1170	1180	1199	1252	1154	1064	1194	1220	1249	1246	1243	1199	1342

Table 11: Continued list of surface melt inclusions and their host olivine, adjusted for FeO loss. T=Crystallization temperature, method explained in text. *Host olivine composition not measured by EMPA.

Sample	**97Syr1**	**00Syr1**										**00Syr2**	
Grain #	228	46	65	126	132	150	158	175	182	224	226	7	17
Host Olivine													
SiO_2	38.93	38.11	37.91	37.70	38.20	38.12	37.84	37.59	37.59	38.13	38.10	38.13	38.26
Cr_2O_3	0.04	0.05	n.d.	0.01	0.01	n.d.	0.01	0.03	0.02	n.d.	n.d.	n.d.	n.d.
FeO	16.18	23.07	19.25	22.00	17.99	21.58	21.30	21.72	21.48	20.56	21.41	21.29	21.26
MnO	0.19	0.35	0.29	0.29	0.22	0.29	0.34	0.33	0.27	0.27	0.27	0.28	0.27
MgO	43.65	38.26	40.92	38.09	41.45	38.87	39.20	38.76	38.90	39.86	39.20	39.11	39.28
CaO	0.24	0.39	0.26	0.32	0.27	0.32	0.35	0.35	0.32	0.31	0.32	0.34	0.31
NiO	0.28	0.09	0.20	0.14	0.17	0.11	0.13	0.09	0.13	0.09	0.13	0.09	0.13
Fo	82.78	74.72	79.12	75.53	80.42	76.25	76.63	76.08	76.35	77.56	76.55	76.60	76.70
Mineral Volumes													
Plag (V%)					30			58					27
Alk-Fsp (V%)	45		69	74	64	79	51	33	70	60	72	95	60
Cpx (V%)		35		26		21	49	9	30	22	28		8
Misc. (V%)	55	65	31		7					18		5	5
Inclusion composition													
SiO_2	48.27	49.50	52.95	54.70	53.93	54.68	49.99	48.10	55.80	53.61	54.33	56.83	51.46
TiO_2	3.55	1.63	2.78	0.46	0.67	0.66	1.21	0.90	1.77	1.18	1.15	0.36	0.47
Al_2O_3	19.08	21.74	22.42	20.21	27.40	21.84	17.23	28.74	19.68	22.90	20.08	23.41	25.30
FeO	4.57	3.12	3.54	2.71	1.02	2.39	4.16	1.27	2.32	1.65	2.91	1.45	1.71
MnO	0.11	0.05	0.12	0.14	0.05	0.09	0.20	0.07	0.07	0.02	0.01	0.09	0.07
MgO	6.94	5.29	3.73	5.56	1.03	1.77	8.16	0.84	3.22	1.66	5.12	0.24	0.75
CaO	11.98	13.71	5.29	6.04	5.89	6.66	11.29	13.91	8.45	9.78	7.47	2.69	7.50
Na_2O	3.58	0.54	6.62	8.92	7.87	8.01	5.20	3.41	7.29	6.03	6.28	8.72	6.07
K_2O	1.34	3.78	1.69	0.18	1.67	2.50	1.46	1.52	0.56	1.96	1.24	4.00	2.25
P_2O_5	0.39	0.03	0.45	0.47	0.65	0.46	0.62	0.58	0.06	0.30	0.61	0.88	0.58
Total	99.81	99.37	99.59	99.39	100.19	99.06	99.50	99.35	99.24	99.09	99.22	98.67	96.15
Re-Equillibrated													
SiO_2	46.05	47.08	49.66	51.62	48.91	50.79	48.18	45.01	51.85	49.55	51.21	52.1	49.04
TiO_2	3.04	1.41	2.3	0.4	0.5	0.53	1.13	0.69	1.45	0.92	0.99	0.28	0.38
Al_2O_3	16.36	18.79	18.58	17.65	20.39	17.59	16.05	22.06	16.15	17.91	17.22	18.22	20.23
Fe_2O_3	1.6	1.6	1.6	1.6	1.6	1.61	1.6	1.6	1.6	1.6	1.6	1.61	1.61
FeO	10.1	10.09	10.1	10.1	10.09	10.13	10.08	10.1	10.08	10.08	10.09	10.17	10.11
MnO	0.09	0.04	0.1	0.12	0.04	0.07	0.19	0.05	0.06	0.02	0.01	0.07	0.06
MgO	7.91	5.39	6.02	4.88	6.5	5.07	5.46	5.57	5.38	5.78	5.51	4.87	5.47
CaO	10.27	11.85	4.38	5.27	4.38	5.36	10.52	10.68	6.93	7.65	6.41	2.09	6
Na_2O	3.07	0.47	5.49	7.79	5.86	6.45	4.85	2.62	5.98	4.72	5.39	6.79	4.85
K_2O	1.15	3.27	1.4	0.16	1.24	2.01	1.36	1.17	0.46	1.53	1.06	3.11	1.8
P_2O_5	0.33	n.d.	0.37	0.41	0.48	0.37	0.58	0.45	n.d.	0.23	0.52	0.68	0.46
T(°C)	1212	1108	1242	1213	1259	1219	1154	1123	1194	1190	1199	1283	1197

Table 12: Continued list of surface melt inclusions and their host olivine, adjusted for FeO loss. T=Crystallization temperature, method explained in text. *Host olivine composition not measured by EMPA.

Sample	00Syr2												
Grain #	21	41	50	62	68	72	75	76	102	104	109	128	134
Host Olivine													
SiO_2	37.61	37.73	38.26	38.38	38.22	38.33	38.44	38.36	38.30	38.61	38.08	39.19	38.54
Cr_2O_3	0.01	n.d.	0.03	n.d.	0.02	0.03	0.01	0.03	0.03	0.01	n.d.	0.04	0.02
FeO	23.72	21.46	19.03	20.10	21.48	20.68	20.15	20.57	20.46	20.86	21.57	17.98	20.17
MnO	0.35	0.28	0.26	0.25	0.32	0.33	0.22	0.27	0.25	0.32	0.32	0.26	0.23
MgO	37.08	38.92	40.14	39.74	39.11	39.54	40.03	39.87	39.39	38.98	39.23	42.21	40.17
CaO	0.38	0.34	0.26	0.31	0.30	0.30	0.27	0.26	0.30	0.30	0.34	0.26	0.29
NiO	0.07	0.10	0.15	0.10	0.15	0.11	0.13	0.10	0.11	0.15	0.13	0.17	0.09
Fo	73.59	76.37	79.00	77.90	76.45	77.31	77.98	77.56	77.43	76.91	76.42	80.71	78.02
Mineral Volumes													
Plag (V%)					60	60	80			19	28		
Alk-Fsp (V%)			59	80	25					73	72	80		38
Cpx (V%)	10	50				40		30	9				29
Misc. (V%)	90	50	41	20	15		20	70			20	100	33
Inclusion composition													
SiO_2	52.45	43.59	54.93	49.42	51.73	50.77	51.14	47.36	48.07	50.09	47.40	42.78	48.49
TiO_2	2.68	2.15	2.26	0.43	0.56	1.98	1.23	0.80	0.38	0.38	1.38	2.72	1.78
Al_2O_3	21.32	16.13	20.91	23.44	23.15	18.31	17.22	14.45	20.07	22.99	22.91	17.66	17.47
FeO	5.28	10.75	5.27	7.71	4.75	6.50	6.23	13.29	3.54	3.67	4.56	7.00	10.91
MnO	0.05	0.22	0.24	0.06	0.09	0.06	0.13	0.15	0.08	0.11	0.13	0.07	0.12
MgO	6.10	11.45	8.97	7.30	6.91	8.05	10.45	14.02	4.60	5.02	6.42	12.78	9.14
CaO	9.83	13.73	9.54	3.14	6.25	7.89	4.28	5.58	4.40	4.41	3.41	15.07	7.12
Na2O	6.54	0.29	5.81	6.48	5.58	4.35	7.04	3.91	6.46	6.69	7.80	0.31	3.40
K_2O	0.28	1.48	1.45	1.63	1.80	1.68	1.92	1.16	2.26	2.01	3.03	1.88	1.53
P_2O_5	1.12	0.72	0.45	0.65	0.11	0.32	0.38	0.26	0.62	0.34	0.12	0.17	0.50
Total	105.64	100.51	109.84	100.28	100.93	99.91	100.02	100.97	90.48	95.71	97.15	100.46	100.46
Re-Equillibrated													
SiO_2	47.65	43.52	48.02	48.25	49.08	49.41	50.23	49.06	50.14	49.49	46.91	41.74	48.53
TiO_2	2.31	2.43	1.89	0.42	0.51	1.9	1.25	1.02	0.36	0.35	1.31	2.86	1.88
Al_2O_3	18.38	18.22	17.53	22.67	20.93	17.55	17.52	18.43	19.22	20.94	21.82	18.57	18.44
Fe_2O_3	1.6	1.59	1.61	1.61	1.6	1.6	1.6	1.6	1.6	1.6	1.61	1.6	1.6
FeO	10.08	10.02	10.12	10.13	10.08	10.08	10.11	10.07	10.09	10.1	10.13	10.08	10.08
MnO	0.04	0.25	0.2	0.06	0.08	0.06	0.13	0.19	0.08	0.1	0.12	0.07	0.13
MgO	4.62	5.65	6.17	5.37	5.3	5.76	5.3	5.71	5.35	5.18	4.41	6.75	6.1
CaO	8.47	15.51	8	3.04	5.65	7.56	4.35	7.12	4.21	4.02	3.25	15.85	7.51
Na2O	5.64	0.33	4.87	6.27	5.05	4.17	7.16	4.99	6.19	6.09	7.43	0.33	3.59
K_2O	0.24	1.67	1.22	1.58	1.63	1.61	1.95	1.48	2.16	1.83	2.89	1.98	1.61
P_2O_5	0.97	0.81	0.38	0.63	0.1	0.31	0.39	0.33	0.59	0.31	0.11	0.18	0.53
T(°C)	1135	1086	1197	1251	1197	1183	1250	1193	1241	1232	1244	1131	1184

Table 13: Continued list of surface melt inclusions and their host olivine, adjusted for FeO loss. T=Crystallization temperature, method explained in text. *Host olivine composition not measured by EMPA.

| Sample	00Syr2										00Syr4		
Grain #	135	151	165	181	208	213	254	265	271	278	137	181	249
Host Olivine													
SiO$_2$	38.06	38.57	38.49	38.41	38.52	38.17	38.44	37.89	37.93	38.58	38.63	38.45	39.12
Cr$_2$O$_3$	n.d.	0.03	0.02	0.01	n.d.	n.d.	0.03	0.01	0.03	n.d.	0.02	n.d.	0.03
FeO	20.91	18.70	20.49	19.34	19.07	21.42	18.20	21.11	22.05	20.84	18.50	19.67	13.95
MnO	0.29	0.23	0.29	0.23	0.25	0.31	0.21	0.29	0.35	0.27	0.17	0.25	0.17
MgO	39.90	41.56	39.82	41.20	41.27	39.28	41.69	39.45	39.57	39.79	41.96	40.91	45.69
CaO	0.31	0.27	0.28	0.27	0.29	0.33	0.26	0.30	0.37	0.34	0.21	0.17	0.19
NiO	0.17	0.15	0.12	0.18	0.17	0.12	0.15	0.09	0.11	0.20	0.07	0.17	0.30
Fo	77.28	79.85	77.60	79.15	79.42	76.57	80.33	76.91	76.18	77.29	80.17	78.76	85.38
Mineral Volumes													
Plag (V%)		18	37				12		36				
Alk-Fsp (V%)				30	54	63	76	91	61			61	87
Cpx (V%)				43	46	13	12						
Misc. (V%)	100	82	63	11		24		9	3		100	39	13
Inclusion composition													
SiO$_2$	47.44	42.04	52.43	49.43	50.93	56.00	57.58	60.02	52.00	56.83	44.14	40.27	48.68
TiO$_2$	2.16	3.52	0.08	1.96	1.73	1.92	0.77	0.83	1.35	0.36	3.26	3.78	3.04
Al$_2$O$_3$	18.50	15.86	21.67	19.01	18.05	20.40	22.67	22.74	28.45	23.41	21.12	19.31	23.21
FeO	7.51	6.37	6.87	2.84	3.72	1.22	1.72	1.29	1.59	1.45	14.56	11.13	4.47
MnO	0.17	0.12	0.21	0.07	0.08	0.03	0.06	0.08	0.02	0.09	0.25	0.17	0.12
MgO	10.59	13.00	9.90	5.80	7.41	0.91	1.32	0.23	0.27	0.24	4.42	6.05	2.42
CaO	7.70	17.64	4.37	11.03	10.95	7.52	5.01	2.11	6.32	2.69	7.80	10.31	8.74
Na$_2$O	4.66	0.55	4.74	4.04	4.95	7.41	7.02	8.11	7.14	8.72	2.78	3.85	5.51
K$_2$O	1.34	1.11	1.20	1.00	1.21	2.56	2.43	3.34	2.23	4.00	1.92	1.39	2.50
P$_2$O$_5$	0.35	0.20	0.59	0.30	0.47	0.71	0.34	0.06	0.15	0.88	0.71	0.34	0.01
Total	100.41	100.41	102.07	95.48	99.50	98.69	98.90	98.80	99.51	98.67	100.96	96.60	98.72
Re-Equillibrated													
SiO$_2$	46.66	40.85	50.33	48.6	48.57	51.45	52.39	54.37	48.05	52.09	44.2	41.64	46.13
TiO$_2$	2.24	3.73	0.08	1.73	1.53	1.5	0.59	0.64	1.04	0.28	3.23	3.97	2.33
Al$_2$O$_3$	19.18	16.81	21.09	16.82	16.01	15.89	17.26	17.52	21.99	18.17	20.93	20.3	17.82
Fe$_2$O$_3$	1.6	1.6	1.61	1.6	1.61	1.6	1.61	1.61	1.6	1.6	1.6	1.6	1.6
FeO	10.1	10.07	10.12	10.11	10.12	10.08	10.12	10.17	10.07	10.11	10.07	10.06	10.09
MnO	0.18	0.13	0.2	0.06	0.07	0.02	0.05	0.06	0.02	0.07	0.25	0.18	0.09
MgO	5.47	6.13	5.96	6.58	6.49	5.29	6.73	5.12	4.99	5.03	6.63	5.55	9.06
CaO	7.98	18.7	4.25	9.76	9.71	5.86	3.81	1.63	4.88	2.09	7.73	10.84	6.71
Na2O	4.83	0.58	4.61	3.58	4.39	5.77	5.34	6.25	5.52	6.77	2.76	4.05	4.23
K2O	1.39	1.18	1.17	0.89	1.07	1.99	1.85	2.57	1.72	3.11	1.9	1.46	1.92
P$_2$O$_5$	0.36	0.21	0.57	0.27	0.42	0.55	0.26	n.d.	0.12	0.68	0.7	0.36	n.d.
T(°C)	1172	1104	1223	1179	1189	1213	1278	1295	1203	1289	1185	1144	1291
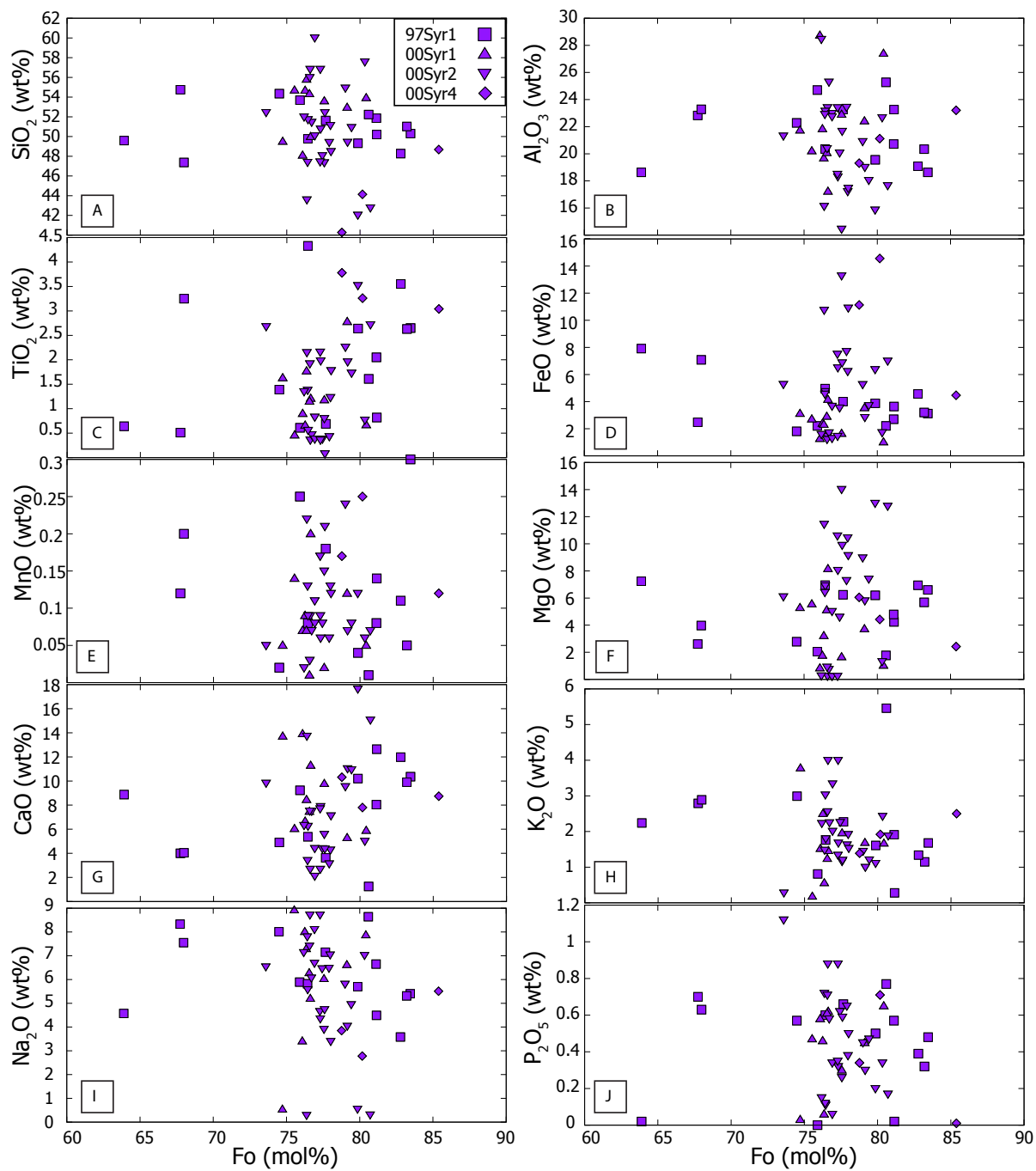
Figure 23: Unequilibrated surface melt inclusion major element data based on volume% calculation relative to host forsterite content.
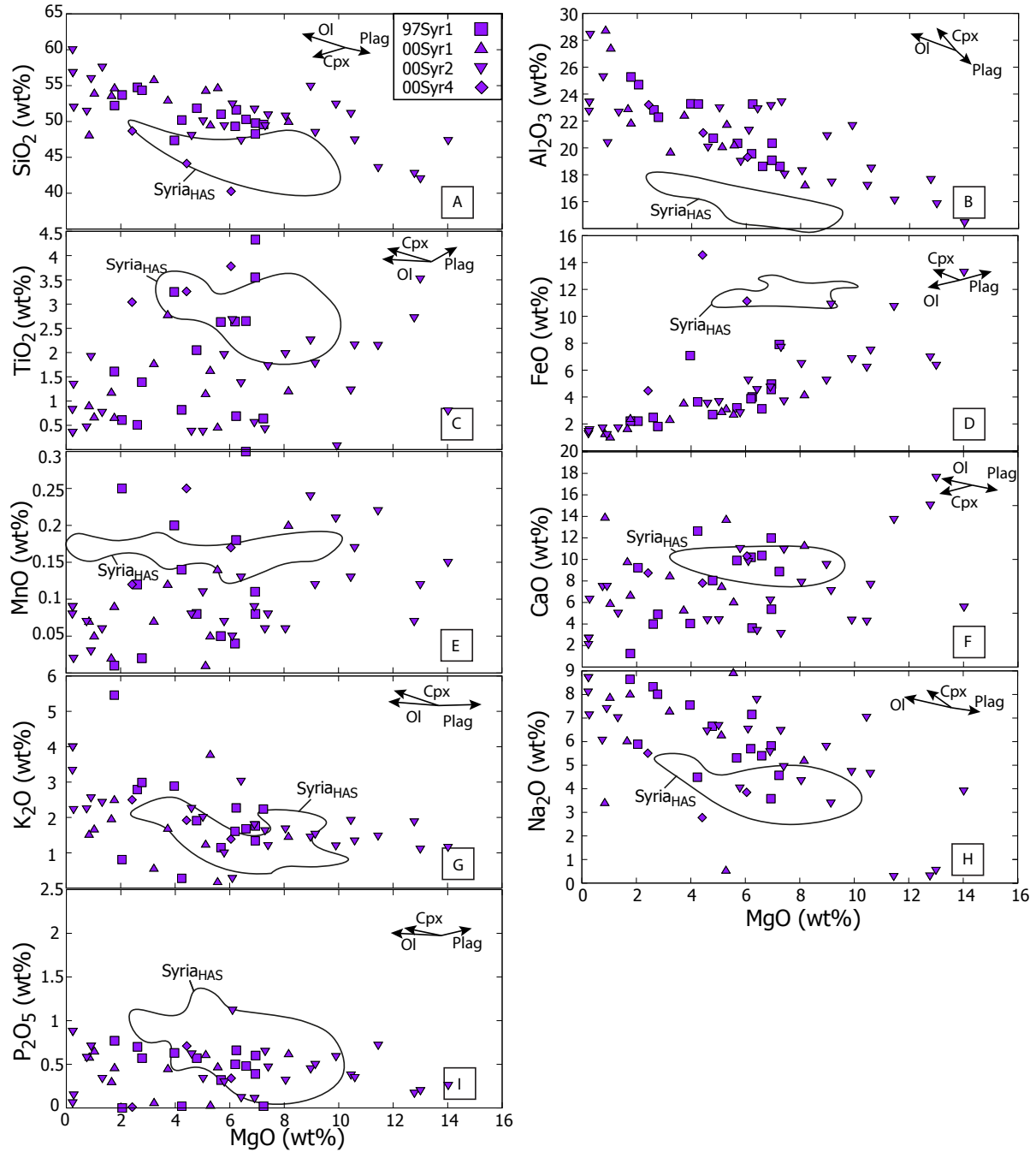
Figure 24: Unequilibrated surface melt inclusion major element data based on volume% calculation relative to MgO. Representative overlay and data thereof is as in Figure 14,16.
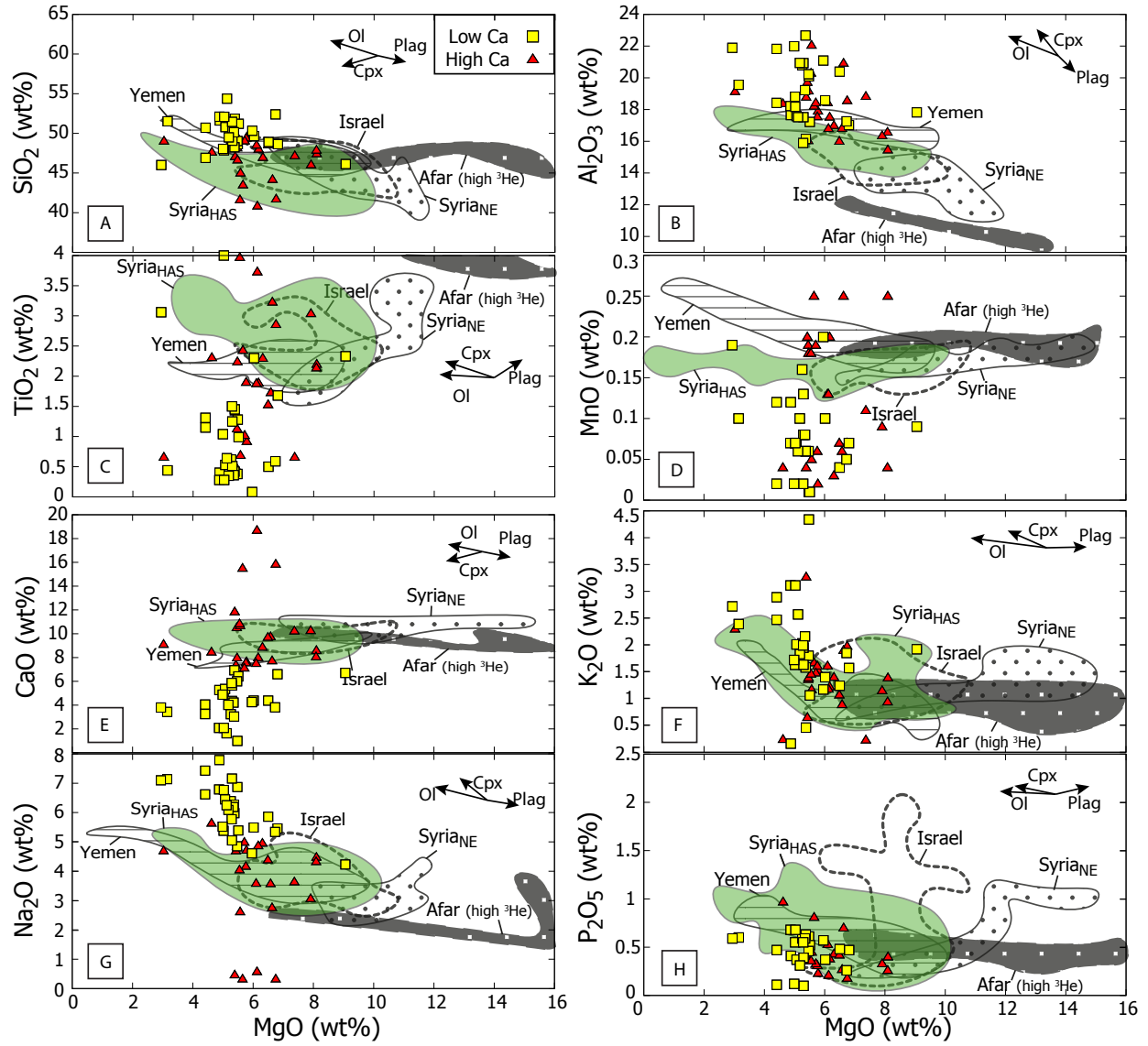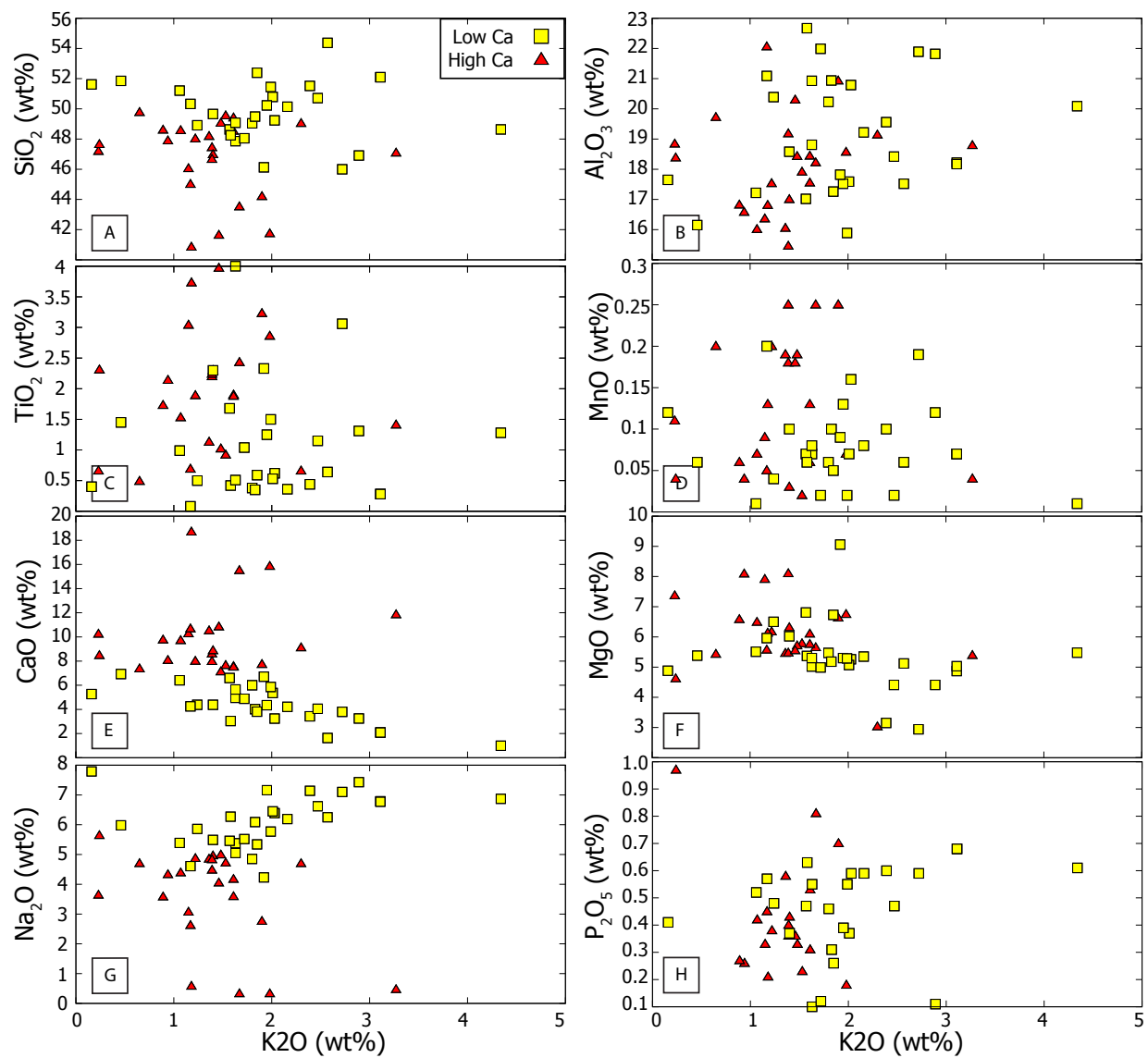
39

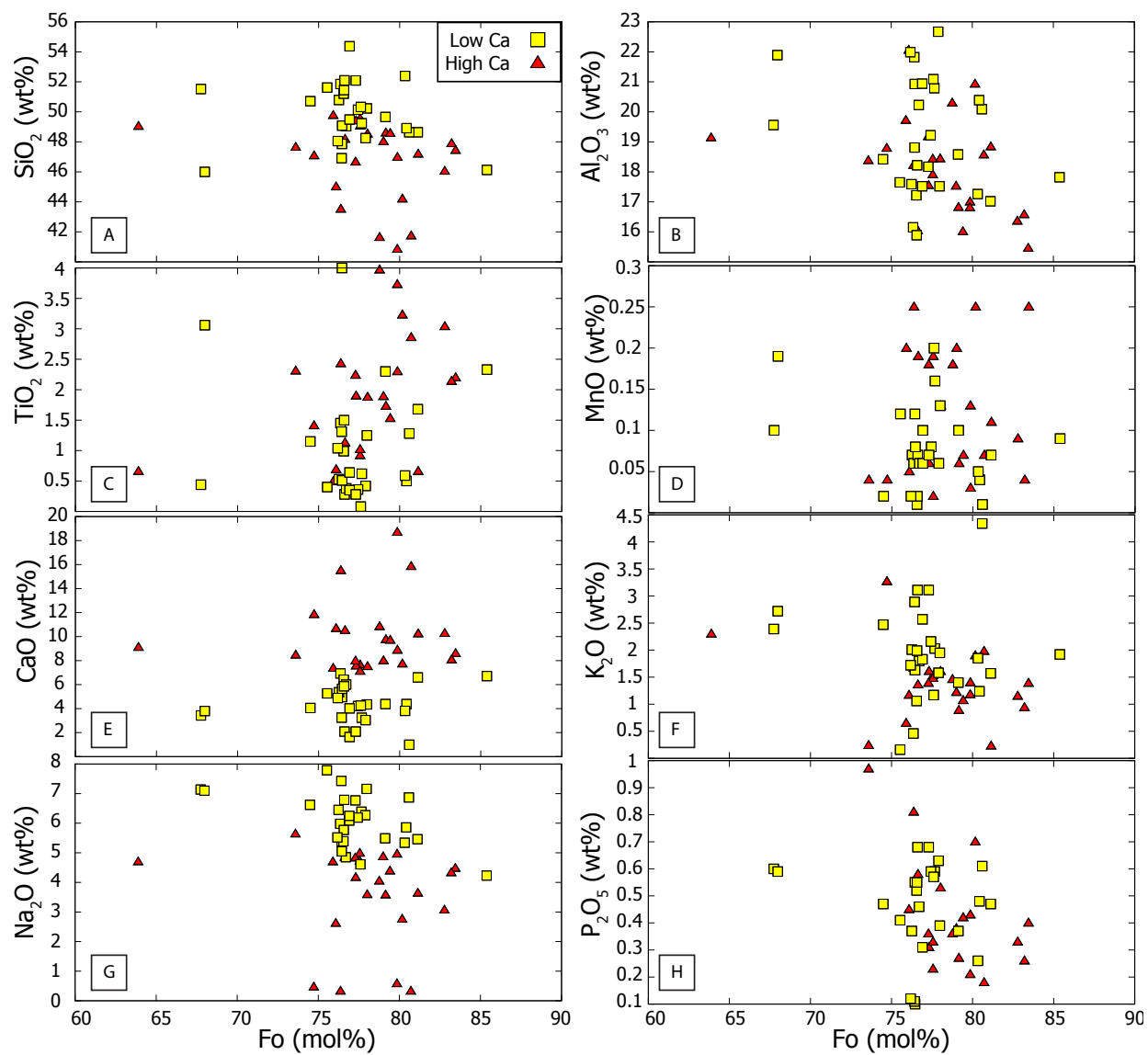Figure 25: Re-equillibrated surface melt inclusion major element data relative to MgO. Re-equilibration procedure discussed in text. Representative overlays and data thereof are as in Figure 14,15.

Figure 26: Re-equillibrated surface melt inclusions major element data relative K_2O. Re-equilibration procedure discussed in text.

41

Figure 27: Re-equilibrated major element versus host Fo diagrams for surface melt inclusions. Re-equilibration procedure discussed in text.
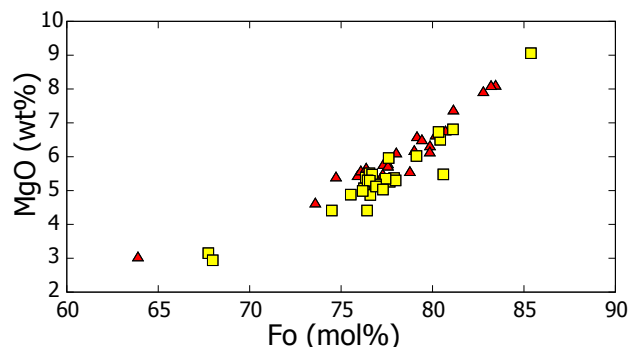
Figure 28: Re-equilibrated surface melt inclusion MgO wt% versus host olivine Fo.

However, assuming the collection of melt inclusions from olivine with >75 Fo has not been subject to crystallization of phases other than olivine before entrapment, and an initial melt composition in equilibrium with the mantle array, primary magma compositions can be estimated by reverse-fractionating olivine up to sufficiently high forsterite contents. For this procedure I estimated mantle equilibrated olivine compositions to range from Fo_{89} to Fo_{90}, based on the inferred intersection between the compositional range of my spinel inclusions and the mantle array (Figure 19). Calculations were performed using the same Ol-MI equilibrium model and Fe^{2+}/Fe^{3+} ratio as used in the initial melt inclusion re-equilibration, as described in section 6.3.2. The resulting primary magma compositions indicate an estimated temperature range of 1360-1400 ± 10 °C.

6.3.5 Trace elements and melt diversity

Out of the complete set of 67 melt inclusions, a total of 22 measurements were deemed unrepresentative of melt and discarded (e.g. Dy/Yb, La/Sm ratios of ¡1, unmeasured elements, or measured element concentrations of >100 rela-
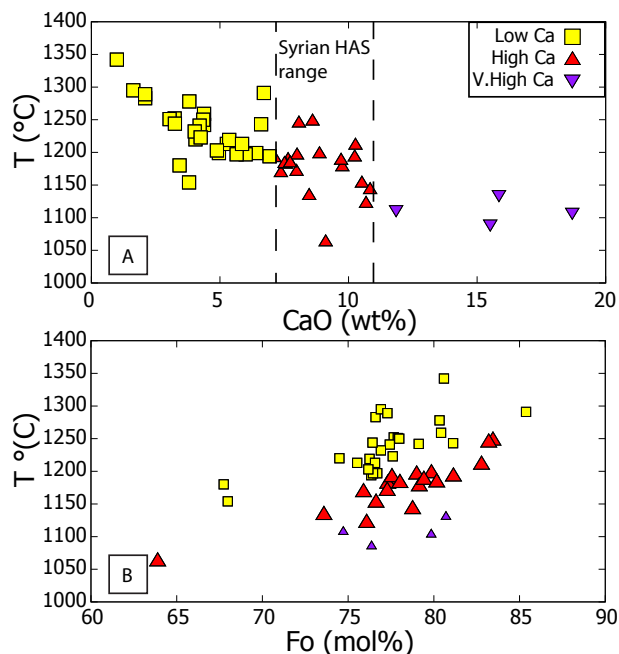

Figure 29: Crystallization/entrapment temperature in Celsius calculated by PETROLOG3 versus CaO content. The Syrian HAS field is based on whole-rock data from *Krienitz et al.* (2007). Temperature calculations from low and very high calcium samples are deemed not viable. Method explained in text.

tive to primitive mantle). It is likely these measurements ablated phases other than the melt inclusion, such as plagioclase or spinel, contaminating the signal. Out of the remaining 45 measurements, 8 were derived from sample 97Syr1, 12 from sample 00Syr1, 20 from sample 00Syr2, and 5 from sample 00Syr4 (Table 14-17). A complete list of measured inclusions is included in the Electronic Appendix. I was able to identify three distinct chemical groups of melt inclusions, based primarily on degree of enrichment (Figure 30), simply named group 1, 2, and 3. The vast majority of inclusions is part of group 1 (37 inclusions), which is chemically similar to alkali basalt whole-rock data from this area
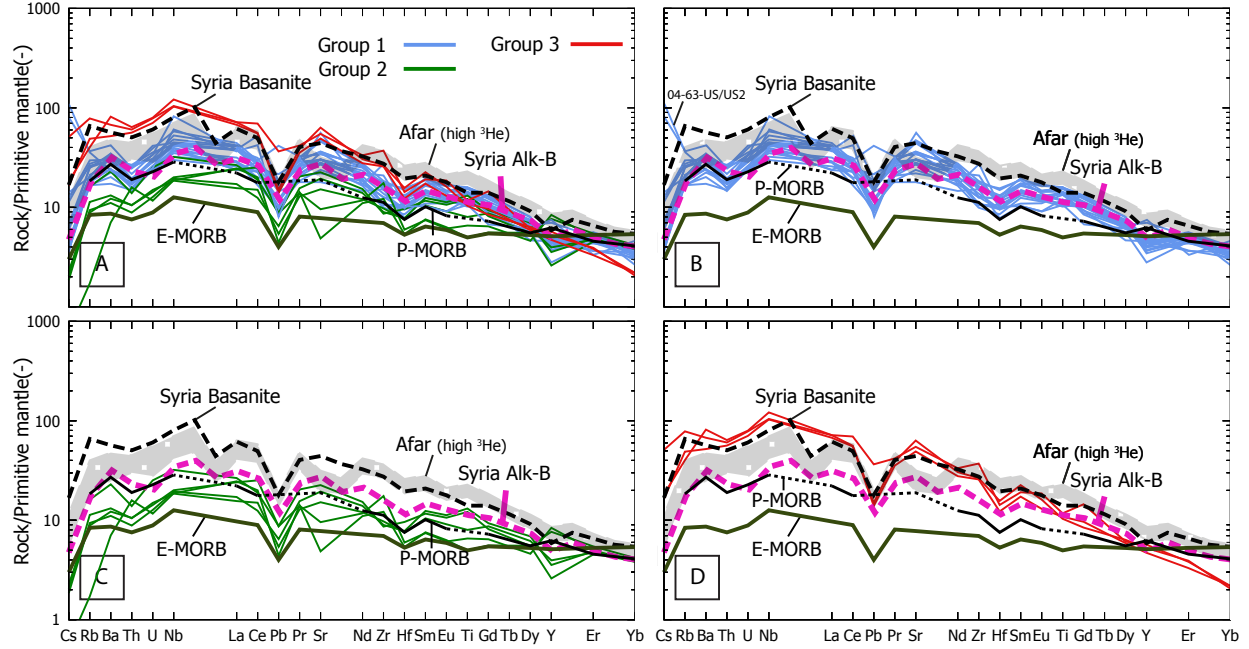
Figure 30: Primitive mantle normalised trace element diagrams in order of low to high incompatibility for melt inclusion groups 1,2, and 3 as measured by LA-ICPMS. Absolute concentrations were normalized to 10 wt% CaO; see methods. Representative lines and normalization values as in Figure 16. Select measurements were removed from group 1 to decrease clutter. Compositions are listed in Table 14-17 and the Electronic Appendix.

(Figure 30) [*Krienitz et al.*, 2007]. This group includes the majority of inclusions from samples 97Syr1 (6), 00Syr1 (12), and 00Syr2 (17), and also includes two measurements from 00Syr4 (Table 14-17). Groups 2 and 3 represent two enrichment extremes, with group 2 representing depleted compositions, and group 3 representing the most enriched samples (Figure 30). The former group includes five inclusions, the while the latter includes only three. Group 2 includes two measurements from 97Syr1 and three from 00Syr2, and group 3 is made up of three of the 00Syr4 measurements. Both melt inclusions in olivine number 64 (High Cs lines in Figure 30B; Table 17) present a slightly anomalous, selectively enriched signal compared the

rest of group 1. Nevertheless, their chemical dissimilarity and overall depletion with respect to the other inclusions from 00Syr4 classify them within the third group. Similar to whole-rock analysis, melt inclusions from all groups contain elevated concentrations of Ba, Nb, Sm, Sr, and Ti. A total of four measurements from group 1 also contain positive Pb anomalies. Negative anomalies are most frequently observed in elements Th, Pb, Hf, and Y, with few exceptions in group 2. Europium anomalies increase from slightly negative to slightly positive from group 2 (Eu/Eu*=0.988) to 3 (Eu/Eu*=1.099), while group 1 presents an intermediate value close to the average of the full data set (Eu/Eu*=1.040). LREE/HREE (e.g. La/Yb) and MREE/HREE

44

(e.g. Dy/Yb) ratios stretch from averages of 7.94 and 2.22 in group 2, to 48.35 and 4.38 group 3, respectively, increasing in accordance with degrees of enrichment (Figure 31). This trend largely agrees with whole-rock data derived from Ethiopian flood basalts associated with the Afar (Figure 31) [*Pik et al.*, 1999]. In contrast, Yemeni flood basalts, also associated with activity of the Afar plume, include significantly lower MREE/HREE ratios despite similar LREE/HREE ratios (Figure 31) [*Baker et al.*, 1997]. Th/Yb versus Nb/Yb ratios indicate no selective thorium enrichment, consistent with a lack contamination by continental material from either lithospheric interaction or melting of subducted sediments (Figure 32). In agreement with this, none of my melt inclusions include significant co-variation of crustal contamination sensitive Ce/Pb or Nb/U ratios (Figure 33). Nevertheless, few measurements posses Ce/Pb ratios diverging from the main cluster. This is primar-
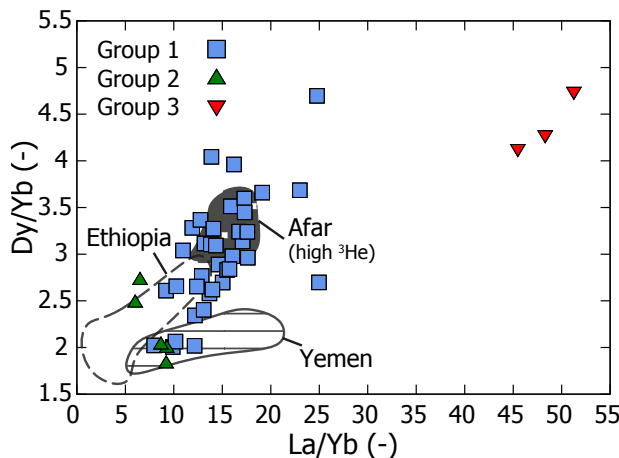

Figure 31: Dy/Yb versus La/Yb ratios of the three melt inclusion groups. Yemeni and Ethiopian overlays based on *Baker et al.* (1997) and *Pik et al.*, 1999. Afar (high ^{3}He) field includes only high ^{3}He lavas associated with the Afar plume from *Pik et al.*, 1999.

ily driven by selective lead enrichments independent of cerium concentrations, as was also observed in the whole-rock data (Table 14-17). Additionally, the two inclusions from olivine 64 of 00Syr4 include extreme Nb/U ratios of approximately 80, providing a unique signal unrelated to their Ce/Pb content. Relative placement on the MORB-OIB array in Th-Yb vs Nb/Yb space indicates the main group of inclusions (group 1) to be virtually identical to the complete collection of Syrian Harrat al-Shamah whole-rock samples of *Krienitz et al.* (2007) (Figure 32). This group is within close chemical agreement with the representative OIB composition of *Sun & Mcdonough* (1989) and the high ^{3}He lavas derived from the Afar plume, albeit slightly more depleted. Group 2 inclusions present noticeably more depleted compositions in Th/Yb-Nb/Yb space (Figure 32), which is in agreement with the relative enrichments observed in spider diagrams (Figure 30). Four out of five measurements of this group are of similar enrichment as the most depleted rocks from Yemen, as well as Iranian P-MORB rocks, when projected onto the MORB-OIB array. This positions this group of inclusions in between OIB and E-MORB compositions. Conversely, the three group 3 samples inside olivine grains 137 and 265 have Th/Yb and Nb/Yb ratios of essentially ten times higher than those in group 2. These samples represent a different end-member with degrees of enrichment in agreement with the most enriched basanites from Israel [*Weinstein et al.*, 2006]. Out of the 'High Ca' group of surface inclusions, a total of seven inclusions have matching LA-ICPMS data (Figure 34). Aside from five group 1 inclusions, the collection includes melt inclusion samples 97-158 and 04-137, from groups 2 and 3, respectively. Approximate trends can be determined based on major oxide concentrations relative to
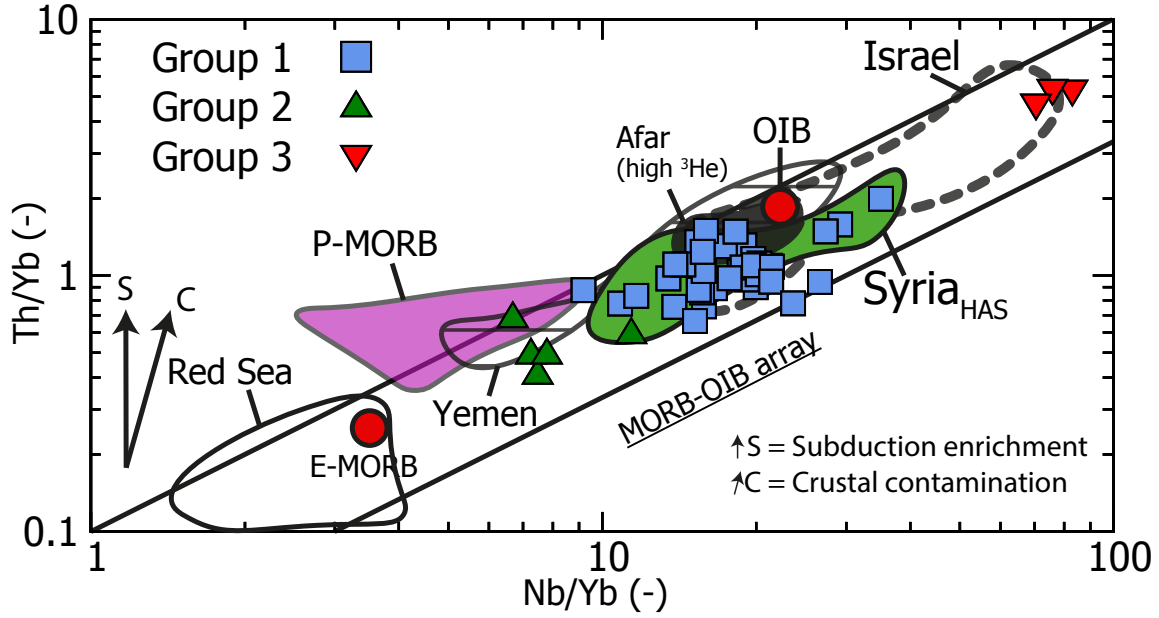
Figure 32: Th/Yb versus Nb/Yb of melt inclusion groups 1, 2, and 3. MORB-OIB array is from *Pearce and Peate* (1995). Representative compositions of E-MORB and OIB are from *Sun & Mcdonough* (1989). P-MORB compositional field is from Saccani et al. (2013a). Subduction and crustal contamination trajectories are included.

PM normalised La/Sm ratios (Figure 34). The remaining data shows some degree of scatter, but approximate trends can be identified to stretch between the group 1 and 3 samples for select oxides. Most noticeably, SiO_2 appears to decrease towards group 3, while Al_2O_3, K_2O, and P_2O_5 can be observed to increase from group 2 to 3 (Figure 34). While the sample 2 and 3 samples define significantly distinct end-members with regards to the remaining oxides, the lack of a progressive trend observed in group 1 samples does not allow us to confidently attribute these values to mantle end-members.
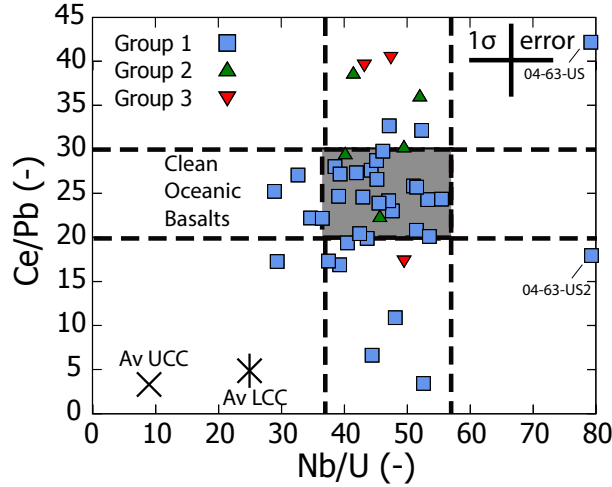
Figure 33: Crustal contamination sensitive Ce/Pb versus Nb/U ratios of all melt inclusion measurements. Reference compositions as in Figure 17. The 1σ error is the mean error based on propagating GLITTER calculated 1σ errors.
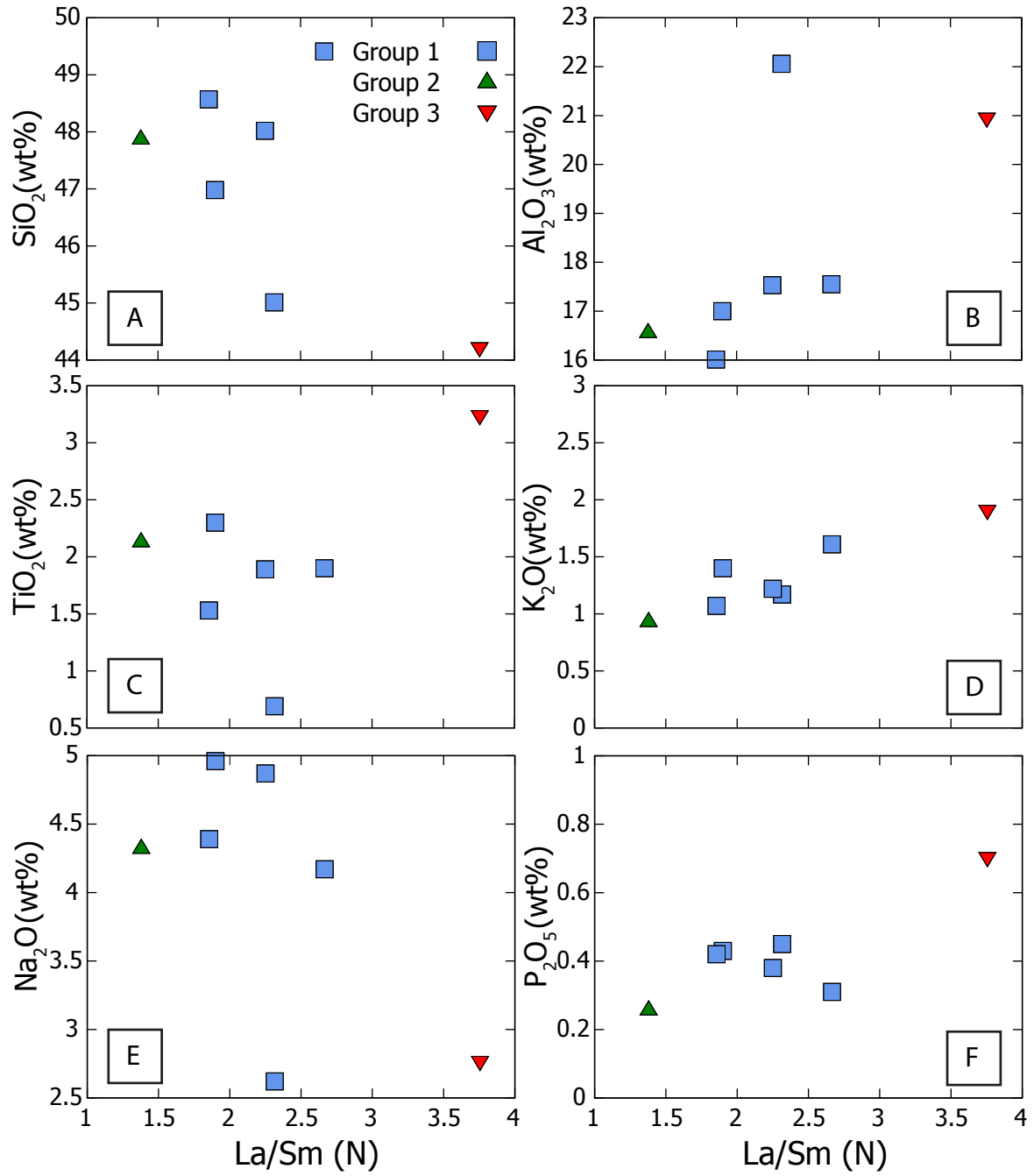
Figure 34: Selected major oxide concentrations of surface inclusions versus primitive mantle normalised La/Sm ratios. All plotted values are from the 'High Ca' group as defined in Figure 27-29. Normalization values are from *Mcdonough & Sun* (1995).

Table 14: List of LA-ICPMS measurements of melt inclusions considered viable for interpretation. Host olivine data is based on EMPA. Trace element concentrations are listed in ppm, as normalized to a CaO concentration of 10 wt%. Inclusion # coding follows: host WR-Olivine #- (if applicable) under surface (US).* Composition of inclusion 97-3-US is mean of three analyses.

Sample	97Syr1								00Syr1		
Host Olivine											
Grain #	3	41	119	158	167	179	182	190	65	68	95
SiO_2	39.29	38.86	38.75	39.12	39.09	38.84	38.45	38.71	37.91	38.55	38.00
Cr_2O_3	n.d.	n.d.	0.02	0.09	0.06	0.04	n.d.	0.02	n.d.	0.07	0.03
FeO	15.83	18.03	17.50	15.77	15.78	17.64	19.49	18.67	19.25	19.94	22.37
MnO	0.12	0.21	0.21	0.19	0.17	0.21	0.19	0.26	0.29	0.19	0.32
MgO	44.55	42.52	42.42	43.84	44.09	42.50	41.36	41.53	40.92	40.72	38.54
CaO	0.21	0.23	0.25	0.24	0.24	0.23	0.24	0.24	0.26	0.27	0.28
NiO	0.26	0.20	0.19	0.21	0.21	0.22	n.d.	0.14	0.20	n.d.	0.11
Fo	83.38	80.78	81.20	83.20	83.27	81.12	79.09	79.86	79.12	78.45	75.43
MI											
Inclusion #	97-3-US*	97-41-US	97-119	97-158	97-167-US	97-179	97-182-US	97-190	01_65	01-68-US	01-95-US
Group	2	1	1	2	1	1	1	1	1	1	1
Trace el.											
Ti	10153	12416	11439	11243	9630	12848	12956	14540	14321	33378	14288
V	262	183	185	155	281	166	158	701	94	313	93
Cr	3497	1130	639	645	6541	814	687	47218	392	1746	213
Rb	7.2	10.0	4.2	4.0	7.9	8.8	10.2	8.6	12.3	8.4	8.3
Sr	318	480	401	274	300	425	486	459	542	462	688
Y	17	19	25	15	16	17	16	16	19	50	19
Zr	102	134	106	94	110	114	115	104	170	461	168
Nb	13	20	21	9	15	17	21	22	22	63	22
Cs	0.04	0.10	b.d.l.	0.03	0.08	0.07	0.06	0.07	0.24	0.36	0.09
Ba	92	150	70	52	109	121	145	114	159	100	159
La	11	17	18	8	13	14	15	13	18	54	20
Ce	25	38	37	21	28	33	38	38	46	134	46
Pr	3.4	4.8	4.9	2.8	3.6	4.2	4.4	4.5	5.6	15.3	6.0
Nd	16	22	21	12	16	18	19	18	24	60	25
Sm	4	5	5	4	4	4	4	4	5	14	5
Eu	1.5	1.8	1.7	1.2	1.4	1.5	1.4	1.5	1.9	3.2	2.0
Gd	5	6	5	4	4	4	4	4	5	13	5
Dy	4	5	5	3	3	4	4	4	4	10	4
Er	2.2	2.3	2.6	1.5	1.5	1.7	1.6	1.8	1.7	4.0	1.6
Yb	1.8	1.8	2.3	1.2	1.3	1.3	1.1	1.1	1.2	2.2	1.2
Lu	0.26	0.25	0.32	0.17	0.17	0.19	0.20	0.21	0.18	0.39	0.19
Hf	3.0	3.7	2.5	2.1	2.8	2.9	2.9	2.8	3.8	10.0	3.4
Ta	0.9	1.3	1.0	0.5	0.8	1.0	1.0	1.0	1.1	3.3	1.4
Pb	1	2	6	1	1	1	1	1	2	7	2
Th	0.9	1.4	2.0	0.5	1.0	1.0	1.2	1.0	1.5	3.4	1.1
U	0.3	0.5	0.2	0.2	0.3	0.4	0.5	0.4	0.6	0.6	0.4

Table 15: Table 14 continued

Sample	**00Syr1**									**00Syr2**	
Host Olivine											
Grain #	102	117	132	135	149	150	175	182	226	7	17
SiO$_2$	38.27	38.21	38.20	38.56	37.61	38.12	37.59	37.59	38.10	38.13	38.26
Cr$_2$O$_3$	0.03	n.d.	0.01	n.d.	0.01	n.d.	0.03	0.02	n.d.	n.d.	n.d.
FeO	17.94	17.33	17.99	20.21	23.69	21.58	21.72	21.48	21.41	21.29	21.26
MnO	0.25	0.22	0.22	0.31	0.35	0.29	0.33	0.27	0.27	0.28	0.27
MgO	41.80	42.09	41.45	40.49	37.50	38.87	38.76	38.90	39.20	39.11	39.28
CaO	0.28	0.29	0.27	0.26	0.42	0.32	0.35	0.32	0.32	0.34	0.31
NiO	0.10	0.14	0.17	0.04	0.09	0.11	0.09	0.13	0.13	0.09	0.13
Fo	80.59	81.24	80.42	78.12	73.83	76.25	76.08	76.35	76.55	76.60	76.70
MI											
Inclusion #	01-102-US	01-117-US	01-132	01-135-US	01-149-US	01-150	01-175	01-182	01-226-US	02_7	02-17-US
Group	1	1	1	1	1	1	1	1	1	1	1
Trace el.											
Ti	13600	10517	13042	13376	21477	13846	15398	12362	14490	12953	14184
V	235	116	173	110	259	127	227	135	88	151	135
Cr	9393	1645	799	522	361	115	1279	681	199	875	373
Rb	3.2	13.3	24.6	8.9	15.2	10.9	10.6	6.9	12.4	9.5	9.1
Sr	620	446	552	579	582	495	379	631	1735	418	534
Y	26	17	19	20	42	20	20	18	29	18	19
Zr	173	182	186	144	332	193	160	156	255	139	172
Nb	22	21	44	20	40	28	26	23	29	22	24
Cs	b.d.l.	0.26	0.42	0.14	0.20	0.14	0.13	0.08	0.20	0.10	0.13
Ba	41	149	134	133	228	167	121	148	168	143	160
La	21	18	31	17	38	21	16	18	28	16	20
Ce	47	41	85	40	87	50	48	45	63	45	48
Pr	5.8	5.5	8.9	4.9	10.0	6.0	4.8	5.4	7.4	4.9	5.7
Nd	25	23	32	21	40	25	19	23	31	20	24
Sm	6	6	5	5	9	6	4	5	7	4	5
Eu	2.1	1.6	1.7	1.7	2.7	1.9	1.5	1.5	2.3	1.4	1.7
Gd	5	5	5	5	9	5	5	4	7	4	4
Dy	5	3	3	4	8	4	3	3	6	3	3
Er	2.3	1.4	1.7	1.7	3.8	1.8	1.7	1.6	2.5	1.6	1.8
Yb	1.6	1.2	1.3	1.2	2.6	1.3	1.7	1.2	1.6	1.3	0.9
Lu	0.21	0.18	0.22	0.20	0.38	0.18	0.26	0.16	0.26	0.25	0.18
Hf	3.8	4.4	3.0	3.1	6.3	4.2	3.2	3.3	5.4	2.6	3.4
Ta	1.2	1.1	1.9	1.1	2.1	1.4	1.0	1.3	1.4	1.0	1.2
Pb	2	2	4	2	4	5	2	2	2	7	2
Th	1.6	1.6	2.5	1.1	3.5	1.4	1.3	1.4	2.4	1.2	1.3
U	0.6	0.5	1.2	0.4	0.8	0.6	0.5	0.4	0.7	0.5	0.5

49

Table 16: Table 14 continued

Sample	**00Syr2**										
Host Olivine											
Grain #	19	19	21	50	68	72	102	102	112	128	130
SiO$_2$	37.90	37.90	37.61	38.26	38.22	38.33	38.30	38.30	38.33	39.19	38.44
Cr$_2$O$_3$	n.d.	n.d.	0.01	0.03	0.02	0.03	0.03	0.03	n.d.	0.04	n.d.
FeO	22.58	22.58	23.72	19.03	21.48	20.68	20.46	20.46	21.16	17.98	21.02
MnO	0.29	0.29	0.35	0.26	0.32	0.33	0.25	0.25	0.30	0.26	0.28
MgO	39.00	39.00	37.08	40.14	39.11	39.54	39.39	39.39	39.94	42.21	40.00
CaO	0.39	0.39	0.38	0.26	0.30	0.30	0.30	0.30	0.29	0.26	0.27
NiO	0.11	0.11	0.07	0.15	0.15	0.11	0.11	0.11	n.d.	0.17	n.d.
Fo	75.48	75.48	73.59	79.00	76.45	77.31	77.43	77.43	77.08	80.71	77.23
MI											
Inclusion #	02-19-US	02-19-US-B	02_21	02_50	02_68	02_72	02-102	02-102-US	02-112-US	02-128-US	02-130-US
Group	1	2	1	1	1	1	1	1	1	2	1
Trace el.											
Ti	12609	11489	12187	11916	10212	5990	11236	13164	12931	9140	13183
V	262	164	117	112	181	51	168	164	85	280	63
Cr	1342	3156	211	508	682	149	717	733	301	2886	255
Rb	11.0	7.7	11.4	7.7	9.4	1.6	9.3	8.8	8.7	6.1	18.8
Sr	435	277	518	546	360	214	413	476	524	280	659
Y	19	36	21	15	12	8	17	19	18	11	32
Zr	162	184	190	135	131	64	163	170	156	91	283
Nb	20	19	26	18	17	8	20	23	21	13	33
Cs	0.12	0.07	0.30	0.10	0.16	0.02	0.17	0.12	1.00	b.d.l.	0.29
Ba	142	117	215	137	117	30	147	138	140	95	193
La	18	23	23	15	11	8	18	17	18	11	33
Ce	41	42	53	40	33	16	46	42	40	32	79
Pr	5.1	5.2	6.2	4.5	3.7	2.0	5.5	4.9	5.2	3.2	10.5
Nd	21	21	26	18	14	8	23	21	22	12	46
Sm	5	4	5	4	3	2	4	5	5	3	12
Eu	1.6	1.4	1.8	1.4	1.1	0.7	1.6	1.5	1.8	1.0	3.3
Gd	5	5	5	4	3	2	4	4	5	3	10
Dy	4	5	4	3	2	1	3	3	3	2	8
Er	1.6	3.2	1.5	1.2	1.2	0.6	1.6	1.5	1.4	1.2	3.6
Yb	1.1	2.5	1.3	0.9	1.1	0.5	1.3	1.3	1.0	1.2	2.0
Lu	0.18	0.36	0.23	0.15	0.15	0.07	0.21	0.20	0.17	0.15	0.30
Hf	3.6	3.3	4.2	2.9	2.9	1.4	3.6	3.7	3.4	2.3	7.1
Ta	1.0	1.0	1.3	1.0	0.7	0.4	1.1	1.1	1.1	0.7	2.1
Pb	2	2	2	2	2	5	3	2	2	1	5
Th	1.1	1.2	1.5	0.9	0.7	0.4	1.2	1.3	1.1	0.7	3.1
U	0.4	0.4	0.6	0.4	0.3	0.1	0.5	0.4	0.4	0.3	1.1

Table 17: Table 14 continued

Sample	00Syr2							00Syr4				
Host Olivine												
Grain #	152	154	208	208	254	265	271	63	63	137	265	265
SiO_2	37.73	38.66	38.52	38.52	38.44	37.89	37.93	39.45	39.45	38.63	38.49	38.49
Cr_2O_3	0.01	0.05	n.d.	n.d.	0.03	0.01	0.03	0.03	0.03	0.02	0.01	0.01
FeO	21.81	20.42	19.07	19.07	18.20	21.11	22.05	14.72	14.72	18.50	17.24	17.24
MnO	0.28	0.24	0.25	0.25	0.21	0.29	0.35	0.16	0.16	0.17	0.22	0.22
MgO	38.76	40.39	41.27	41.27	41.69	39.45	39.57	45.02	45.02	41.96	43.15	43.15
CaO	0.29	0.28	0.29	0.29	0.26	0.30	0.37	0.17	0.17	0.21	0.21	0.21
NiO	0.14	0.15	0.17	0.17	0.15	0.09	0.11	0.32	0.32	0.07	0.20	0.20
Fo	76.01	77.90	79.42	79.42	80.33	76.91	76.18	84.50	84.50	80.17	81.69	81.69
MI												
Inclusion #	02-152-US2	02-154-US	02-208	02-208-S	02-254-2	02-265	02-271-S	04-63-US	04-63-US2	04-137	04-265-S	04-265-S2
Group	1	1	1	1	1	1	2	1	1	3	3	3
Trace el.												
Ti	13128	13998	14126	12754	13891	8142	8446	17544	22385	17333	13086	14261
V	93	59	245	184	124	133	107	255	348	187	239	304
Cr	336	283	1272	1330	183	642	161	315	746	88	313	717
Rb	8.1	10.3	9.3	11.6	12.3	14.7	1.5	29.7	38.7	29.5	49.3	32.0
Sr	589	928	453	500	430	506	137	842	1967	1333	1322	1067
Y	18	21	16	18	19	23	33	30	32	24	23	20
Zr	141	227	134	161	174	193	128	219	286	390	278	270
Nb	18	28	24	21	22	25	17	55	95	98	72	74
Cs	0.14	0.09	0.23	b.d.l.	0.28	0.28	0.02	3.20	2.98	0.38	1.07	0.35
Ba	90	204	143	142	176	202	65	215	487	660	468	374
La	16	25	15	18	20	26	22	33	43	57	49	48
Ce	38	57	55	44	48	77	33	71	88	117	94	92
Pr	4.8	7.4	5.9	5.9	5.9	7.7	5.1	9.2	11.5	13.0	10.4	9.8
Nd	21	32	23	25	25	33	19	38	37	51	40	38
Sm	5	9	5	6	6	7	4	8	7	10	10	8
Eu	2.0	2.8	1.9	1.8	1.9	2.6	1.4	2.7	2.5	3.5	2.6	2.2
Gd	5	8	5	6	5	7	4	8	6	10	5	6
Dy	5	5	4	4	5	6	5	6	7	5	5	4
Er	1.6	2.3	1.4	2.3	2.0	2.4	3.4	3.1	2.6	2.1	1.8	1.6
Yb	1.2	1.3	1.1	1.4	1.4	1.8	2.6	2.4	3.6	1.2	1.0	1.1
Lu	0.16	0.17	0.16	0.20	0.20	0.24	0.35	0.34	0.43	0.30	0.26	0.27
Hf	4.3	5.6	3.3	4.5	4.2	4.7	2.9	5.2	6.9	6.7	6.3	5.1
Ta	1.2	1.6	1.1	1.1	1.3	1.5	0.8	3.1	5.1	5.6	3.6	3.9
Pb	2	3	2	2	2	3	1	2	5	7	2	2
Th	1.2	1.4	1.1	1.6	1.7	2.0	1.8	1.9	3.5	6.2	5.1	4.9
U	0.4	0.7	0.6	0.5	0.7	0.9	0.3	0.7	1.2	2.0	1.7	1.6

7 Discussion

7.1 Melt end-members

The collection of melt inclusions that was analysed covers a range of compositions which cannot be explained by simple fractional crystallization. The restricted range of MgO concentrations in the melt inclusions, as well as the forsterite of their host crystals indicate that the individual inclusions were trapped at a similar interval in the fractionation process. Nevertheless, the presence of solitary plagioclase inclusions indicates the system to have progressed beyond single-phase crystallization of olivine, albeit to a limited degree (based on high Sr and Eu). Additional evaluation of crustal input on the basis of trace element systematics relative to an extensive set of clean ocean basalts [*Hofmann et al.*,1986; *Pearce & Peate*, 1995] has also indicated that my samples are representative of mostly uncontaminated compositions (Figure 32, 33). I therefore discern that the melt inclusion groupings are representative of incomplete mixing between two melt end-members relevant in the generation of Harrat al-Shamah volcanism. The presence of multiple compositionally variable inclusions within a single crystal confirm this. The end-members of groups 2 and 3 represent noticeably depleted and enriched melts, respectively. This variation can either be the result of melting within mantle domains of variable composition, and/or different conditions of melt generation from a similar source. Variable melting regimes are in agreement with previous literature from the area, which has consistently argued for multiple melt sources [e.g. *Shaw et al.*, 2003; *Weinstein et al.*, 2006; *Krienitz et al.*, 2007, 2009, *Ma et al.*, 2011, 2013]. Variability in degrees of partial melting commonly results in con-cave to sub-horizontal curves in MREE/HREE vs LREE/HREE diagrams depending on garnet source enrichment (as HREE are preferentially retained in garnet) [e.g. *Johnson*, 1998]. These patterns are in contrast with the semi-linear trends described by the group 1 and 2 samples (Figure 31). The gap separating group 3 would also imply a significantly large difference in degrees of melt extraction for these samples. On the basis of this, I deem it unlikely for my selection of melts to have been produced through simple batch melting processes. Therefore, this melt inclusion sample set indicates melting of variable sources, perhaps under different conditions.

7.2 Melting of metasomatic lithosphere

In order to explain the geochemical signature of the Harrat al-Shamah, melts have been proposed to have been derived from multiple exotic mantle lithologies, such as amphibolite [*Weinstein et al.*, 2006] and hornblendite [*Ma et al.*, 2011, 2013]. Such hydrous phases would account for the presence of especially low Rb/Ba ratios observed by *Weinstein et al.* (2006). Amphibole retention would then account for High Nb/Ba and Sr/Ba ratios, through preferential incorporation of Ba [*Weinstein et al.*, 2006]. Nevertheless, Rb/Ba ratios in my samples (0.24-2.02, mean=0.81±0.26, PM normalised) are much higher than those found by *Weinstein et al.* (2006) (0.08-1.01, mean=0.49, PM normalised). Instead, my samples are more similar to data from e.g. *Krienitz et al.* (2007), with a mean of 0.68 from Syrian rocks, or *Baker* (1997), whom reported a mean of 0.63 in Yemeni rocks. However, the best match with my data are the Ethiopian high [3]He lavas, with a mean of 0.86 ±0.21 [*Pik et al.*, 1999].

Elevated Sr/Ba ratios are observed, but I instead attribute these to high Sr concentrations, which are common for rocks in this area [*Lustrino & Sharkov*, 2006]. Alternatively, *Ma et al.* (2011; 2013) argued for the requirement of hydrous lithospheric melting of hornblendite on the basis of a reported K/La depletion [*Krienitz et al.*, 2007, 2009] previously associated with a Red Sea-similar magma source [*Krienitz et al.*, 2007, 2009], as well as high alkalis and TiO_2, and low Rb and Zr concentrations. These authors follow the line of reasoning of *Pilet et al.* (2008), whom argued that mixing of melts derived from lithospheric metasomatic veins and mantle peridotite can explain the compositional trends observed in alkaline lavas. Although there is K/La data for my samples, no melt inclusions (including TiO_2-rich, SiO_2-poor sample 04-137) include significant depletions of Rb or Zr. Consequentially, my Sm/Zr data does not follow the hornblendite mixing curves constructed to explain the data of *Ma et al.* (2011) (Figure 35). On the basis of these observations I infer that melting of metasomatic veins is likely to be of no- to little influence on this melt inclusion population.

7.3   Melting conditions

By excluding significant contributions of metasomatic veins to the primary magma compositions, I can assume that melts are most likely derived from spinel and/or garnet bearing mantle peridotite. Melting models for the volcanism in Syria have considered both end-members, and there is an agreement in the literature that some degree of melting of garnet peridotite is required in order to explain the significantly elevated MREE/HREE ratios in these rocks [e.g. *Shaw et al.*, 2003; *Lustrino & Sharkov*, 2006; *Weinstein et al.*, 2006; *Krienitz et al.*, 2007, 2009;
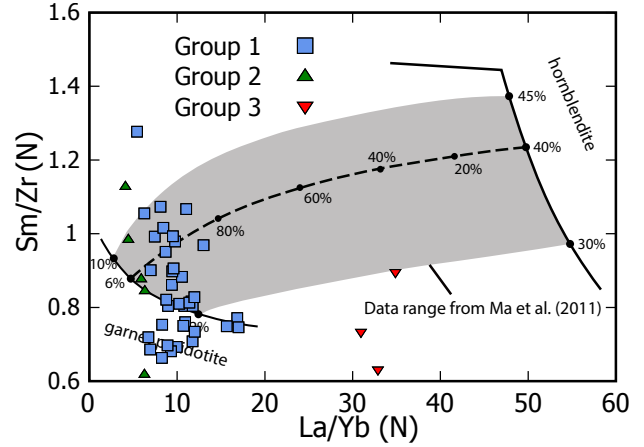
Figure 35: PM normalized Sm/Zr versus La/Yb ratios compared to the melting and mixing curves for garnet peridotite and hornblendite constructed by *Ma et al.* (2011) for Syrian alkali basalts and basanites. Primitive mantle normalization values are from *Mcdonough & Sun* (1995). For additional details, see *Ma et al.* (2011).

Ma et al., 2011, 2013]. Similar signatures were observed in my melt inclusions (Dy/Yb=1.83-4.74) (Figure 31). However, contrary to the observations of [*Krienitz et al.*, 2009], the Syrian MIs form a sub-horizontal trend at odds with the garnet lherzolite melting curve (Figure 36). This melting regime additionally fails to account for the group 3 measurements, and would require up to >12% partial melting to produce some of the more depleted measurements. Such degrees of partial melting are unlikely considering the lack of evidence for significant lithospheric extension and/or input of subduction derived fluids [*Pearce & Peate*, 1995; *Haase*, 1996]. This problem is emphasized when other mantle mineralogies are considered, as *Shaw et al.* (2003) found a required partial melting degree in excess of 25% by using different grt/cpx ratios and melting proportions. It is therefore unlikely that my dataset is the result of variable degrees of partial melting of garnet lherzolite. Alternatively, binary mixing

models such as the ones proposed for Jordanian and Yemeni volcanics by *Shaw et al.* (2003) and *Baker et al.* (2000), respectively, would explain the linear trend produced by the Syrian melt compositions in MREE/HREE vs LREE/HREE space (Figure 31, 37) without requiring unrealistically high degrees of partial melting. Following the approach of *Shaw et al.* (2003), the set of group 1 and 2 samples can be observed to follow a binary mixing line between >2% partial melting of garnet lherzolite and <2% melting of spinel lherzolite. For the bulk of the data, garnet:spinel lherzolite melt ratios of 90:10 to 70:30 are sufficient to explain the geochemical enrichment patterns. On the same mixing line, few group 1 and 2 measurements instead appear to represent almost complete melting of spinel lherzolite (Figure 37), which is in agreement with a stronger compositional resemblance to shallow melting derived Yemeni rocks (Figure 31) [*Baker et al.*, 1997]. Conversely, all group 3
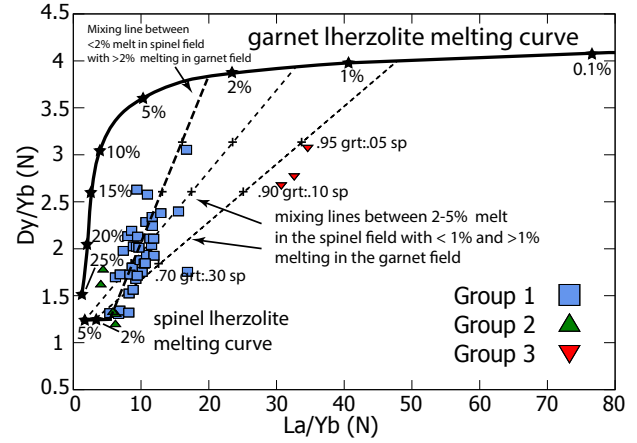
Figure 37: Primitive mantle normalized Dy/Yb vs La/Yb compared to expected partial melting curves for garnet and spinel lherzolite non-modal fractional melting constructed by *Shaw et al.* (2003). Mantle source composition is slightly enriched with La/Yb (N)=0.99 and Dy/Yb (N)=1.22. Binary mixing lines are included to represent variable garnet-spinel ratios (dashed, thin). An additional approximate mixing line is included representing my samples, indicating approximately 2-3 % partial melting of garnet lherzolite and <2% melting of spinel lherzolite (dashed, thick). Primitive mantle normalization values are from *Taylor & Mclennan* (1985). For additional details, see *Shaw et al.* (2003).
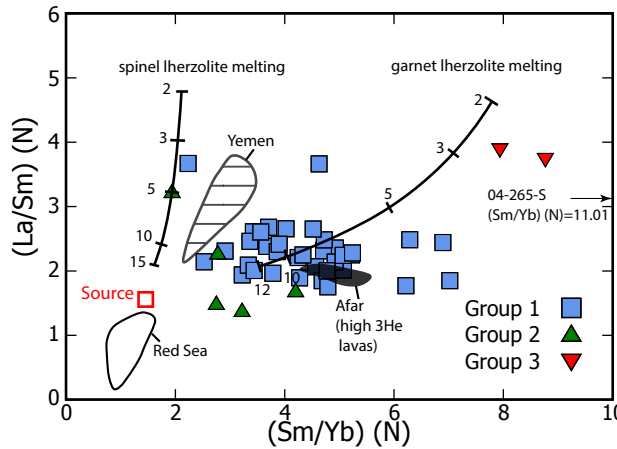
Figure 36: Chondrite normalized La/Sm versus Sm/Yb ratios compared to the melting and curves for garnet and spinel peridotite sources constructed by *Krienitz et al.* (2009). Chondrite normalization values are from *Mcdonough & Sun* (1995). For additional details, see *Krienitz et al.* (2009).

measurements plot on a separate mixing curve characterised by a smaller degree of melting in the garnet lherzolite field (<1%) (Figure 37), consistent with the more enriched geochemical signal of the melt inclusions. These samples require garnet:spinel melt mixing ratios of 95:05 to 90:10, suggesting a deeper origin and contrasting melting regime compared to the rest of the data. A progressive increase in melting depths and a coinciding decrease in melt fractions from group 2 to 3 is also suggested by major elements. Namely, increasing melting depths are associated with a decrease in SiO_2, and due to the moderate incompatibility of TiO_2, K_2O, and Na_2O, these oxides are likely to concentrate in small melt fractions [*Klein & Langmuir*, 1987; *Hirose & Kushiro*, 1993]. I observe a nearly iden-

tical trend in my major element data (Figure 34), excluding an anomalously low Na_2O concentration in the group 3 sample, which may be related to the volume estimations. By combining my thermometric data with information regarding spinel- garnet facies transition depth, melting depths of the respective end-members can be approximated. Observations from seismic tomography and xenoliths have located the lithosphere-asthenosphere boundary at 60-80 km depth [*Nasir & Safarjalani*, 2000; *Hofstetter & Bock*, 2004; *Hansen et al.*, 2007]. Depending on the estimate, this is close to the spinel-garnet transition zone which is estimated at 60-70 km depth based on xenolith studies [*Mcguire*, 1987; *Nasir & Safarjalani*, 2000]. Combining this observation with my maximum temperature esti-

Figure 38: P-T-depth diagram as adapted from *Krienitz et al.* (2007) indicating mantle melting conditions. The shaded temperature area displays the 1360-1400°C interval estimated for maximum primary melt generation. Approximate maximum melting depth of primary magmas is indicated by the star. Dry solidus and asthenospheric mantle adiabats are based on *McKenzie & Bickle* (1988). Spinel-garnet transition depth interval (purple, dashed) is based on *Mcguire* (1987) and *Nasir & Safarjalani* (2000). Lithosphere-asthenosphere boundary (LAB) on seismic and xenolith studies, see text. P-T estimates by *Krienitz et al.* (2007) are displayed as black circles.

mates of 1360 to 1400 °C, the maximum melting depth can be located directly on the dry solidus [*McKenzie & Bickle*, 1988], coinciding with the transition to garnet facies peridotite, at the bottom of the lithosphere (Figure 38). This depth estimate is likely representative of the garnet lherzolite melt fractions generating the high MREE/HREE ratios. As there is no minimum temperature estimate for my samples, the spinel-lherzolite derived end-member melts may have been produced over an extended depth interval up to approximately 60 km. Considering the relatively thick lithosphere under western Arabia, it is not unlikely for this to involve lithospheric melting, which is consistent with previous observations [*Shaw et al.*, 2003; *Lustrino & Sharkov*, 2006; *Ma et al.*, 2011, 2013]. I therefore suggest mantle melting to occur over a depth interval stretching upward from the lithosphere-asthenosphere boundary, without the need for significantly increased ambient mantle temperatures.

7.4 Magma sources

The presence of enriched mantle underneath West-Arabia has been a consistent observation among previous studies, and is an underlying requirement for many petrogenetic models of the area, regardless of plume involvement [*Camp & Roobol*, 1992; *Stein & Hofmann*, 1992; *Shaw et al.* (2003); *Weinstein et al.*, 2006; *Krienitz et al.* (2007); *Ismail et al.*, 2008; *Ma et al.*, 2013]. This hypothesis is consistent with my observations regarding enrichment sensitive trace element ratios, for which groups 1 and 3 display OIB-like and higher degrees of enrichment (Figure 32, 37, 39). A progressive transition from OIB-type (alkaline) to P-MORB compositions is dictated by the group 1 and 2 samples (Figure
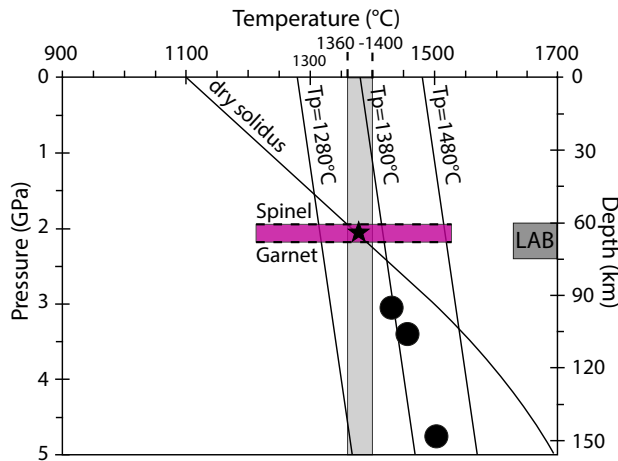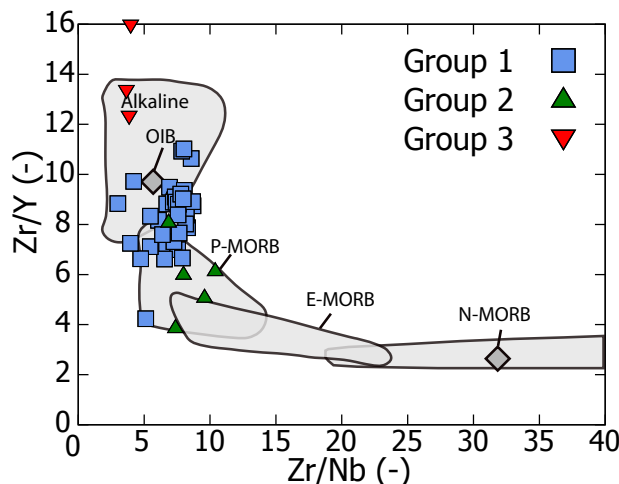
Figure 39: Zr/Y vs Zr/Nb ratios for Syrian melt inclusions as adapted from *Saccani et al.* (2014). Fields representative of alkaline, P-MORB, E-MORB, and N-MORB are based on *Saccani et al.* (2013a), *Chauvet et al.* (2011), and *Lapierre et al.* (2004). Compositions of OIB and N-MORB (circles) are from *Sun & Mcdonough* (1989)

Red Sea MORB sources. However, in order to reconcile this with the earlier discussed binary mixing model, the MORB-type signature must be more concentrated in the uppermost asthenosphere, and may have partially equilibrated with parts of the lower lithosphere. Within this framework, groups 1 and 2 represent mixing between melts derived from 2-3% partial melting of mixed OIB-MORB asthenosphere in the garnet facies and shallower melting of spinel facies peridotite, with a geochemical signature more akin to Red Sea MORB. Group 3 melts are instead composed of higher grt:sp mixing ratios, with the former component having been produced through less extensive melting, thereby causing their significant enrichment in incompatible trace elements. The smaller degree of melting recorded in group 3 melts can be attributed to either higher pressures, or a temporal decrease in local mantle temperatures [*McKenzie & Bickle*, 1988].

7.5   Tectonic relationships

Plume-type signatures in western Arabia are commonly associated with northward channelling of the Afar mantle plume, located between Ethiopia and Yemen [e.g. *Camp & Roobol*, 1992; *Sobolev et al.*, 2005; *Krienitz et al.*, 2007, 2009; *Ma et al.*, 2011, 2013; *Chang & Van der Lee*; *Faccena et al.*, 2013]. Disregarding geochemical arguments, the northward migration of the Afar plume is supported by (1) regional uplift in West-Arabia [*Camp & Roobol*, 1992; *Daradich et al.*, 2003; *Sobolev et al.*, 2005], (2) an inferred elevated geotherm in disequilibrium with the surface [*Stein et al.*, 1993; *Nasir et al.*, 2000; *Krienitz et al.*, 2007], and (3) an observed low velocity zone at ±100 km depth [*Debayle et al.*, 2001; *Chang & Van der Lee*, 2011; *Faccena et al.*, 2013]. These observations are consistent

29, 39), which is characteristic of mixing between OIB- and MORB sources such as observed in Iran [*Saccani et al.*, 2013a, 2013b, 2014]. None of my samples contain E-MORB- or N-MORB-type compositions, indicating a dominance of the OIB-type component relative to E-MORB. Combined tapping of Red Sea-like MORB and plume material was also suggested by *Krienitz et al.* (2009), whom argued for a chemically homogeneous mantle reservoir under Arabia represented by Gulf of Aden and Red Sea basalts [*Altherr et al.*, 1988; *Haase et al.*, 2000], locally refertilized by Afar derived plume material. This is not unlike what was suggested by the chemistry of olivine-included spinel (Figure 19, 20), and is consistent with closer chemical resemblance between group 2 melts and Red Sea basalts (Figure 36). Following this approach, group 2 would represent melting of (nearly) fully mixed OIB and

with recent introduction of hot (plume) material, causing thermal erosion of the lithosphere, which leads to isostatic uplift [*Sobolev et al.*, 2005]. The development of these features coincides with extensive intra-plate volcanism, and it is therefore reasonable to assume a tectono-magmatic relationship. Alternatively, extension along the DSFZ has been proposed as a primary mechanism for generating magmatism, especially around Syria [*Shaw et al.*, 2003; *Lustrino & Sharkov*, 2006]. This is agreement with observations from *Krienitz et al.* (2009), who state that the oldest phases of volcanic activity in south- to western Syria coincide with the first phase of movement along the DSFZ. Nevertheless, Arabian intra-plate magmatism extends far beyond the DSFZ, and the primary movement along this fault zone is sinistral rather than extensional [*Sobolev et al.*, 2005], and thereby fails to explain the distribution and abundance of volcanic fields. In addition to this, while extensional features are present in the area [*Matmon et al.*, 2003], these are commonly of insufficient scale to explain extensive lithospheric thinning of the thick Arabian lithosphere. The melting regime suggested by my data is consistent with thermal erosion at the lithosphere-asthenosphere boundary due to plume influences, and is difficult to reconcile with isolated lithospheric upwelling by activity of the Dead Sea Fault Zone. Nevertheless, I do not observe as significant a thermal anomaly as *Krienitz et al.* (2007), but instead find temperatures roughly halfway ambient mantle and plume conditions [*Green et al.*, 2001; *Herzberg et al.*, 2007]. I can therefore exclude the possibility of a separate mantle plume underneath West-Arabia, which was suggested by *Camp & Roobol* (1992) and *Chang & Van der Lee* (2011). The thermal regime of Syrian melts can be attributed either to a pulsing plume influx as
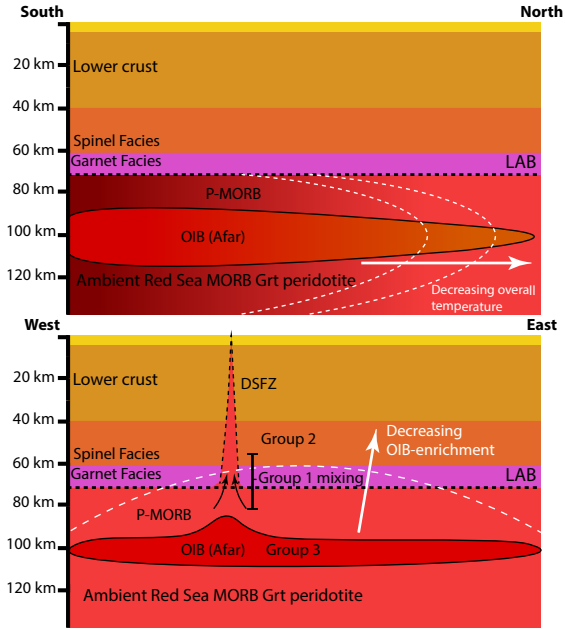

Figure 40: Conceptual cross sections (not to scale) of (top) northward dilution of plume material and asthenospheric temperature decrease, as well as (bottom) melt generation at the DSFZ and progressively increasing OIB enrichment toward deeper levels under the Harrat al-Shamah. Sources for spinel-garnet transition- and LAB depths are as in Figure 38.

suggested by *Krienitz et al.* (2007), or progressive cooling and/or dilution of mantle material as it migrates northward, as was suggested by *Ma et al.* (2011) (Figure 40). I prefer the second hypothesis, as it is difficult to explain cooling rates of ±100°C over a <10 million years, and no temporal data was collected to confirm this. Instead, dilution and cooling of plume material would explain the northward increase in basanites and decreased magma flux observed by *Ma et al.* (2011). This hypothesis additionally explains the contemporaneous development of the DSFZ, as it provides preferential pathways for melts which progressively lose their ability to penetrate the thick Arabian lithosphere (Figure 40).

8 Conclusions and recommendations

Detailed analysis of mineral- and melt inclusions in early crystallizing olivine (Fo=73-85) from the Syrian Harrat al-Shamah indicate a diverse collection of parental magmas. Diverse major element compositions and mineral inclusions are indicative of minor plagioclase and clinopyroxene crystallization prior to melt entrapment. We discern three groups of compositionally distinct melts based on relative trace element enrichments: an enriched, depleted, and intermediate group. The intermediate group is dominant and contains the largest amount of compositions. The enriched group is approximately representative of Syrian basanites, whereas the intermediately enriched melt compositions match alkali-basalt chemistry. Linear LREE/HREE vs MREE/HREE relationships of intermediate- to depleted melts indicate binary mixing between spinel and garnet lherzolite melt end-members, suggesting polybaric melting. Crystallization temperatures inferred from melt inclusion thermometry (up to 1400°C) indicate garnet lherzolite melting to occur near the lithosphere-asthenosphere boundary at approximately 60 km depth. Spinel lherzolite melting is inferred to occur (partly) at lithospheric depths. Both major and trace elements suggest that particularly trace element enriched melts were formed by deeper <1% partial melting of garnet lherzolite mixed with small proportions of spinel lherzolite melts. The significantly high Dy/Yb ratios (up to 4.74) of my samples cannot be explained through melting of primitive mantle, and require an enriched mantle source. Contamination sensitive ratios indicate no influence of subduction and/or crustal assimilation prior to entrapment. Th/Yb vs Nb/Yb and Zr/Y vs Zr/Nb ratios indicate significant contribution of OIB-type and P-MORB-type source components related to mixing of (Afar) plume material and Red Sea MORB. Geochemical trends are inconsistent with melting of metasomatized lithospheric veins. I suggest West-Arabian volcanism to be caused by an interplay between northward migration and progressive dilution of Afar plume material, and the development of preferential zones for mantle upwelling and thermal erosion by activity of the Dead Sea Fault Zone.

In order to verify my conclusions and gain insight into the evolution of the magmatic activity in the area I suggest future studies to focus on dating-coupled melt inclusion analysis. By applying this to the North-South succession of harrats that have been associated with migrating Afar plume material, it may be possible to constrain the progression and driving forces of plume channelling.

9 Acknowledgements

10 References

Al Kwatli, M.A., Gillot, P.Y., Zeyen, H., Hildenbrand, A., Al Gharib, I. *Volcano-tectonic evolution of the northern part of the Arabian plate in the light of new K-Ar ages and remote sensing: Harrat Ash Shaam volcanic province (Syria)* (2012) Tectonophysics, 580, pp. 192-207.

Altherr, R., Henjes-Kunst, F., Puchelt, H., Baumann, A. *Volcanic activity in the Red Sea axial trough - evidence for a large mantle diapir?* (1988) Tectonophysics, 150 (1-2), pp. 121-133.

Altherr, R., Henjes-Kunst, F., Baumann, A. *Asthenosphere versus lithosphere as possible sources for basaltic magmas erupted during formation of the Red Sea: constraints from Sr, Pb and Nd isotopes* (1990) Earth and Planetary Science Letters, 96 (3-4), pp. 269-286.

Baker, J.A., Menzies, M.A., Thirlwall, M.F., Macpherson, C.G. *Petrogenesis of quaternary intraplate volcanism, Sana'a, Yemen: Implications for plume-lithosphere interaction and polybaric melt hybridization* (1997) Journal of Petrology, 38 (10), pp. 1359-1390.

Baker, J.A., MacPherson, C.G., Menzies, M.A., Thirlwall, M.F., Al-Kadasi, M., Mattey, D.P. *Resolving crustal and mantle contributions to continental flood volcanism, Yemen; constraints from mineral oxygen isotope data* (2000) Journal of Petrology, 41 (12), pp. 1805-1820.

Bas, M.J.L., Maitre, R.W.L., Streckeisen, A., Zanettin, B. *A chemical classification of volcanic rocks based on the total alkali-silica diagram* (1986) Journal of Petrology, 27 (3), pp. 745-750.

Bergantz, G.W., Dawes, R. *Aspects of Magma Generation and Ascent in Continental Lithosphere* (1994) International Geophysics, 57 (C), pp. 291-317.

Beccaluva, L., Bianchini, G., Ellam, R.M., Natali, C., Santato, A., Siena, F., Stuart, F.M. *Peridotite xenoliths from Ethiopia: Inferences about mantle processes from plume to rift settings* (2011) Special Paper of the Geological Society of America, 478, pp. 77-104.

Bilal, A., Touret, J.L.R. *Mantle xenoliths in recent volcanism from Syrian rift [Les enclaves du volcanisme récent du rift syrien]* (2001) Bulletin de la Societe Geologique de France, 172 (1), pp. 3-16.

Bonatti, E., Ottonello, G., Hamlyn, P.R. *Peridotites from the island of Zabargad (St John), Red Sea: petrology and geochemistry.* (1986) Journal of Geophysical Research, 91 (B1), pp. 599-631.

Brew, G., Lupa, J., Barazangi, M., Sawaf, T., Al-Imam, A., Zaza, T. *Structure and tectonic development of the Ghab basin and the Dead Sea fault system, Syria* (2001) Journal of the Geological Society, 158 (4), pp. 665-674.

Camp, V.E., Roobol, M.J. *The Arabian continental alkali basalt province: Part I. Evolution of Harrat Rahat, Kingdom of Saudi Arabia* (1989) Geological Society of America Bulletin, 101 (1), pp. 71-95.

Camp, V.E., Roobol, M.J. *Upwelling asthenosphere beneath western Arabia and its regional implications* (1992) Journal of Geophysical Research, 97 (B11), pp. 15,255-15,271.

Chang, S.-J., Van der Lee, S. *Mantle plumes and associated flow beneath Arabia and East Africa* (2011) Earth and Planetary Science Letters, 302 (3-4), pp. 448-454.

Danyushevsky, L.V., Della-Pasqua, F.N., Sokolov, S. *Re-equilibration of melt in-*

clusions trapped by magnesian olivine phenocrysts from subduction-related magmas: Petrological implications (2000) Contributions to Mineralogy and Petrology, 138 (1), pp. 68-83.

Danyushevsky, L.V., Plechov, P. *Petrolog3: Integrated software for modeling crystallization processes* (2011) Geochemistry, Geophysics, Geosystems, 12 (7), art. no. Q07021, .

Daradich, A., Mitrovica, J.X., Pysklywec, R.N., Willett, S.D., Forte, A.M. *Mantle flow, dynamic topography, and rift-flank uplift of Arabia* (2003) Geology, 31 (10), pp. 901-904.

Debayle, E., Lévêque, J.-J., Cara, M. *Seismic evidence for a deeply rooted low-velocity anomaly in the upper mantle beneath the northeastern Afro/Arabian continent* (2001) Earth and Planetary Science Letters, 193 (3-4), pp. 423-436.

Eissen, J.-P., Juteau, T., Joron, J.-L., Dupre, B., Humler, E., Al'mukhamedov, A. *Petrology and geochemistry of basalts from the red sea axial rift at 18° north* (1989) Journal of Petrology, 30 (4), pp. 791-839.

Faccenna, C., Becker, T.W., Jolivet, L., Keskin, M. *Mantle convection in the Middle East: Reconciling Afar upwelling, Arabia indentation and Aegean trench rollback* (2013) Earth and Planetary Science Letters, 375, pp. 254-269.

Fitton, J.G. *The Cameroon line, West Africa: a comparison between oceanic and continental alkaline volcanism.* (1987) Alkaline igneous rocks, pp. 273-291.

Ford, C.E., Russell, D.G., Craven, J.A., Fisk, M.R. *Olivine-liquid equilibria: temperature, pressure and composition dependence of the crystal/liquid cation partition coefficients for Mg, Fe2+, Ca and Mn.*(1983) Journal of Petrology, 24 (3), pp. 256-265.

Furman, T., Bryce, J., Rooney, T., Hanan, B., Yirgu, G., Ayalew, D. *Heads and tails: 30 million years of the Afar plume* (2006) Geological Society Special Publication, 259, pp. 95-119.

Garfunkel, Z. *Internal structure of the Dead Sea leaky transform (rift) in relation to plate kinematics* (1981) Tectonophysics, 80 (1-4), pp. 81-108.

Green, D.H., Falloon, T.J., Eggins, S.M., Yaxley, G.M. *Primary magmas and mantle temperatures* (2001) European Journal of Mineralogy, 13 (3), pp. 437-451.

Haase, K.M. *The relationship between the age of the lithosphere and the composition of oceanic magmas: Constraints on partial melting, mantle sources and the thermal structure of the plates* (1996) Earth and Planetary Science Letters, 144 (1-2), pp. 75-92.

Haase, K.M., Mühe, R., Stoffers, *P. Magmatism during extension of the lithosphere: Geochemical constraints from lavas of the Shaban Deep, northern Red Sea* (2000) Chemical Geology, 166 (3-4), pp. 225-239.

Hansen, S.E., Rodgers, A.J., Schwartz, S.Y., Al-Amri, A.M.S. *Imaging ruptured lithosphere beneath the Red Sea and Arabian Peninsula* (2007) Earth and Planetary Science Letters, 259 (3-4), pp. 256-265.

Hegner, E., Pallister, J.S. *Pb, Sr, and Nd isotopic characteristics of Tertiary Red Sea rift volcanics from the central Saudi Arabian Coastal Plain* (1989) Journal of Geophysical Research, 94 (B6), pp. 7749-7755.

Hempton, M.R. *Constraints on Arabian Plate motion and extensional history of the Red Sea* (1987) Tectonics, 6 (6), pp. 687-705.

Herzberg, C., Asimow, P.D., Arndt, N., Niu, Y., Lesher, C.M., Fitton, J.G., Cheadle,

M.J., Saunders, A.D. *Temperatures in ambient mantle and plumes: Constraints from basalts, picrites, and komatiites* (2007) Geochemistry, Geophysics, Geosystems, 8 (2), art. no. Q02006, .

Hirose, K., Kushiro, I. *Partial melting of dry peridotites at high pressures: Determination of compositions of melts segregated from peridotite using aggregates of diamond* (1993) Earth and Planetary Science Letters, 114 (4), pp. 477-489.

Hofstetter, A., Bock, G. *Shear-wave velocity structure of the Sinai subplate from receiver function analysis* (2004) Geophysical Journal International, 158 (1), pp. 67-84.

Hofmann, A.W., Jochum, K.P., Seufert, M., White, W.M. *Nb and Pb in oceanic basalts: new constraints on mantle evolution* (1986) Earth and Planetary Science Letters, 79 (1-2), pp. 33-45.

Ismail, M., Delpech, G., Cottin, J.-Y., Grégoire, M., Moine, B.N., Bilal, A. *Petrological and geochemical constraints on the composition of the lithospheric mantle beneath the Syrian rift, northern part of the Arabian plate* (2008) Geological Society Special Publication, 293, pp. 223-251.

Jarrar, G., Stern, R.J., Saffarini, G., Al'Zubi, H. *Late- and post-orogenic Neoproterozoic intrusions of Jordan: Implications for crustal growth in the northernmost segment of the East African Orogen* (2003) Precambrian Research, 123 (2-4), pp. 295-319.

Johnson, K.T.M. *Experimental determination of partition coefficients for rare earth and high-field-strength elements between clinopyroxene, garnet, and basaltic melt at high pressures* (1998) Contributions to Mineralogy and Petrology, 133 (1-2), pp. 60-68

Kamenetsky, V.S., Crawford, A.J., Meffre, S. *Factors controlling chemistry of magmatic spinel: An empirical study of associated olivine, Cr-spinel and melt inclusions from primitive rocks* (2001) Journal of Petrology, 42 (4), pp. 655-671.

Klein, E.M., Langmuir, C.H. *Global correlations of ocean ridge basalt chemistry with axial depth and crustal thickness.* (1987) Journal of Geophysical Research, 92 (B8), pp. 8089-8115.

Krienitz, M.-S., Haase, K.M., Mezger, K., Shaikh-Mashail, M.A. *Magma genesis and mantle dynamics at the Harrat Ash Shamah volcanic field (southern Syria)* (2007) Journal of Petrology, 48 (8), pp. 1513-1542.

Krienitz, M.-S., Haase, K.M., Mezger, K., Van Den Bogaard, P., Thiemann, V., Shaikh-Mashail, M.A. *Tectonic events, continental intraplate volcanism, and mantle plume activity in northern Arabia: Constraints from geochemistry and Ar-Ar dating of Syrian lavas* (2009) Geochemistry, Geophysics, Geosystems, 10 (4), art. no. Q04008,.

Laws, E.D., Wilson, M. *Tectonics and magmatism associated with Mesozoic passive continental margin development in the Middle East* (1997) Journal of the Geological Society, 154 (3), pp. 459-464.

Lustrino, M., Sharkov, E. *Neogene volcanic activity of western Syria and its relationship with Arabian plate kinematics* (2006) Journal of Geodynamics, 42 (4-5), pp. 115-139.

Ma, G.S.-K., Malpas, J., Xenophontos, C., Chan, G.H.-N. *Petrogenesis of latest miocene-quaternary continental intraplate volcanism along the northern Dead Sea Fault System (Al Ghab-Homs volcanic field), western Syria: Evidence for lithosphere-asthenosphere interaction* (2011) Journal of Petrology, 52 (2), art. no. egq085, pp. 401-

430.

Ma, G.S.-K., Malpas, J., Suzuki, K., Lo, C.-H., Wang, K.-L., Iizuka, Y., Xenophontos, C. *Evolution and origin of the Miocene intraplate basalts on the Aleppo Plateau, NW Syria* (2013) Chemical Geology, 335, pp. 149-171.

Mason, P.R.D., Nikogosian, I., Van Bergen, M.J. *Major and trace element analysis of melt inclusions by laser ablation ICP-MS.* In: Sylvester P (ed) (2008) Mineralogical Association of Canada short course volume, 40, 219-239.

Matmon, A., Wdowinski, S., Hall, J.K. *Morphological and structural relations in the Galilee extensional domain, northern Israel* (2003) Tectonophysics, 371 (1-4), pp. 223-241.

Maurel, C., Maurel, P. *Etude expérimentale de l'équilibre Fe2+–Fe3+ dans les spinelles chromifères et les liquids silicates basiques coexistants a l atm.* (1982) C.R. Acad. Sci. Paris 295 (II), pp. 209–212.

Mcguire, A.V. *Petrology of mantle xenoliths from harrat al kishb: The mantle beneath Western Saudi Arabia* (1988) Journal of Petrology, 29 (1), pp. 73-92.

McClusky, S., Reilinger, R., Mahmoud, S., Ben Sari, D., Tealeb, A. *GPS constraints on Africa (Nubia) and Arabia plate motions* (2003) Geophysical Journal International, 155 (1), pp. 126-138.

McDonough, W.F., Sun, S.-s. *The composition of the Earth* (1995) Chemical Geology, 120 (3-4), pp. 223-253.

Mckenzie, D., Bickle, M.J. *The volume and composition of melt generated by extension of the lithosphere* (1988) Journal of Petrology, 29 (3), pp. 625-679.

Miyashiro, A. *Nature of alkalic volcanic rock series* (1978) Contributions to Mineralogy and Petrology, 66 (1), pp. 91-104.

Nasir, S., Safarjalani, A. *Lithospheric petrology beneath the northern part of the Arabian Plate in Syria: Evidence from xenoliths in alkali basalts* (2000) Journal of African Earth Sciences, 30 (1), pp. 149-168.

Natali, C., Beccaluva, L., Bianchini, G., Ellam, R.M., Savo, A., Siena, F., Stuart, F.M. *High-MgO lavas associated to CFB as indicators of plume-related thermochemical effects: The case of ultra-titaniferous picrite-basalt from the Northern Ethiopian-Yemeni Plateau* (2016) Gondwana Research, 34, pp. 29-48.

Pearce, J.A., Peate, D.W. *Tectonic implications of the composition of volcanic arc magmas* (1995) Annual Review of Earth & Planetary Sciences, 23, pp. 251-285.

Pik, R., Deniel, C., Coulon, C., Yirgu, G., Hofmann, C., Ayalew, D. *The northwestern Ethiopian Plateau flood basalts: classification and spatial distribution of magma types* (1998) Journal of Volcanology and Geothermal Research, 81 (1-2), pp. 91-111.

Pik, R., Deniel, C., Coulon, C., Yirgu, G., Marty, B. *Isotopic and trace element signatures of Ethiopian flood basalts: Evidence for plume-lithosphere interactions* (1999) Geochimica et Cosmochimica Acta, 63 (15), pp. 2263-2279.

Pilet, S., Baker, M.B., Stolper, E.M. *Metasomatized lithosphere and the origin of alkaline lavas* (2008) Science, 320 (5878), pp. 916-919.

Rogers, N.W. *The isotope and trace element geochemistry of basalts from the volcanic islands of the southern Red Sea* (1993) Geological Society Special Publication, 76, pp. 455-467.

Rudnick, R.L., Fountain, D.M. *Nature and com-*

position of the continental crust: A lower crustal perspective (1995) Reviews of Geophysics, 33 (3), pp. 267-309.

Saccani, E., Allahyari, K., Beccaluva, L., Bianchini, G. *Geochemistry and petrology of the Kermanshah ophiolites (Iran): Implication for the interaction between passive rifting, oceanic accretion, and OIB-type components in the Southern Neo-Tethys Ocean* (2013a) Gondwana Research, 24 (1), pp. 392-411.

Saccani, E., Azimzadeh, Z., Dilek, Y., Jahangiri, A. *Geochronology and petrology of the Early Carboniferous Misho Mafic Complex (NW Iran), and implications for the melt evolution of Paleo-Tethyan rifting in Western Cimmeria* (2013b) Lithos, 162-163, pp. 264-278.

Saccani, E., Allahyari, K., Rahimzadeh, B. *Petrology and geochemistry of mafic magmatic rocks from the Sarve-Abad ophiolites (Kurdistan region, Iran): Evidence for interaction between MORB-type asthenosphere and OIB-type components in the southern Neo-Tethys Ocean* (2014) Tectonophysics, 621, pp. 132-147.

Schilling, J.-G., Kingsley, R.H., Hanan, B.B., McCully, B.L. *Nd-Sr-Pb isotopic variations along the Gulf of Aden: evidence for Afar mantle plume-continental lithosphere interaction* (1992) Journal of Geophysical Research, 97 (B7), pp. 10,927-10,966.

Schindelin, J., Arganda-Carreras, I., Frise, E., Kaynig, V., Longair, M., Pietzsch, T., Preibisch, S., Rueden, C., Saalfeld, S., Schmid, B., Tinevez, J.-Y., White, D.J., Hartenstein, V., Eliceiri, K., Tomancak, P., Cardona, A. *Fiji: An open-source platform for biological-image analysis* (2012) Nature Methods, 9 (7), pp. 676-682.

Schindelin, J., Rueden, C.T., Hiner, M.C., Eliceiri, K.W. *The ImageJ ecosystem: An open platform for biomedical image analysis* (2015) Molecular Reproduction and Development, 82 (7-8), pp. 518-529.

Shaw, J.E., Baker, J.A., Menzies, M.A., Thirlwall, M.F., Ibrahim, K.M. *Petrogenesis of the largest intraplate volcanic field on the Arabian plate (Jordan): A mixed lithosphere - Asthenosphere source activated by lithospheric extension* (2003) Journal of Petrology, 44 (9), pp. 1657-1679.

Sharkov, E.V., Chernyshev, I.V., Devyatkin, E.V., Dodonov, A.E., Ivanenko, V.V., Karpenko, M.I., Leonov, Yu.G., Hanna, S., Khatib, K. *Geochronology of Late Cenozoic Basalts in Western Syria* (1994) Petrology 2, pp. 385-394

Sharkov, E.V., Snyder, G.A., Taylor, L.A., Laz'ko, E.E., Jerde, E., Hanna, S. *Geochemical peculiarities of the asthenosphere beneath the Arabian plate: Evidence from mantle xenoliths of the quaternary Tell-Danun volcano (Syrian-Jordan Plateau, Southern Syria)* (1996) Geochemistry International, 34 (9), pp. 737-752.

Sobolev, A.V. *Melt inclusions in minerals as a source of principle petrological information* (1996) Petrology, 4 (3), pp. 209-220.

Sobolev, S.V., Petrunin, A., Garfunkel, Z., Babeyko, A.Y. *Thermo-mechanical model of the Dead Sea Transform* (2005) Earth and Planetary Science Letters, 238 (1-2), pp. 78-95.

Stein, M., Hofmann, A.W. *Fossil plume head beneath the Arabian lithosphere?* (1992) Earth and Planetary Science Letters, 114 (1), pp. 193-209.

Stein, M., Garfunkel, Z., Jagoutz, E. *Chronothermometry of peridotitic and pyroxenitic xenoliths: Implications for the*

thermal evolution of the Arabian lithosphere (1993) Geochimica et Cosmochimica Acta, 57 (6), pp. 1325-1337.

Sun, S.-S., McDonough, W.F. *Chemical and isotopic systematics of oceanic basalts: Implications for mantle composition and processes* (1989) Geological Society Special Publication, 42 (1), pp. 313-345

Taylor, S.R., McLennan, S.M. *The Continental Crust: its Composition and Evolution.* (1985). Oxford: Blackwell Science.

Trifonov, V.G., Dodonov, A.E., Sharkov, E.V., Golovin, D.I., Chernyshev, I.V., Lebedev, V.A., Ivanova, T.P., Bachmanov, D.M., Rukieh, M., Ammar, O., Minini, H., Al Kafri, A.-M., Ali, O. *New data on the Late Cenozoic basaltic volcanism in Syria, applied to its origin* (2011) Journal of Volcanology and Geothermal Research, 199 (3-4), pp. 177-192.

Weinstein, Y., Navon, O., Altherr, R., Stein, M. *The role of lithospheric mantle heterogeneity in the generation of Plio-Pleistocene alkali basaltic suites from NW Harrat Ash Shaam (Israel)* (2006) Journal of Petrology, 47 (5), pp. 1017-1050.

Weinstein, Y., Garfunkel, Z. *The dead sea transform and the volcanism in Northwestern Arabia* (2014) Modern Approaches in Solid Earth Sciences, 6, pp. 91-108.